Integration of a 15-Element, VHF Bow-Tie Antenna Array into an Aerodynamic Fairing on a NASA P-3 Aircraft

by

Kyle J. Byers
University of Kansas, 2011

Submitted to the graduate degree program in Electrical Engineering & Computer Science and the Graduate Faculty of the University of Kansas School of Engineering in partial fulfillment of the requirements for the degree of **Master of Science**

_____
Dr. Sarah A. Seguin (Chairperson)

_____
Dr. Carl Leuschen

_____
Dr. Chris Allen

Date Defended: June 8, 2011

The Thesis Committee for Kyle J. Byers
certifies that this is the approved version of the following thesis:

Integration of a 15-Element, VHF Bow-Tie Antenna Array into an Aerodynamic Fairing on a NASA P-3 Aircraft

Committee:

_____

Dr. Sarah A. Seguin (Chairperson)

_____

Dr. Carl Leuschen

_____

Dr. Chris Allen

Date Approved: June 8, 2011

Abstract

Radar depth sounding and imaging of deep glaciers in Antarctica and Greenland yield results for better understanding a changing climate and improving glacier modeling. A 15-element, airborne antenna array with an increased bandwidth was developed to advance the potential for radar measurements as part of NASA Operation IceBridge (OIB). These antennas were a planar, modified bow-tie antenna design. The antennas were fed using a custom ferrite, transmission line transformer balun capable of operating with high power signals and across a wide frequency range. An aerodynamic fairing enclosed the antennas and was required to achieve structural performance, but the structural design contradicted and imposed limitations on the antenna performance. Dielectric and parasitic conductors loaded the antenna, limited bandwidth and decreased return loss. Detailed analysis through full-wave simulations and measurements identified the structural effects on the antenna. Proper compensation techniques regarding antenna design and adaption of the surrounding structure improved the antenna performance. The original structure design rendered the antenna incapable of producing a return loss greater than 10 dB, and the final structure and antenna design achieved a bandwidth of 41% with a center frequency of 195 MHz in reference to a 10 dB return loss. The design also considered the mutual coupling between array elements, and this was reduced using unique modifications to the antenna ends.

Acknowledgments

I would like to thank my advisor Dr. Sarah Seguin for her confidence in my capabilities throughout my studies and research. She has encouraged me to develop my research to stronger levels. Also, I would like to thank her and my committee for their interest in this project and my personal development as an engineer and researcher.

The advice and support of Dr. Harish was most helpful throughout this project. He not only designed the original antenna, but he provided antenna expertise enabling better integration with the structure and limiting the mutual coupling. The opportunity to work with him was a blessing to this project and my education.

I would like to thank Dr. Prasad Gogineni for the support and advice throughout the project and my graduate research with the Center for Remote Sensing of Ice Sheets (CReSIS). Of course he had a strong interest in the success of this project, but also he showed an interest in my education and development as a researcher. This was fostered as he took the time to explain concepts pertinent to my contribution to the radar systems and to the larger goals of CReSIS.

I would like to thank the CReSIS team, which consists of many individuals that contributed to this project and my education. I am listing a few individuals, but many other graduate students and staff members have contributed and made working at CReSIS a memorable and enriching experience. Emily Arnold, an aerospace engineering graduate student, shared a mutual interdisciplinary collaboration throughout this project. Fernando Rodriguez-Morales showed commitment to my success as a researcher, student and engineer. He took time from his busy schedule to explain or discuss my progress. Ben Panzer introduced me to HFSS. Victor Jara encouraged me to include the effects of the baluns for agreement between simulations and measurements. John Hunter allowed me the opportunity to help in composite lab and learn about the manufacturing process. Finally, I would like to thank my friends and family for their support outside work. In particular, the journey through graduate school and life outside has definitely offered obstacles to overcome, and my girlfriend, Amanda Zimmerschied, has supported me every step.

Contents

List of Figures

List of Tables

Chapter 1

Introduction

An antenna array was developed for an ice-penetrating and imaging radar that generates images of the ice-bedrock interface, which may be a few kilometers below the surface of the ice. The array consisted of 15 modified bow-tie antennas operating at 195 MHz with a bandwidth optimized to achieve 41%. This antenna array was mounted to a P-3 aircraft in three cusom aerospace fairings as part of NASA Operation IceBridge (OIB). An in-flight picture of the aircraft and farings is shown in Figure 1.1.

Figure 1.1: Custom Aerospace Fairings Enclosing Radar Antennas on a NASA P-3 Aircraft

1.1 Motivation

The National Science Foundation (NSF) funded Center for Remote Sensing of Ice Sheets (CReSIS) develops radar to advance the knowledge about the glacier in Greenland and Antarctica. This data is crucial for modeling the glacier dynamics, and these models help measure and predict sea level change that has a global impact [1]. The sensors developed as part of CReSIS core mission are globally recognized and participate in the OIB. The objectives for OIB are listed below directly from [50]:

> IceBridge is a program of airborne remote sensing measurements designed to fill the gap in measurements between the end of the ICESat-1 mission and the launch of ICESat-2. IceBridge will make two major contributions to cryospheric science:
>
> 1. Provide surface elevation data now that the ICESat-1 mission has ended, focused on areas undergoing rapid change that are critical to characterizing select areas of sea ice and modeling the processes that determine the mass balance of the terrestrial ice sheets. Due to the time variable, non-linear changes that these areas undergo, repeated monitoring is required. IceBridge also allows more detailed studies over these areas, though over much smaller overall areas.
>
> 2. Support complementary measurements critical to ice models such as bed topography, grounding line position, and ice and snow thickness. These parameters cannot be measured by satellite, but can be measured from aircraft. They are the other great unknowns in understanding the ice in general and developing predictive models of sea level rise in response to climate change. (NASA OIB)

The CReSIS radars measure near-surface internal layers, snow over sea ice, surface elevation, ice thickness, internal layers and produce 3D-bed topography maps [1]. One radar records the data for the ice thickness, internal layers and 3D bed topography, which provides valuable basal conditions for improving glacier models [51]. The ice thickness provides information for the mass flux and stress estimates, and the bottom topography provides information for the stress estimates [22]. The range accuracy tells the measurement uncertainty of the absolute distance from the source to an object [39], and the required range accuracy to measure the ice thickness and bottom topography is 5 meters [22]. Increasing the bandwidth improves the range accuracy and reduces the range error given by Equation 1.1 for free-space, where B is the bandwidth, c is the

speed of light and the signal-to-noise ratio is SNR [39].

$$\delta R \simeq \frac{c}{2B\sqrt{2 \times SNR}} \tag{1.1}$$

The SNR depends on several factors such as the transmitted signal power, the channel, the receiver, and the processing techniques. Another radar metric is the range resolution, which tells the distance between two targets needed to distinguish between two targets [39]. The range resolution is also a function of the bandwidth but not the noise and is given in Equation 1.2 for free-space [39].

$$\Delta R = \frac{c\tau}{2} \simeq \frac{c}{2B} \tag{1.2}$$

In Equation 1.2, τ is the pulse duration, which is approximately equal to 1/B. Therefore, increasing the bandwidth will decrease the distance needed to recognize two targets are present and decrease the uncertainty of the absolute distance to an object. Increasing the bandwidth is desirable for improving the data collected with a radar. Note that Equation 1.2 has an approximation that is not valid for a pulse compression radar such as the one used in this application, but increasing the bandwidth will still increase the range resolution. In the case of an ice penetrating radar, the targets exist in the forms of different layers and topographical features on the ice-bed interface. Both Equation 1.1 and Equation 1.2 must be modified for propagation through the medium, which in this case is ice. The propagation is no longer the velocity of light in free-space but is equal to c/n, where n is the refractive index of the ice ($n = \sqrt{\epsilon_r \mu_r}$). Therefore, extending the radar bandwidth will improve the quality of the data regarding the ice-bed interface and the images of the internal layers.

While increasing the bandwidth improves the range accuracy and resolution, the number of antenna elements within the array adds benefits to the data as well. As the number of elements in the antenna array increases, the main beam becomes narrower [72]. The smaller the spatial angle of the main beam the better the angular resolution of the data. This is also true for scanning arrays when the beam is directed at an angle [8]. Similarly, the MUltiple SIgnal Classification (MUSIC) algorithm is used to estimate the angle of arrival of incoming signals, which is limited to the number of antenna elements in the array [64]. This signal processing technique has been used to generate 3-D topographical maps of the ice-bed interface [51, 52]. Therefore, increasing the number of elements will improve the spatial resolution in the cross-track direction as well. Furthermore, increasing the number of antenna elements in the array improves the capabilities of Synthetic Aperture Radar (SAR) processing techniques. Each antenna has an associated phase center, which is the location where spherical waves originate,

and increasing the number of phase centers provides better data on the basal conditions [8, 51]. As a result of the improvement in the signal processing techniques, the surface clutter may better be reduced. Increasing the number of elements improves the beam steering capabilities, which permits the return due to clutter to be better rejected. In this particular applications, clutter is one of the largest detriments for receiving weak bed returns and may appear in the radar data due to surface melt water and other features on and inside the glaciers off the side of the main beam of the array.

The motivation for increasing the bandwidth and the array length has been developed, but the array developed for this thesis is not the first flown for an ice penetrating radar. A previous array flown on the same NASA P-3 aircraft consisted of four dual-band dipoles on each wing shown [61]. The dipoles were centered at 450 MHz and 150 MHz with 30 MHz and 20 MHz bandwidths, respectively [61, 30]. This corresponds to a 6.7% bandwidth at 450 MHz and a 13.3% bandwidth at 150 MHz for a total bandwidth of 20%. Also, this parallel array was configured with a $\lambda/2$ spacing at 150 MHz (1 meter) with peak mutual coupling of 10.3 dB at 140 MHz [61, 30]. It is desirable to minimize the mutual coupling as this indicates energy coupled from one antenna to another in the array [8]. The relative spacing at 450 MHz was 1.5λ with peak mutual coupling of 20.8 dB at 425.3 MHz, which is expected since the relative distance is greater [30]. This array was succesfully deployed with a radar system in Greenland (2007).

Another airborne system was designed to fly at sub-sonic speeds on a NASA DC-8 aircraft, and a custom aerodynamic fairing was constructed for this mission as shown in Figure 1.2 [62]. This array consists of 5 staggered antennas with a row of three dipole antennas and a row of two dipole antennas. These antennas were centered at 195 MHz, and the aerodynamic design restricted the antennas so that they were in close proximity to the ground plane limiting the bandwidth to 10 MHz [62]. This array was successfully deployed in Antarctica (2009 and 2010) and in Greenland (2010).

(a) Inside Fairing (b) Outside Fairing

Figure 1.2: Custom DC-8 Fairing

Another antenna array was deployed on a Twin Otter aircraft consisting of six folded dipoles on each wing. The operation range of these dipoles is 140–160 MHz, and they are arranged in a parallel configuration with 95 cm of spacing as shown in Figure 1.3 [62].

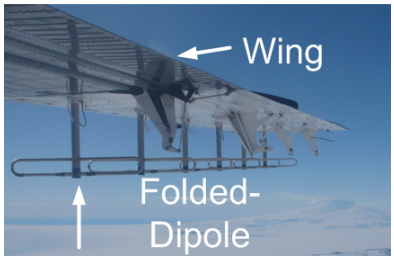

Figure 1.3: Twin Otter Folded-Dipole Array

In comparison with the previous airborne antenna arrays, the array designed for the NASA P-3 aircraft described in this thesis includes more antenna elements and a wider bandwidth than previous systems. These advances improve the radar resolution in terms of both the range and the cross-angular direction. More elements enables advanced signal processing techniques to minimize clutter and improve the images of the ice-bedrock interface.

1.2 Scope of Project

The aerospace fairings enclosed 15 VHF dipole antennas. The symmetry of the structure surrounding the array causes half the antennas to have unique metallic features that impact the performance, while the other half are mirrored versions of the same metallic features. Simulations were completed with Ansoft HFSS version 12 to analyze the antenna performance within the aerospace structure, and were validated with measurements. Furthermore, a high power balun that operates over the given bandwidth was designed to feed these antenna elements. Each of these baluns affect the antenna's input impedance and thus bandwidth. The array was deployed twice, and each array had its own revision. The first revision of the array was designed and manufactured under an aggressive timeline, while the second revision improved upon the performance from the first revision. The analysis consists of the effects from metallic objects in close proximity to antennas and dielectric loading through antenna modifications and structural adaptations.

1.3 Chapter Summaries

Chapter 2: Background Theory

This chapter introduces some basic theory and terminology pertinent to the research explained throughout the remaining chapters. Basic concepts that exemplify the more complex electromagnetic problems are explored here, and these concepts are applied throughout the following chapters. Some of the concepts introduced here are basic antenna theory with an emphasis on bow-ties, baluns, antenna arrays, mutual coupling and parasitic elements.

Chapter 3: Array Design Revision 1

Chapter 3 discusses the design of the balun, the antenna integration challenges and the results from the first revision. These results and challenges provided motivation for a more extensive study. Several areas for improvement are presented in this chapter including the antenna integration with the structure, balun, mitigation of the parasitics in the fairing and mutual coupling.

Chapter 4: Array Design Revision 2

This chapter discusses the changes implemented for the second revision of the array. Several aspects are addressed including the antenna integration with the structure, balun, mitigation of the parasitics in the fairing and mutual coupling. Significant improvement in terms of the operational bandwidth, especially centered around 195 MHz, was achieved and is presented here.

Chapter 5: Conclusions

This section summarizes the results that were achieved after the second revision. The novel contributions are also discussed within this section. While significant improvements were achieved from revision one to revision two, further modifications may help improve the return loss around 195 MHz and improve a few antennas. In addition to the summary, some suggested future work is discussed in this section.

Chapter 2

Background

This chapter introduces some basic theory and terminology pertinent to the research explained throughout the remaining chapters. Basic concepts that exemplify the more complex electromagnetic problems are explored here, and these concepts are applied throughout the following chapters. Some of the concepts introduced here are basic antenna theory with an emphasis on bow-ties, baluns, antenna arrays, mutual coupling and parasitic elements.

2.1 Brief Introduction to Antenna Theory

Antennas are crucial for remote sensing and communication systems, so a brief introduction to antennas, particularly dipoles, is presented with the terminology used throughout the remainder of the document. IEEE defines an antenna as "That part of a transmitting or receiving system that is designed to radiate or to receive electromagnetic waves" [7]. Therefore, a transmit antenna converts signals on transmission lines into radiated energy that travels through the surrounding space. Similarly, a receive antenna focuses energy from the surrounding space onto the transmission line. An important aspect is the connection with the transmission line, because the impedance match at this transition limits the operational bandwidth of the antenna. Occasionally, the input match or the current and voltage relationship is referred to in terms of admittance, which is the inverse of impedance. The antenna input impedance consists of real and imaginary components as shown in Equation 2.1 [72]:

$$Z_{\text{in}} = R_{\text{in}} + jX_{\text{in}} = R_{\text{r}} + R_{\text{o}} + jX_{\text{in}} = \frac{V}{I} \tag{2.1}$$

The real component represents the power dissipated by the antenna, which can either be radiated (R_{r}) or from ohmic losses (R_{o}) . In general, the ohmic losses are small while

most of the energy is radiated. The imaginary part represents the energy stored in the reactive near-field of the antenna and is related to the Q-factor of the antenna, which is the ratio of reactive power to radiated power [72]. As Q increases, the amount of energy stored in the near-field increases and the radiated power decreases and the input impedance is more sensitive to changes in frequency. This limits bandwidth, which is often expressed in terms of a percentage based on the center frequency as shown in Equation 2.2:

$$BW = \frac{f_U - f_L}{f_C} \times 100\% \tag{2.2}$$

Where the f_U is the upper frequency of operation, the f_L is the lower frequency of operation and the f_C is the center frequency. This percentage bandwidth relates the relative operating bandwidth of antenna centered at one frequency to an antenna operating at other frequencies. Another method to describe bandwidth is a ratio, which is commonly used for broadband antennas that have 2:1 or greater bandwidths [72]. The ratio X:1 states that the highest operating frequency is X times the lowest frequency. Bandwidth is important for many applications, and in the case of radar, bandwidth is related to the range accuracy [69]. For a Gaussian pulse, the range accuracy is defined by Equation 2.3, where B = the half-power bandwidth, E = the signal energy and N_0 = the noise power per unit bandwidth [69].

$$\delta T_R = \frac{1.18}{\pi B \sqrt{(2E/N_0)}} \tag{2.3}$$

A common antenna is a dipole, which is considered a resonant antenna. Resonance is commonly defined as the frequency where the input impedance is purely resistive [2]. The length of the antenna determines the frequencies where the antenna will be resonant. The antenna current distribution is used to calculate the far-field pattern and impacts the input impedance of the antenna. The dipole current is sinusoidal with opposing phases, and the currents go to zero at the ends. A half-wavelength long dipole will have a maximum at the center of the antenna, which provides resonant conditions without a minimum in the current distribution (longer than a half-wavelength) nor a current distribution with a triangular shape (shorter than a half-wavelength).

Since the summation of current elements is fundamental for describing radiation, the current distribution can completely describe the radiation pattern of an antenna as shown in Equation 2.4 [72]:

$$f = \int_{-L/2}^{L/2} I(z') e^{jkz' cos(\theta)} dz' \tag{2.4}$$

Where f represents the unnormalized radiation pattern, I(z') is the current distribution along the antenna, and k is the phase constant. For a dipole, the current distribution along a dipole is given by Equation 2.5 [72]:

$$I(z) = I_m \sin[\beta(\frac{L}{2} - |z|)] \quad for\ |z| < \frac{L}{2} \tag{2.5}$$

Where I_m is the maximum current along the antenna; L is the length of the antenna, and z is the position along the antenna. As the length of the dipole changes, the current distribution also changes, which produces different radiation patterns.

A dipole has bandwidths in the range from 8% to 16% with the frequency bounds defined by a Voltage Standing Wave Ratio (VSWR) of 2.0 [72]. The VSWR can be calculated as shown in Equation 2.6 and relates to the magnitude of the reflection coefficient as shown in Equation 2.7 [15]

$$VSWR = \frac{|V_{max}|}{|V_{min}|} = \frac{1 + |\Gamma_L|}{1 - |\Gamma_L|} \tag{2.6}$$

$$|\Gamma_L| = \frac{VSWR - 1}{VSWR + 1} = \frac{Z_L - Z_0}{Z_L + Z_0} \tag{2.7}$$

Where the Γ_L is the reflection coefficient, Z_L is the load impedance and Z_O is the characteristic impedance of the transmission line. In the case of antennas, the antenna is the load and the transmission line is the line impedance. The reflection coefficient can then be used to calculate the return loss as shown in Equation 2.8 [47]. Often bandwidth is discussed in terms of the return loss, and the antenna operational bandwidth is commonly considered across frequencies having a return loss greater than 10 dB.

$$Return\ Loss = -20 \log_{10} |\Gamma_L| \tag{2.8}$$

Another important characteristic of antennas is the gain. Gain describes the amount of power radiated in a particular direction and takes into account the efficiency (e_r) of the antenna, which is the power radiated over the input power. The radiation intensity ($U(\theta, \phi)$) must be defined before the gain, and it is one half the real part of the cross product between the electric field and the complex conjugate of the magnetic field, as shown in Equation 2.10 [72]:

$$U(\theta, \phi) = \frac{1}{2} Re(\mathbf{E} \times \mathbf{H}^*) \cdot r^2 \hat{\mathbf{r}} \tag{2.9}$$

The gain is defined as $4\pi e_r$ times the radiation intensity to the net power over the

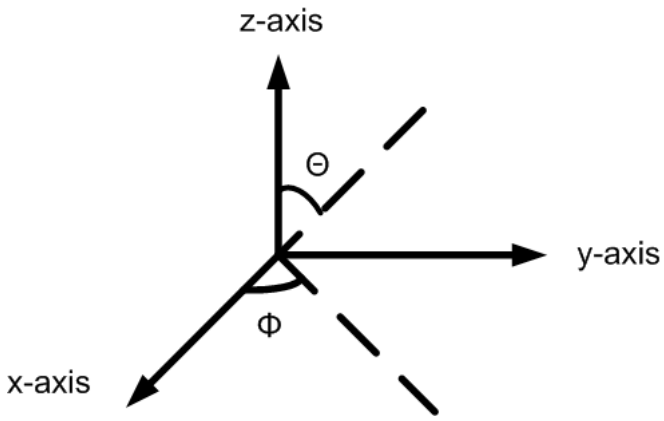

Figure 2.1: Cartesian Coordinate Relationship with Spherical Coordinates

input power [72]. This variable is useful for telling how much power is radiated in a particular direction, taking into effect the imperfections of antennas, such as Ohmic losses. Often the gain is expressed in decibels using the following equation [72] and applied in the direction where it is maximized. Gain may be given as scalar value instead of a function of the angle, which implies the gain in the direction of maximum radiation.

$$G(\theta, \phi) = 10 \log_{10}(\frac{4\pi e_r U(\theta, \phi)}{P_{in}}) \tag{2.10}$$

The radiation pattern is discussed in terms of two principal planes containing the E_θ and H_ϕ components of a transmitted wave. The E-Plane pattern for a dipole oriented along the z-axis consists of sweeping the angle θ for a given ϕ [72]. Also, the H-Plane pattern consists of sweeping the angle ϕ for a given θ [72]. These angles are defined in Figure 2.1.

2.1.1 Baluns

A balun attaches an unbalanced load/line to a balanced load/line. A coaxial transmission line is an unbalanced line. An external ground plane from the transmission line structure such as a coaxial line needs to have equal capacitance to both the signal and the return in order for the structure to be a balanced line [47]. Currents on the third conductor or ground can off-balance the current distribution of an antenna. The coax shield may support undesirable currents off-balancing the antenna. Therefore, a balun will ensure the currents are distributed properly on a balanced antenna when fed from an unbalanced transmission line.

There are many different balun configurations with advantages and disadvantages. A common balun for dipoles is a bazooka balun. This configuration has a $\lambda/4$ length metal sleeve that covers the coax at the feed point of the antenna [8]. This $\lambda/4$ section acts as a high impedance transmission line for return currents coupled onto the outer conductor. Since the sleeve section is $\lambda/4$ long, this high impedance has a peak at the frequency corresponding with the λ and falls off either for increasing or decreasing frequencies. Therefore, this is a narrowband balun. There are a few other similar balun configurations based on this same principle, but none of them are applicable to the wideband dipole.

Other implementations of baluns include planar designs and lumped circuits. Planar designs include Marchand and Guanella, but these designs are limited due to the size constraints of the design. Therefore, these are mainly used at higher frequencies and are not suitable for a size constrained VHF antenna.

2.1.2 The Bow-Tie Antenna

Since it is often desirable to increase the bandwidth of a dipole in a planar configuration, the design is modified. To a certain degree, increasing the wire thickness will increase the bandwidth of the a dipole [72]. However, this increase is sometimes not sufficient. A dipole with flared edges and a fixed angle introduces the structure of a biconical antenna, which is the three dimensional equivalent to a bow-tie antenna. The finite biconical antenna has reflections at the cone ends that cause standing waves and a complex input impedance, and similarly, the currents are abruptly terminated at the bow-tie ends, which limit their bandwidth [72]. Furthermore, the near-field sphere around the biconical antenna consists of both Transverse Electromagnetic (TEM) waves and higher-order modes created at the cones that significantly increase the imaginary component of the input impedance [72]. These same fields are present for the planar version of the biconical or the bow-tie antenna.

2.2 Brief Introduction to Array Theory

As antennas get longer, the main radiation beams become narrower or their gain increases. Arranging multiple antennas in space can accomplish this same increased gain. When antennas are arranged like this then it is an antenna array. Unlike large antennas, the amplitudes of the currents on each antenna can be weighted to reduce sidelobes, and the phase can be adjusted to direct the array [8]. The array is often considered in regards to its array factor (AF), which is the array radiation pattern

when the antennas are replaced with point sources [72]. An incoming plane wave to a planar array is incident at an angle (θ) from the axis of the antenna elements. There is a phase shift of the incoming plane wave by k times the distance between elements, and one element is considered the reference element that does not have a phase shift [72]. The distance term is converted into spherical coordinates. A planar array lying on the xz-axis is shown in Figure 2.2. The phase shift between the two elements lying along the z-axis (or parallel to the z-axis) is kdzcos(θ) and labeled $\Delta\Phi z$ in the figure. Similarly, the phase shift between two elements lying along the x-axis (or parallel to the x-axis) is kdxsin(θ) cos(ϕ) or $\Delta\Phi x$. Although not shown in the figure, the phase shift for elements along the y-axis is kdysin(θ) sin(ϕ) or $\Delta\Phi y$, with dy being the distance between two point sources along the y-axis. The angle ϕ is defined from the x-axis towards the y-axis. The relationship between the Cartesian coordinate system and spherical angles is shown in Figure 2.1. Therefore, the angle ϕ in Figure 2.2 is constant and is pointed along the x-axis, so it is zero.

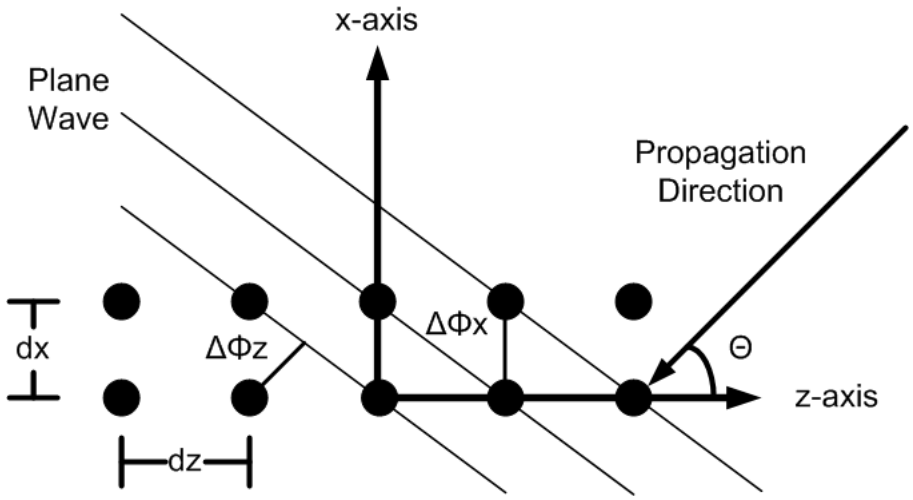

Figure 2.2: Isotropic Point Sources Lying on z- and x-axis

Each point source has a corresponding current element (I_n) and phase relationship with the reference point source. This can be expressed for the full array factor as in Equation 2.11 [72]. Each $\Delta\Phi x$ represents the phase shift from that point source to the reference. This equation allows for arrays with variations along each axis to be defined using the array factor. Note that the array factor is often expressed in decibels, so this

would be $10\log_{10}(AF)$.

$$\begin{aligned} AF = I_0 &+ I_1 e^{j(\Delta\Phi x1 + \Delta\Phi y1 + \Delta\Phi z1)} \\ &+ I_2 e^{j(\Delta\Phi x2 + \Delta\Phi y2 + \Delta\Phi z2)} + ... \\ &+ I_N e^{j(\Delta\Phi xN + \Delta\Phi yN + \Delta\Phi zN)} \end{aligned} \tag{2.11}$$

The main beam direction with respect to the axis of the array can either be considered a broadside array, where the main beam is normal to the axis ($\theta = 90°$), or an ordinary end-fire array, where the maximum is along the axis of the array ($\theta = 0°$ or $180°$) [8]. A broadside array is the type used for the NASA P-3 aircraft. Obviously, an end-fire array extending from an aircraft would not be aerodynamic.

The separation between point sources or antenna elements is critical for producing an array factor with decent gain and no grating lobes, which are principle maxima in other directions other than the main beam [8]. The grating lobes can be avoided if the spacing between elements is less than λ [8].

Each point source also has a current weight along with the phase term. The current amplitude can be adjusted to change the main beamwidth and the relative side lobe amplitudes. An adjustment to narrow the main beam will raise the side lobes, and an adjustment to lower the side lobes will widen the main beam [72]. The current amplitude schemes are often called weighting functions. If the weighting function reduces the side lobes or has a current distribution that is smaller at the end elements, then it may be referred to as a taper. If the weighting function narrows the main beam, then the weights are greater on the end elements than the center elements. This is called an inverse-taper. Many tapers have been developed to achieve low side lobes with a minimum increase in the main beamwidth, such as the Hanning and the Chebychev.

A taper is desirable for most applications to reduce the sidelobes, which is particularly useful for remote sensing when minimizing the radar return from clutter. Side lobes increase the gain in an undesired direction or to the side of the main beam. This direction consists of other objects rather than the main target, which the main beam is pointing towards. These extra objects that reflect the signal and contaminate the signal from the main beam are called clutter [69]. In the case of aerial remote sensing of glaciers, clutter can be on the surface or interior to the ice. Clutter creating the biggest impact on the radar performance can be caused by water, which reflects more energy than the surrounding ice. Therefore, increasing the number of elements within the array enables advanced signal processing that improves the capabilities of the radar system.

2.2.1 Mutual Coupling

Array elements interact with each other causing changes in the current magnitude, phase and distribution on each element, and this interaction is called mutual coupling [72]. An isolated antenna's input impedance is altered under the presence of mutual coupling [17]. As mentioned earlier, near-field objects, especially metallic, change the input impedance of an antenna element. Adjacent antenna elements are metallic, so similar effects are expected. Also, some energy transmitted on one antenna is coupled onto the other antenna within the array based on the mutual impedance (a metric for qualifying the mutual coupling). The magnitude of the coupling is a function of the following [8]:

1. Radiation characteristics of each antenna
2. Relative separation between each element
3. Relative orientation of each element

Mutual coupling affects both the radiation pattern and the received power at each antenna. An input signal excites currents that radiate, but some of the radiated energy induces currents on nearby antennas, which will then re-radiate some energy from these induced currents. Therefore, the antenna with the signal at its input port radiates an intentional field, while the induced current onto the nearby antenna produces an unintentional field. Each element in the array will have this process occur. Therefore, the far-field radiation pattern is the vector sum of each of these excitations, both intentional and unintentional [4].

A similar concept is true for the received power of each antenna within the array. The incoming wave excites currents at each antenna, and these currents will cause some of the energy to be re-radiated, which will couple onto nearby antennas. Therefore, the total energy received from the incident wave at each antenna is a combination of the direct energy and re-radiated energy from nearby antennas [4]. The received energy will arrive in two paths: a direct case and a re-radiated case. The re-radiated energy will be delayed from the direct wave. The reception of two waves at different time intervals will interfere with the data and cause ambiguities on the received signal.

Mutual coupling causes the illumination of incoming plane waves to not be uniform and vary with the angle of arrival [23]. The estimation of angle of arrival has been used to map the bed topography, so calibrating and minimizing the mutual coupling needs to be done [51, 52]. Therefore, minimization of the mutual coupling will increase the purity of the received signal without interference from nearby antennas.

The mutual coupling can have an effect on the radiation pattern of the array as well. Mutual coupling may raise the sidelobes of the array pattern, and generally affects the closest sidelobes [4]. If the antenna elements are fed individually, then the efficiency will be affected but not the pattern [17]. Consideration to the mutual coupling effects on the radiation pattern may be important, but the array elements considered are individually fed.

This process of mutual coupling can also be represented as a network of mutual impedances. Each element has an induced voltage and current that can be expressed as V_n and I_n. The impedances can be written as Z_{mn}, which represent the impedance from the m$^{\text{th}}$ element to the n$^{\text{th}}$ element. This is expanded in Equation 2.12 [72]:

$$\begin{aligned} V_1 &= Z_{11}I_1 + Z_{12}I_2 + ... + Z_{1N}I_N \\ V_2 &= Z_{12}I_1 + Z_{22}I_2 + ... + Z_{2N}I_N \\ &\vdots \\ V_N &= Z_{1N}I_1 + Z_{2N}I_2 + ... + Z_{NN}I_N \end{aligned} \tag{2.12}$$

Therefore, the impedance from one antenna to another can be found if one antenna has an open-circuit to remove the current, and the other antenna is excited with a voltage. This is shown in Equation 2.13 where I_m is equal to zero [72].

$$Z_{mn} = \frac{V_m}{In} \tag{2.13}$$

However, 2.12 can be written using Ohm's Law as shown in Equation 2.14 [72]:

$$Z_{mn} = \frac{V_m}{I_m} = Z_{m1}\frac{I_1}{I_m} + Z_{m2}\frac{I_2}{I_m} + \cdots + Z_{mN}\frac{I_N}{I_m} \tag{2.14}$$

These equations show that there is an impedance between each antenna that characterizes the coupling path for energy to be induced onto neighboring elements. Since impedance is defined as a ratio of voltage and current, then the signal voltage level at one antenna and the mutual impedance establishes the magnitude of current on the other antenna. As mentioned above in Section 2.1, currents are fundamental for radiation, so these changes in currents create different radiation patterns and alter the antenna's performance if it were not in an array. Also, these induced currents will affect the input impedance of the antenna, which is related to bandwidth. Since impedance is complex, results for mutual coupling will be shown as real and imaginary components.

These results will also be represented in decibels S-parameters as measured with a network analyzer.

As mentioned, mutual coupling can affect the input impedance and current distribution on each antenna. Two antennas in close proximity will have a mutual impedance. Equation 2.12 indicates that if either antenna has a current traveling then a voltage will be present at the terminal of the other antenna. One antenna can be considered as a parasitic element, in that there is not a generator exciting currents intentionally on the element. Considering the case where two antennas are in close proximity to each other such that the current on one affects the input impedance of the other. Equation 2.15 shows the voltage induced on antenna one.

$$V_1 = Z_{11}I_1 + Z_{12}I_2 \tag{2.15}$$

Antenna one has a load impedance denoted by Z_1, when no current is used to excite it. The voltage across antenna one port will be equal to Z_1 multiplied by the current along antenna one, I_1. If antenna one is not excited with a voltage across the input port, then the current will be directed in the opposite direction of antenna two. The reason for this relates to the boundary condition on a conductor causing an induced voltage equal in magnitude but opposite in direction as the incident electric field along a line [58]. A more thorough explanation is provided in Appendix A. The current on antenna one will then be denoted with a negative sign. The magnitude of the current will depend on the mutual impedance between the two antennas and the current on the second antenna. Equation 2.15 can then be written as the following [72].

$$-Z_1I_1 = Z_{11}I_1 + Z_{12}I_2 \tag{2.16}$$

This can be solved for the current existing on element one.

$$-Z_1I_1 - Z_{11}I_1 = Z_{12}I_2 \tag{2.17}$$

$$I_1 = \frac{Z_{12}I_2}{-Z_1 - Z_{11}} = \frac{-Z_{12}I_2}{Z_1 + Z_{11}} \tag{2.18}$$

This indicates that if element one is a parasitic element and is not excited with a voltage, then there will exist a current traveling on it. Since a current is traveling on antenna one, then this antenna will radiate and effect the current on antenna two. The same procedure used for finding the current on antenna one above can be used for

antenna two as shown below [72].

$$I_2 = \frac{Z_{21} I_1}{-Z_2 - Z_{22}} = \frac{-Z_{21} I_1}{Z_2 + Z_{22}} \tag{2.19}$$

Of course the input impedance for either antenna is defined as the voltage divided by the current by Ohm's Law [72]. Therefore, the induced currents due to the other antenna will inevitably impact the input impedance of both antennas. The stronger the coupling the larger this impact. The impedance is inversely proportional to the current, so as the current increases, the input impedance can be expected to decrease.

The expressions above describe the coupling in terms of circuit elements, but a more general equation relates the physics to the coupling. This equation is shown in Equation 2.20 [43]. It is assumed that both the current source and the receiving element are oriented vertically along the z-axis. This equation shows that the coupling between two current elements is determined by the sum of the currents along the source and the contributions of electric field from discrete points along the current element. This is generalized to any current elements but can be applied to specific antenna types. Also, this shows that the coupling is inversely proportional to the currents on both the transmitting and receiving elements. This is a result of the definition of impedance being voltage over the current defined by Ohm's Law. Furthermore, the negative sign comes from the boundary condition enforced on a conductor demanding an equal and opposite electric field over a line or voltage [58]. While this equation illustrates some of the physics of the energy coupled from a current source to a receiving element, it is often best calculated with numerical tools due to the complexity of practical sources. One recommend technique is the Method of Moments, which solves the currents along conductors [58]. The derivation for this equation is shown in the Appendix A.

$$Z_{21} = -\frac{1}{I_1(0) I_2(0)} \int E_{z21} I_2(z') dz' \tag{2.20}$$

2.3 Fundamentals of Mutual Reactance

The fundamental physics of electromagnetic field coupling is either capacitive or inductive. These fundamentals are discussed for problems defined in the near-field or where the electromagnetic energy is not considered a plane wave. Plane waves can couple energy in the antenna far-field. Mutual reactance is not limited to antenna fields coupling but is applicable to many applications. Charges and currents produce fields that are related through mutual reactance. These interactions of fields or signals are often undesirable and can cause devices to operate differently than if these interactions

were not considered. In this section, the physics for capacitive and inductive coupling will be described to better understand the physics of mutual coupling in arrays and other devices, such as twisted-pair transformer baluns. While the fundamentals explain the physics for simplified situations, practical problems are more complex. The fundamental physics explained here

2.3.1 Fundamentals of Mutual Capacitance

The following discussion is based on the fundamental coupling for close proximity problems and will begin with capacitive coupling. Capacitance is defined as the charge on each electrode per volt of potential difference or voltage between the electrodes as shown in Equation 2.21 with units of Coulomb per volt or Farads (F) [58].

$$C = \frac{Q}{V} \tag{2.21}$$

A general equation for capacitance can be derived from the relationships of voltage and charge with the electric field. First, voltage is the negative change in electric field from one point to another along a line, which can become positive from reversing the direction of integration. Positive voltage requires integrating from the point where positive charges are accumulated (positive potential) to the negative charge region (negative potential). Second, charge density on an electrode is the normal component electric flux density ($\mathbf{B}$), which is defined as the relative permittivity times the electric field. Therefore, the total charge on the electrode is the surface integration of the charge density. These relationships are fully represented in Equation 2.22, where S_- is the surface with the negative potential and S_+ is the surface with the positive potential [15].

$$C = \frac{\oint_{S_-} \epsilon \mathbf{E} \cdot \mathbf{ds}}{\int_{S_-}^{S_+} \mathbf{E} \cdot \mathbf{dl}} \tag{2.22}$$

2.3.2 Fundamentals of Mutual Inductance

Before discussing mutual inductance, self inductance must be introduced. Faraday's Law of Induction states that a time-varying magnetic flux around a closed path creates a net voltage and is shown mathematically in Equation 2.23 [15]. Induced currents from the time-varying magnetic field tend to oppose the time-varying flux linkage, which is called Lenz's Law [15]. The flux linkage is the magnetic flux passing through a current

path and is $\int_S \mathbf{B} \cdot \mathbf{ds}$ [15].

$$\oint_C \mathbf{E} \cdot \mathbf{dl} = -\frac{\partial d}{\partial t} \int_S \mathbf{B} \cdot \mathbf{ds} \tag{2.23}$$

Faraday's Law relates a time-varying magnetic field through a closed path with an induced voltage, which is the difference in electric fields from point a to point b [58]. Now inductance can be defined as the magnetic flux linkage per unit of current and mathematically described in Equation 2.24 [58].

$$L = \frac{\int_S \mathbf{B} \cdot \mathbf{ds}}{I} \tag{2.24}$$

The induced voltage (the negative of the left hand side of Equation 2.23) from a time varying field can be written in terms of the inductance and current. Substituting Equation 2.24 into Faraday's Law and calling the negative of the left side the induced voltage produces this relationship as shown in Equation 2.25 [58]. Note that the negative induced voltage means that the potential difference is opposite of the defined contour for the electric field.

$$-V_{induced} = \frac{d}{dt}(LI) \tag{2.25}$$

The mutual inductance term requires the development of further background theory. The magnetic vector potential ($\mathbf{A}$ with units of webers per meter or tesla-meters) is introduced as an intermediate variable [58]. It is shown in Equation 2.26, and its relationship with the magnetic field in Equation 2.27 [15].

$$\mathbf{A} = \frac{\mu_o}{4\pi} \int_{Volume} \frac{\mathbf{J} dv'}{|\mathbf{r} - \mathbf{r}'|} = \frac{\mu_o}{4\pi} \int_{Contour} \frac{\mathbf{I} dl'}{|\mathbf{r} - \mathbf{r}'|} \tag{2.26}$$

$$\mathbf{B} = \nabla \times \mathbf{A} \tag{2.27}$$

$\mathbf{J}$ is the current density with units of A/m^2 for a volume current and can be found by multiplying the conductivity to the electric field. In addition, $\mathbf{r}$ is the position vector where $\mathbf{A}$ is being evaluated, and $\mathbf{r}'$ is the position vector that is swept through all locations where the current density is nonzero [15]. The mutual inductance is defined as the flux linkage between current 2 to current 1 divided by current 1 and is shown in

Equation 2.28 [15].

$$\begin{aligned} L_{21} &= \frac{\text{Flux Linkage from Current 2 to Current 1}}{I_2} \\ &= \frac{\int_{S_1} \mathbf{B_2} \cdot \mathbf{ds}}{I_2} \\ &= \frac{1}{I_2} \int_{S_1} \nabla \times \mathbf{A}_2 \cdot \mathbf{ds} \end{aligned} \tag{2.28}$$

Equation 2.28 can be reduced by applying Stokes Theorem in Equation 2.29 [15] and this reduction is shown in Equation 2.31.

$$\oint_C \mathbf{F} \cdot \mathbf{dl} = \int_S \nabla \times \mathbf{F} \cdot \mathbf{ds} \tag{2.29}$$

$$L_{21} = \frac{1}{I_2} \oint_{C_1} \mathbf{A}_2 \cdot \mathbf{dl}_1 \tag{2.30}$$

Then the Equation 2.26 can be inserted into Equation 2.31 to arrive at the Neumann formula for mutual inductance [15]. The Neumann formula is commonly used to describe the magnetic flux linkage between two current elements around closed paths. Therefore, two currents will interact due to their magnetic fields, and this equation can be applied to quantify the amount of energy coupled.

$$L_{21} = \frac{\mu_o}{4\pi} \oint_{C_1} \oint_{C_2} \frac{\mathbf{dl}_1 \cdot \mathbf{dl}_2}{|\mathbf{r}_2 - \mathbf{r}_1|} \tag{2.31}$$

2.4 Parasitic Elements

Parasitic elements were first introduced by Uda and Yagi in 1926 and 1928, respectively [74, 78]. The configuration described in their work utilized a beam "director" and a beam "reflector" to create directive radio transmission. The director has a resonant frequency higher than the wave, while the reflector has a lower resonant frequency than the incident wave [78]. The directors positioned in front of the antenna will make a narrower beam or a higher gain in the z-direction as indicated by Figure 2.3.

Both the reflector and the directors are considered parasitic elements, since they are not excited with a source like the driven element. Analysis of Yagi-Uda antennas has been done extensively to develop optimal configurations for maximum radiation after Yagi and Uda experimentally proved the concept [13, 14, 33, 45, 46, 73]. The combination of directors and reflectors launch a wave that has a phase velocity less

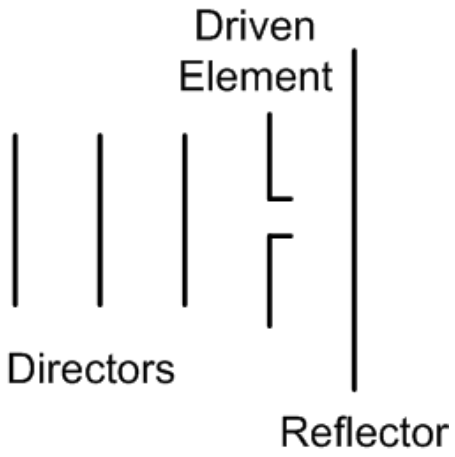

Figure 2.3: Yagi-Uda Antenna

than the speed of light or a phase delay that is greater per unit distance along the axis for the array [72]. The infinite and finite Yagi-Uda excite a guided wave along the array that has a critical point where the wave does not become slower [45, 46]. Therefore, the fundamental wave-guiding operation of the Yagi-Uda has a limit due to the phase delay. The ability for a Yagi-Uda array to guide waves is based on the driver exciting a wave both towards the reflector and the directors. Each parasite has an incident electric field that then produces a negative of the incident electric field to fulfill the boundary condition (tangential electric field = 0) [72]. Therefore, the current excited on the parasite has the opposite phase as the incident electric field, and the parasite can be equated to an equal amplitude and opposite phase antenna [72]. This assumption that the parasite will become an element is dependent on the parasites capability to radiate. The current is excited due to the incident field regardless of the radiation characteristics of the antenna, such as the radiation resistance and the resonant frequency. If the parasite does radiate well, then array theory can be utilized, and this array is considered end-fire. The optimization of the array depends on the currents excited on each of the parasites. These induced currents are described through mutual impedance relationships between the driven element and each of the parasites, even from one parasite to the next. The summation of all the complex currents on each element determines the radiation characteristics of the Yagi-Uda antenna [13, 14, 33]. The currents induced on the parasites convert the nearby metallic object into an antenna element forming an array, and the radiation characteristics can be controlled through the placement of the parasitic elements.

The parasitic elements discussed for Yagi-Uda antennas are utilized for gain

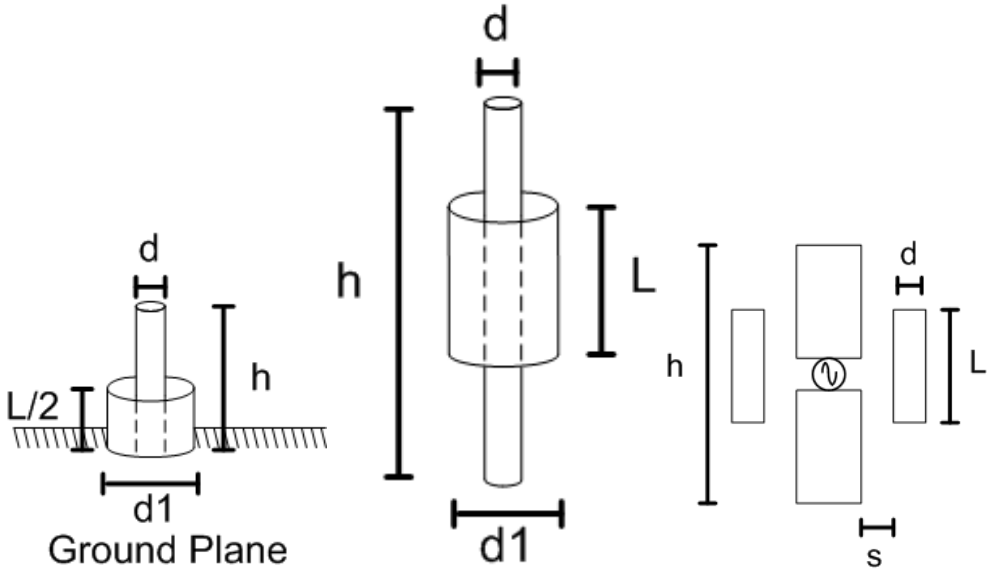

(a) Sleeve Monopole (b) Sleeve Dipole (c) Planar Open-Sleeve Dipole

Figure 2.4: Sleeve Antenna Configurations

enhancement, but other parasites are used to increase the bandwidth. A common type of antenna that utilizes parasitic elements to enhance bandwidth is the sleeve antenna. A few variations of the sleeve antenna are shown in Figure 2.4.

The analysis of the sleeve antenna is based on asymmetric feeding and the superposition of the currents from two equivalent antennas [35]. The sleeve is assumed to confine the currents to the interior closest to the antenna. The sleeve that is shown in Figure 2.4a extends the gap between the excitation source and the ground plane to a height of L above the ground plane [35]. A monopole is based on image theory, where the equivalent circuit is a dipole [72]. Image theory is extended to the sleeve monopole case as well. Since Maxwell's equations are linear, superposition can be applied to make an equivalent antenna with two different positions for the source [35]. Therefore, the equivalent sleeve monopole has two different feed locations located at L/2 above the ground plane and L/2 below the ground plane. This decomposition of sources into equivalent antennas is shown in Figure 2.5 [35].

The same principle of equivalent antennas is applicable to the sleeve dipole, but the principle has some approximations. First, the feed for a monopole antenna is between the monopole and the ground plane, so the sleeve extends the ground plane and the location of the feed to a higher location along the height of the monopole. On the other hand, the feed for a dipole is between two halves of the antenna. The addition of

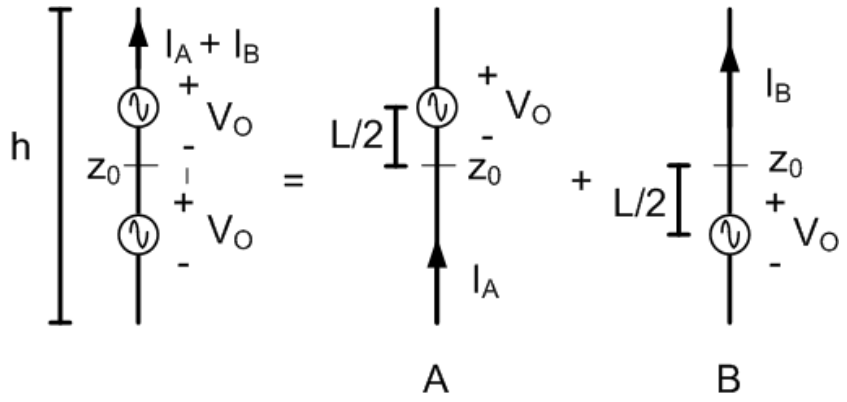

Figure 2.5: Decomposing the Sleeve Monopole into Equivalent Asymmetrical Antennas

the sleeve does not extend the feed along the length of the dipole, because the sleeve for the dipole antenna is detached from the antenna and not connected to the lower half. Therefore, the sleeve dipole feed is not the same as the sleeve monopole feed. The equivalent antenna approximation is still used for the sleeve dipole, but the theory diverges more from practice than for the sleeve monopole due to this difference. The equivalent antenna approximation is still used, because there are still currents that are coupled onto the sleeve and appear to move the feed position. The approximation for the sleeve dipole is still used with the understanding that there would need to be a correction for this geometry difference [35]. Similarly, the open-sleeve dipole can either be planar or cylindrical, and the sleeve is replaced with at least two wires [31]. The driven antenna excites currents on the parasitic wires or metallic strips next to the antenna as shown in Figure 2.4c as occurs with a cylindrical or coaxial sleeve surrounding the input. Therefore, the effects of the parasitic strips are similar to the sleeve dipole.

As mentioned, the sleeve dipole is often designed for wide band performance. The equivalent impedances can be optimized to balance the input reactance such that when one reactance is high the other is low at a particular frequency [35]. As the two reactances sum to zero, the antenna more efficiently radiates without increasing the energy stored in the reactive near-field. Some performance results have shown large increases in bandwidths for dipoles with the addition of the sleeve. In one example, the open-sleeve dipole was reported to have impedance bandwidths up to 1.8:1 [34]. In addition, a planar open-sleeve dipole utilizing end-loading elements was reported to achieve 50% bandwidth with a center frequency around 1 GHz as shown in Figure 2.6 [71].

The radiation patterns for asymmetric antennas are also subject to influence. The

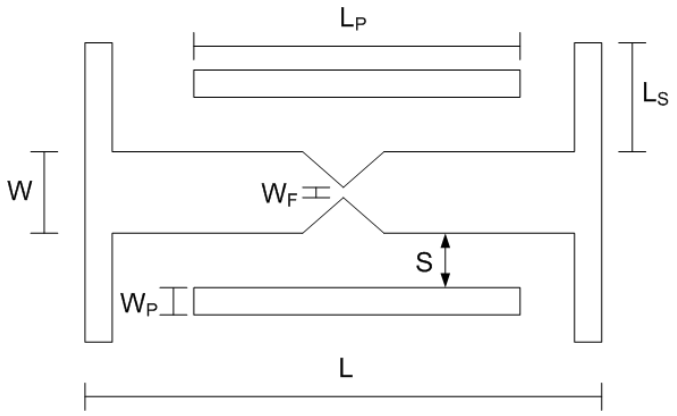

Figure 2.6: End-Loaded Planar Open-Sleeve Dipole [71]

relative phase along antennas longer than a half-wavelength varies with the feeding position and influences the pattern [76]. The antenna current distribution for a sinusoidal input is not equally distributed for an asymmetric antenna. Effects are less notable for shorter antennas due to the ends forcing the current to zero [76].

Chapter 3

Array Design Revision 1

The design and performance of the first revision of the array is discussed in this chapter. The array consists of 15-modified, dipole antennas. These elements were integrated within an an aerospace fairing, and analysis was done to predict antenna performance within this structure. Also, a balun was designed and selected to perform for high power and throughout the frequency band. Overall, the first array revision had several areas for improvement in regards to antenna performance, which are introduced here.

3.1 Antenna Elements

The antenna was designed by Dr. Ayyangar Harish utilizing dual wings on each dipole half to create a dual resonance and widen the antenna bandwidth. This concept was shown by Joshi and Harish [32]. For the first revision, the elements were not modified from this design, and an HFSS simulation result showing the bandwidth is presented in Figure 3.1. Also, the dimensions of the first antenna are shown in Figure 3.2.

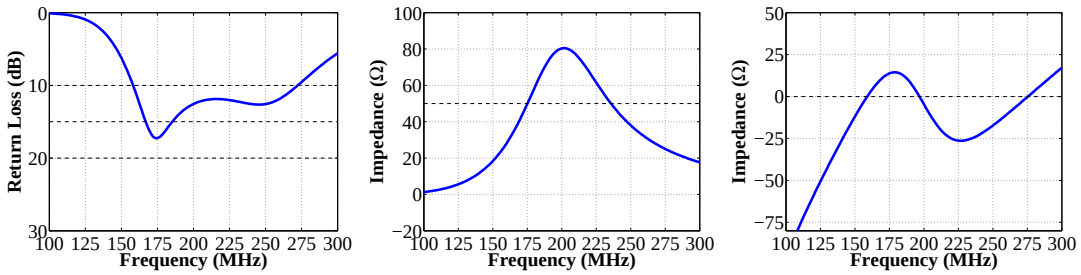

(a) Return Loss (b) Real Input Impedance (c) Imaginary Input Impedance

Figure 3.1: Free-Space Simulations Results for the Rev. 1 Antenna

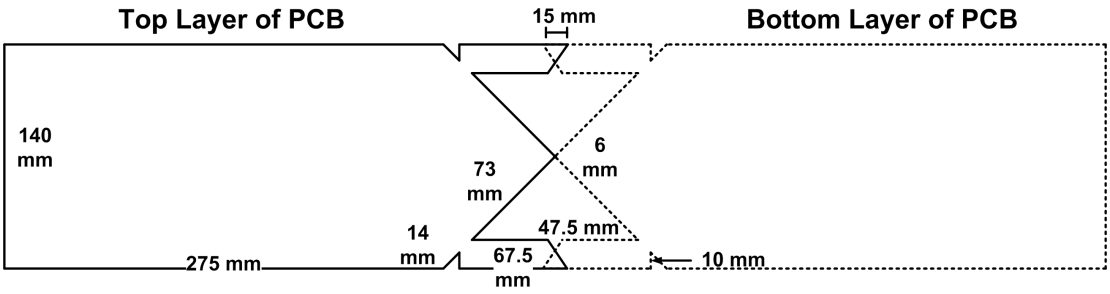

Figure 3.2: Revision 1 Antenna Dimensions

3.2 Balun

The balun for the antenna shown in Section 3.1 was designed to achieve a wide-bandwidth at VHF and operate with a peak input power of at least 300 Watts. There are several types of baluns capable of feeding a dipole, but achieving a wide-bandwidth and high power design limits the available balun types. The selected balun was a ferrite transmission line transformer. The ferrite transmission line transformer could withstand power levels exceeding 300 W and meet the bandwidth requirement.

Radar performance is improved by increasing the signal-to-noise ratio (SNR), and one way that this is accomplished is by transmitting at higher powers. The propagation of the waveform experiences loss through air and then through the ice for a two-way travel. The two-way propagation through the ice ranges from 166.8–174.6 dB across the frequency range 110–500 MHz [53]. Overcoming these losses requires transmitting at higher powers, so the balun should be capable of performing at higher currents.

Characterization and design of ferrite transmission line transformers is primarily experimental [49, 60, 65, 66]. A test to characterized the balun's performance. The metrics include temperature change of the core and the ability for the balun to maintain a equal magnitude and 180° phase difference between two sinusoids. The test setup for measuring the balun is shown in Figure 3.3. The data was measured in the time-domain using an oscilloscope (Tektronix DPO 4104). The signal was provided using an Agilent Arbitrary Waveform Generator 33250A to pulse the Agilent Signal Generator 8648D, which provides the sine wave into the input of port 1 on the test jig as shown in Figure 3.5 except with 25 Ω resistors on the output ports to ground and 1 MΩ oscilloscope input. Each output from the balun when feeding the antenna has 25 Ω connected to each port. The amplifier used to produce the signal was a 400 W Hurley AMT 3304C solid-state amplifier. Each temperature measurement was done with a 255 W (+54 dBm) signal at the input of the balun. Two different size ferrite binocular core baluns were

measured. A smaller core (Fair-Rite Part Number 2843010302) and a larger core (Fair-Rite Part Number 2843009902) were measured, and the results are shown in Figure 3.4. The larger binocular core was wound with 20 AWG wire, and the smaller core was wound with 24 AWG wire. The results indicate that the smaller core was much more susceptible to heating due to the high power. The larger core experienced heating as well, but the temperature increase was not sufficient.

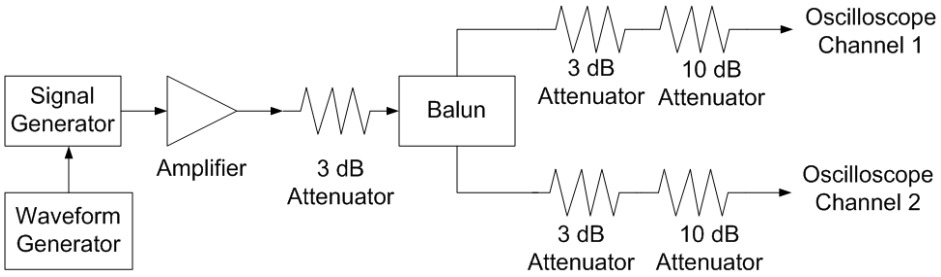

Figure 3.3: Balun Temperature Test Setup

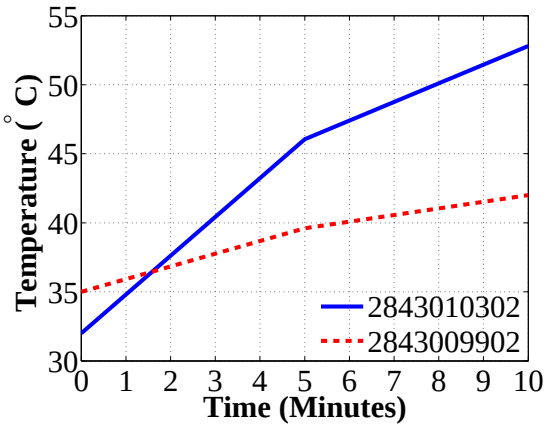

Figure 3.4: Balun Temperature Test

Later, a 4-port network analyzer (Agilent N5230C) was used to directly measure the S-parameters of the balun. A test jig with a common ground was constructed utilizing SMA connectors at each port of the balun as shown in Figure 3.5. The results are represented in Figure 3.6. First, the variations for each terminal match shows the variation in the design of the balun since each terminal has its own characteristics. The output ports (two and three) show the strongest agreement, but do diverge greatly starting at around 190 MHz. Also the transfer functions from the input to the output ports (S21 and S31) shows some variation increasing at around 200 MHz. A 3 dB loss

is expected since the power is split between two ports, because 3 dB is a factor of two in linear, which represents half the power for a loss. Therefore, the insertion loss can be stated to be 1 dB at 100 MHz and increase with frequency. It is undesirable that the power delivered to each port is not equal, because this will cause the dipole to have unequal currents on each half.

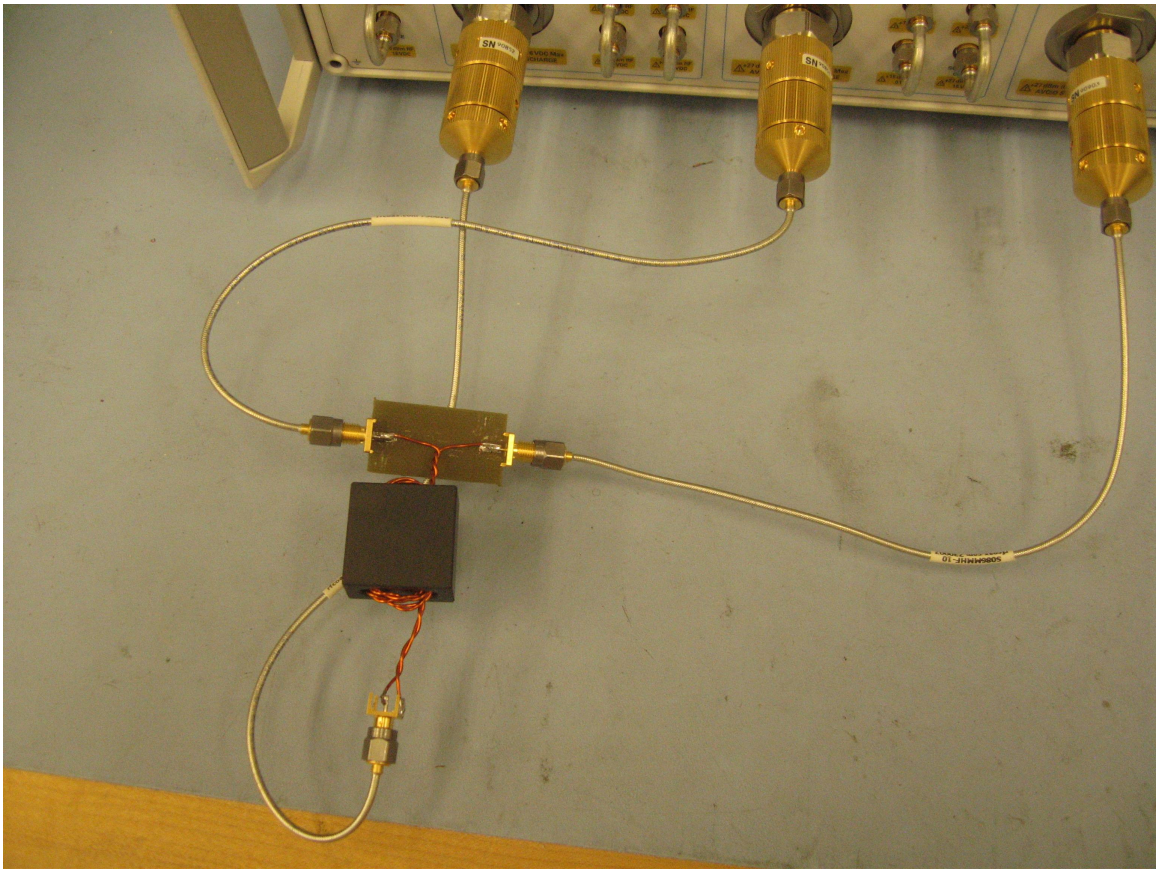

Figure 3.5: Balun Original Test Jig

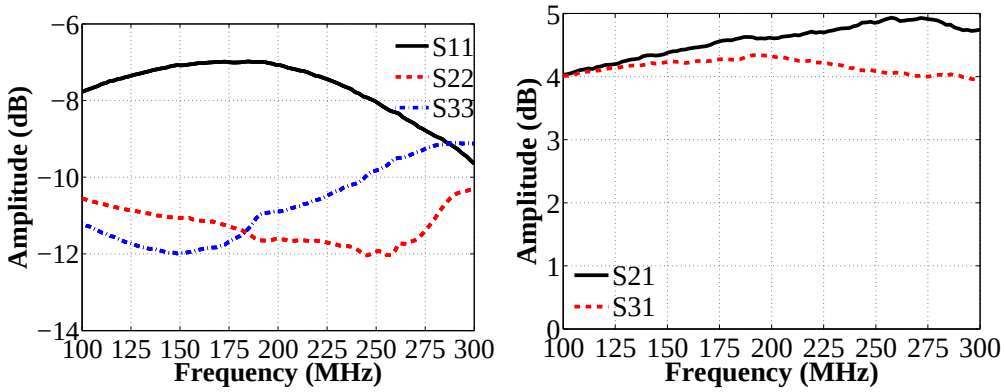

(a) Terminal Matches

(b) Loss to Each Output

Figure 3.6: Revision 1 Balun

3.3 Integration with fairing

The full P-3 array consists of three smaller arrays: two on each wing referred to as outboard arrays and one in the center of the aircraft referred to as the inboard arrays. These configurations are shown in Figures 3.7 and 3.8 [75]. The fairing is primarily composed of S2-fiberglass and aluminum. The S2-fiberglass has a dielectric permittivity of 5.2 [3]. There are several aluminum components included in the fairing to add structural support. Each of these components is positioned in the near-field of the antenna, and therefore they affect the input impedance. The fairing includes pylons, ribs, gang channels, screws, doublers and miscellaneous smaller aluminum components shown in Figure 3.8. The antennas attach to the skin, which is screwed into the rest of the fairing. Inside the skin is a layer of Rohacell foam (71 IG) with a dielectric constant of 1.08 up to 2.5 GHz [19]. This decreases the relative permittivity of the composite S2-fiberglass underneath the antennas. The complexity of these fairings to meet structural requirements was driven by strict NASA requirements for consideration to the fairing and the aircraft [25].

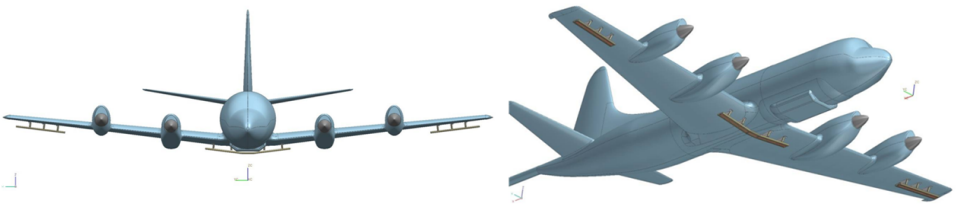

(a) P3 with Fairings (Front View) (b) P3 with Fairings (Belly View)

Figure 3.7: P-3 and Fairing Layouts [75]

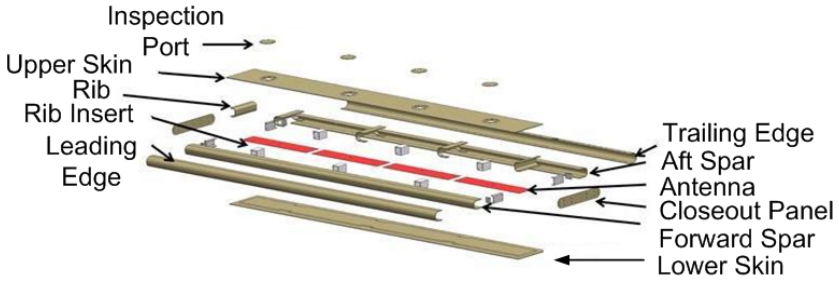

(a) Fairing Layout

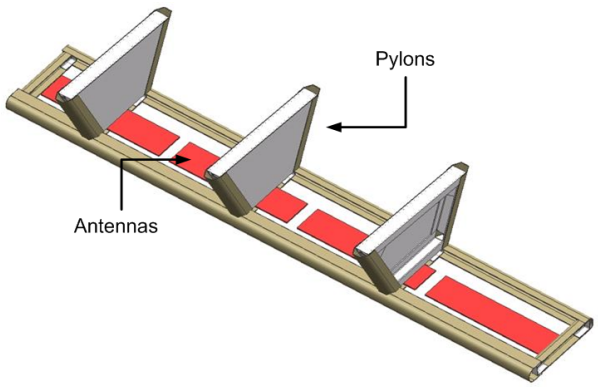

(b) Pylons with Fairing

Figure 3.8: Fairing Layouts

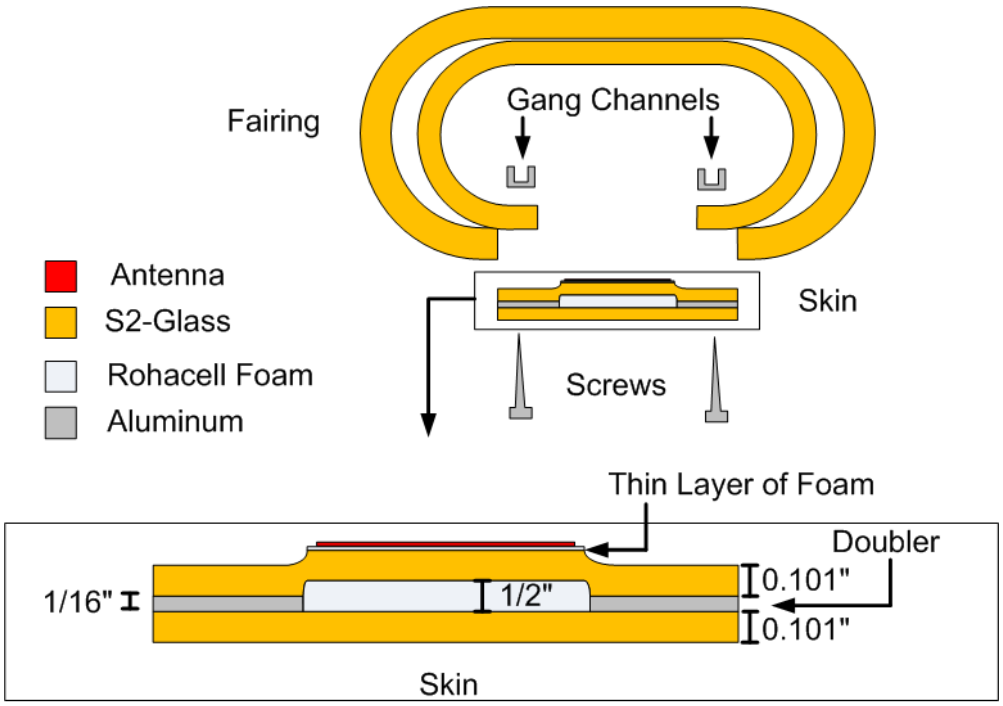

Figure 3.9: Side Sectional View of Fairing

3.3.1 Gang Channels and Doublers

As discussed in the previous section, there were metallic objects positioned alongside the antennas to construct the aerospace fairing. During the first revision, both the gang channels and the doublers were originally designed to be long, unbroken sections parallel to the antennas. Before deploying this design, measures were taken to improve antenna performance. In this section, the impact of long conductors parallel to antennas will be discussed before providing details about the gang channel and doubler configurations as deployed with results.

Conductors in close proximity to antennas can be positioned to improve performance as discussed in Section 2.4, but generally there is a negative impact on performance. At the boundary of a conductor, the sum of tangential electric fields along a closed path must be equal to zero [58]. The contributions due to the sides are negligible assuming a infinitesimal distance inside the conductor, so the tangential fields have opposite signs and the same magnitude. Consider a conductor approaching an electric field source. As the conductor approaches an infinitesimal distance from the source, this opposing voltage will cancel the source and essentially short-circuit the source. A dipole was simulated in free-space in order to compare the effect of the close conductors, and these results are shown in Figure 3.10. First, this effect is illustrated with a ground plane at

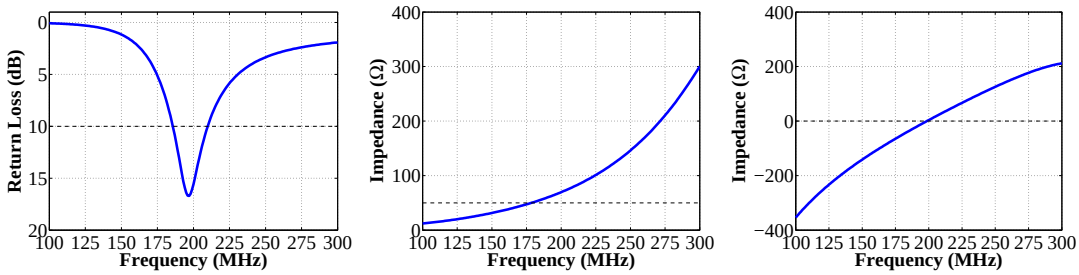

(a) Return Loss (b) Real Input Impedance (c) Imaginary Input Impedance

Figure 3.10: Dipole Free-Space

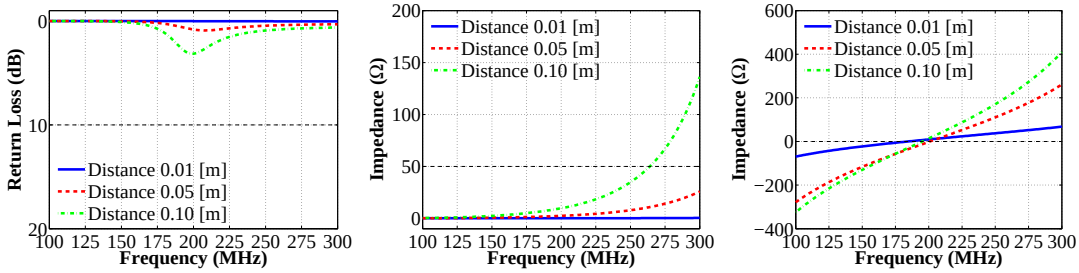

(a) Return Loss (b) Real Input Impedance (c) Imaginary Input Impedance

Figure 3.11: Ground Plane Close-Proximity to Dipole

a few different locations as shown in Figure 3.11. The separation is intervals of 0.01, 0.05 and 0.1 meters, which corresponds to 0.0067λ, 0.033λ and 0.067λ, respectively at 200 MHz (the resonant frequency of the dipole in free-space). When the ground plane is 0.01 meters from the antenna, all the power is reflected at the input port, and the radiation resistance is 0 Ω. As the ground plane is moved a little further from the antenna this effect is reduced, but is is very prominent for narrow separations. The radiation resistance is not near 50 Ω when the antenna is resonant, so the return loss is never better than 5 dB for these distances.

While the ground plane simulation illustrates the boundary conditions of a good conductor, the ground plane is much larger than the antenna and is not the same shape as the gang channels and doublers. A study where one conducting cylinder the same length of the dipole was positioned close to the antenna, and its impact on the input impedance was investigated. The study showed that the real input impedance was close to zero for close separations between the cylinder and the dipole [2]. Since the radiation resistance is the main contributor to the real input impedance, it is expected to approach zero for narrow separations. Therefore, a similar approach was taken for long,

conducting cylinders next to the dipole on one and both sides. HFSS simulations were performed showing the effects of one and two conducting cylinders close to the dipole antenna and the same length as the dipole. These results are shown in Figures 3.12–3.13. The results indicate that any of the three situations (ground plane, one parallel cylinder or two parallel cylinders in close proximity) will cause serious degradation to the antenna return loss. Two parallel parasitic cylinders have an impact very similar to the ground plane. The large ground plane and two parasitic elements provide more area or angles around the dipole that produce images within the conductors. In other words, as more conductors surround the dipole, the boundary conditions are enforced around a larger surface surrounding the dipole.

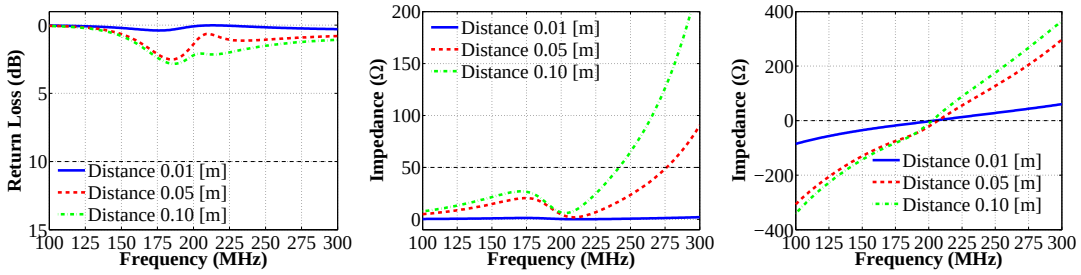

(a) Return Loss (b) Real Input Impedance (c) Imaginary Input Impedance

Figure 3.12: One Parallel, Parasitic Element in Close-Proximity to Dipole

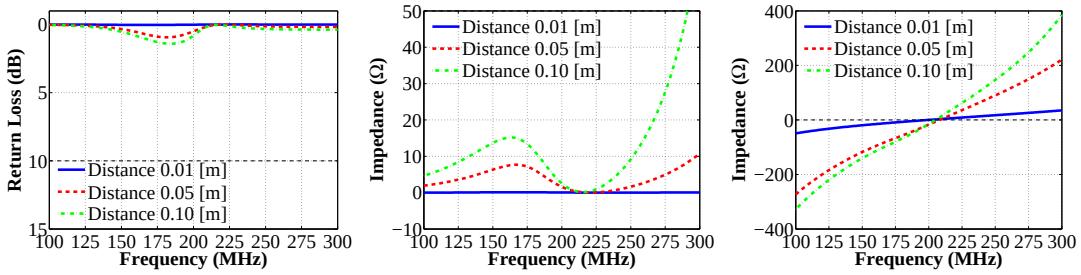

(a) Return Loss (b) Real Input Impedance (c) Imaginary Input Impedance

Figure 3.13: Two Parallel, Parasitic Elements in Close-Proximity to Dipole

The parasitic cylinders have a decreased affect on the radiation resistance as the separation increases. The study performed by Adams and Warren showed that as the distance increased, the radiation resistance increased until it began to oscillate around the impedance without a parasitic element present [2]. Their results compared the radiation resistance at resonance as a function of the separation between antennas. The same method for data analysis was performed for the HFSS simulations above comparing

one and two elements, and the author's figure is reproduced and compared with the HFSS simulation data in Figure 3.14. The HFSS simulation with one parasitic element agrees well with the results produced by Adams and Warren. The addition of the second parasitic element showed larger variation for input impedance values and larger oscillations around the dipole natural frequency, which is the dipole resonant frequency in free-space. Since there are two elements instead of one, the total distance between the dipole and both parasitics increased by a function of two times d. Two parasitic elements also increases the total conductor area surrounding the dipole, so the greater area permits a greater potential for canceling fields in comparison with one parasitic element. This causes the peak around 0.4λ to become much higher, which indicates the radiation resistance has a higher possible peak with more parasitic elements. The same trend occurs in terms of the imaginary input impedance in Figure 3.15.

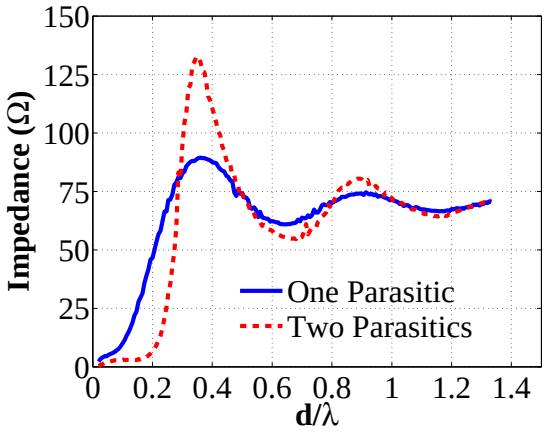

Figure 3.14: Dipole Plus Parasitic Elements

A similar investigation was taken place with the length of the parasitic element changing and the distance kept constant at 0.08 meter (0.053λ at 200 MHz). The parasitic element is located at the center of the dipole. The results for this simulation setup is shown in Figure 3.16. As the parasitic's length increases, the resonance shifts to higher frequencies. The current distribution is stronger at the center of the dipole due to the additional conductor. Currents capacitively couple from the dipole to the parasitic element, and then the dipole current distribution is stronger at the center. This is an opposite effect of top-hat loading, where the dipole resonant frequency is decreased due to parallel conductors at the ends of the antenna [20, 21, 37, 48, 67, 68]. The top-hat loading effect is discussed in more detail later in this section. The parasitic elements increase the distribution at the center causing the dipole to appear electrically

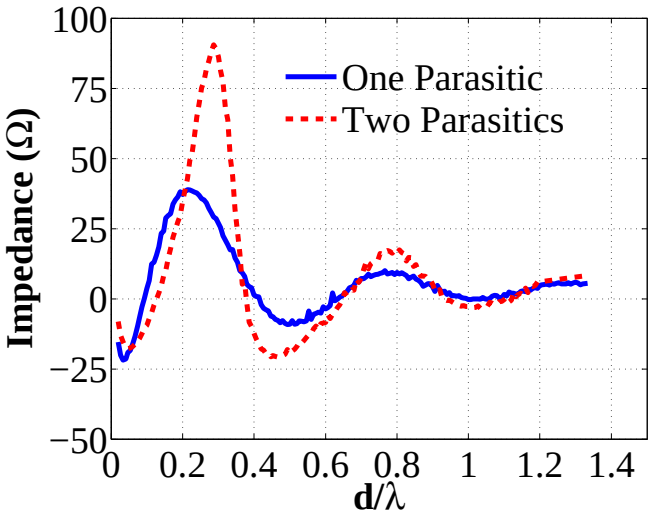

Figure 3.15: Parasitic Elements' Impact on the Imaginary Input Impedance

shorter. As the parasitic element becomes longer, more currents couple and the effect increases. As the resonant length increases, the return loss improves as well. However, the effect has a limit at which point, the resonant frequency decreases and the return loss decreases. At this point, the majority of the energy at the input port of the dipole becomes reflected. The presence of one and two parasitic elements experience the same trends, except two parasitic elements causes the trend to occur more greatly for shorter parasitic elements.

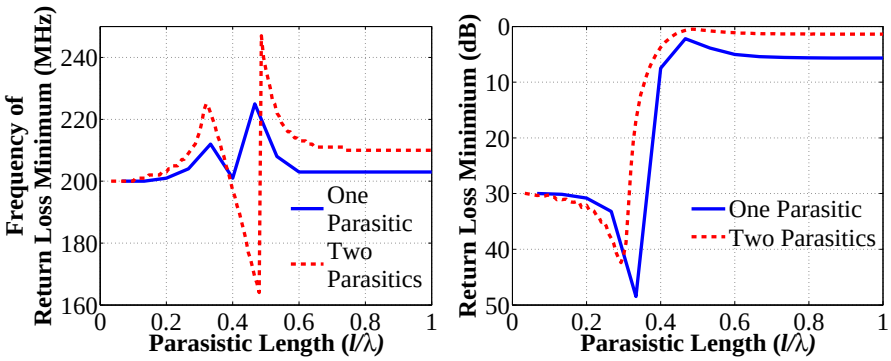

(a) Resonant Frequency (b) Return Loss at Resonance

Figure 3.16: Return Loss as a Function of the Parasitic Elements' Lengths

Although the boundary condition predicts the extinguishing of the source an infinitesimal distance and very close separations, the interaction between the conductor

and the antenna is more complex at larger separations. The antenna produces both magnetic and electric fields that induce currents on the conductor. The energy transfer is often expressed in terms of mutual impedance for a circuit explanation. The general mutual impedance equation (Equation 2.20) shows that the summation of currents along the source along with the electric field propagated from the source will determine the magnitude of the energy coupled onto the receiver. The most energy is coupled with a good radiator, but as a wire or current element becomes longer this contribution will become greater. As the length of the current becomes longer, Equation 2.20 indicates the coupling will increase. As explained in Section 2.2.1, the increased mutual coupling between two antennas (one may be parasitic) the larger the impact on the input impedance. As the current increases, the input impedance will decrease. Similarly, close proximity will indicate a larger mutual impedance, so it can be expected that the input impedance will decrease. This agrees with the simulation results presented above in Figures 3.11–3.14.

While these investigations showed general trends for antenna bandwidth performance with a conductor in close proximity, this analysis provides insight to the integration of the modified bow-tie antennas within a structure containing long conductors. The first conductors discussed are the gang channels, which are strips providing a strong connection for securing the skins to the fairing and allowing a washer and nut in to the bolt [75]. The gang channels were originally long metal strips extending the full length of the fairing and oriented parallel to the antennas. The investigation occurred for the outboard fairings as shown in Figure 3.17. The original length of the gang channels on the outboard arrays was the length of the fairing, which was 3,060.7 mm (120.5 in). The center-to-center spacing between antennas was 749.3 mm (0.49λ at 195 MHz). The separation between the antenna edge and the gang channel was 92 mm.

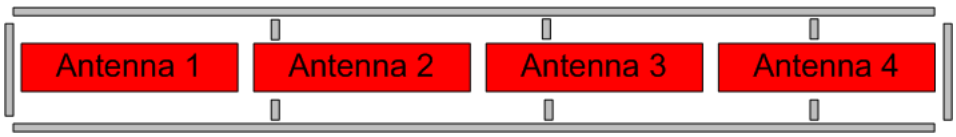

Figure 3.17: Original Gang Channel Configuration for Outboard Fairings

The simulation results for the outboard antennas with this configuration is shown in Figure 3.18. The operational bandwidth was severely deteriorated with these long gang channels. The case for the close doubler and long parasitic elements parallel the antenna appear to predict this effect.

Similarly, the original configuration for the doublers were continuous without any

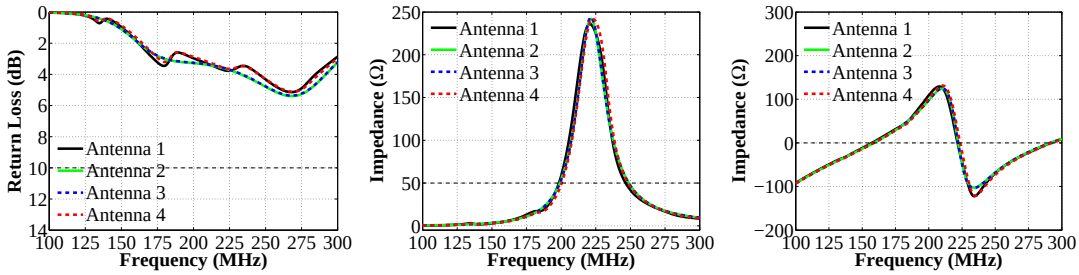

(a) Return Loss (b) Real Input Impedance (c) Imaginary Input Impedance

Figure 3.18: Simulation with Original Gang Channel Configuration for Outboard Fairings

gaps as shown in Figure 3.19. The simulation results for this configuration is shown in Figure 3.20, which is very similar to the long gang channels. One major difference between the gang channels and the doublers is the separation between the doublers and antennas, so the doublers are expected to have a greater impact due to their closer proximity. Both the real and the imaginary components of the input impedance vary to much larger extremes, which will not permit the design for large operational bandwidths. The doublers shifted the resonant frequency higher as shown through the imaginary input impedance.

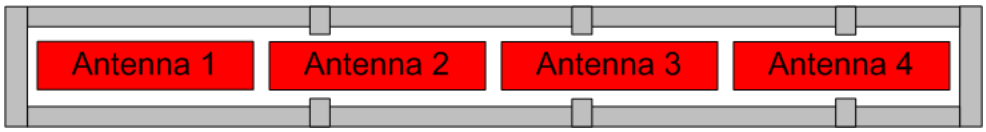

Figure 3.19: Original Doubler Configuration for Outboard Fairings

A lower skin was fabricated with long doublers without the gaps between each doubler. This had the effect of decreasing the bandwidth and increasing the resonant frequency. This is shown in Figure 3.21 compared with the simulations for the long doublers and long gang channels. The simulations for both the doublers and the gang channels are very similar in their performance. The measured performance did better than expected, but the 10 dB bandwidth barely existed. The antenna performance without any loading had a return loss slightly greater than 10 dB around 250 MHz. As the frequency increases, the electrical distance compared to a wavelength is greater, so it can be expected that high frequencies will be less affected by the presence of the conductors as discussed previously. Below 240 MHz, the measurement and simulation agree well.

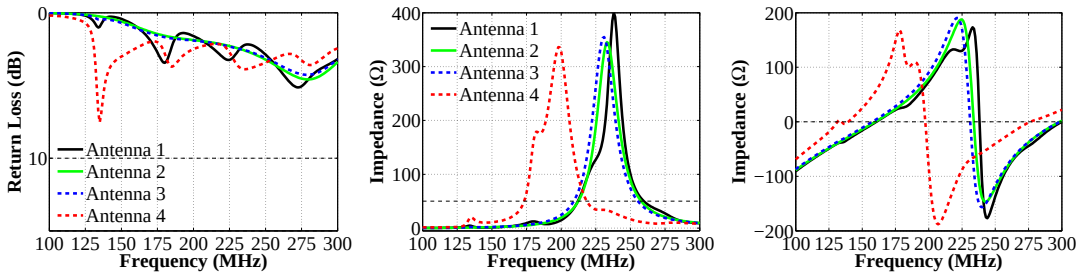

(a) Return Loss (b) Real Input Impedance (c) Imaginary Input Impedance

Figure 3.20: Simulation with the Original Doubler Configuration for the Outboard Fairings

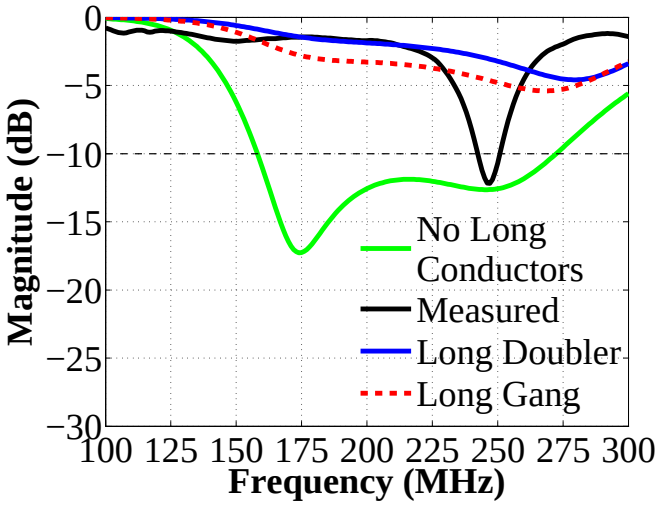

Figure 3.21: Measured Antenna on Skin with Long Doublers Compared with Simulations

After evaluating these long conductors' impact on the antenna performance, the gang channels and doublers were split into shorter segments. The gang channel configuration is shown in Figure 3.22. The gang channels are symmetric, so only half the inboard array is shown in the figure. The gang channel lengths are given in Table 3.1 and their widths are 13 mm. The gaps between the two G4 gang channels is 54 mm. The distance from the antennas to the gang channels on the inboard section is 71 mm.

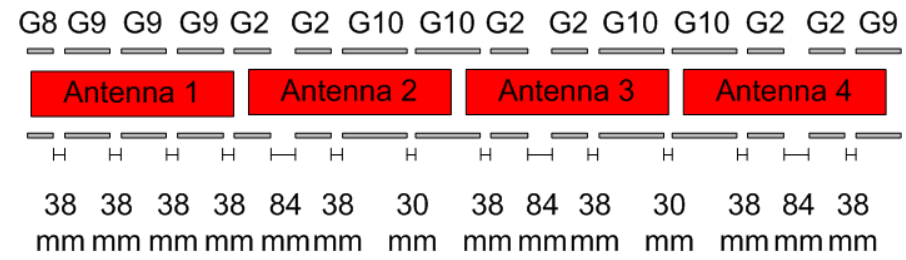

(a) Outboard

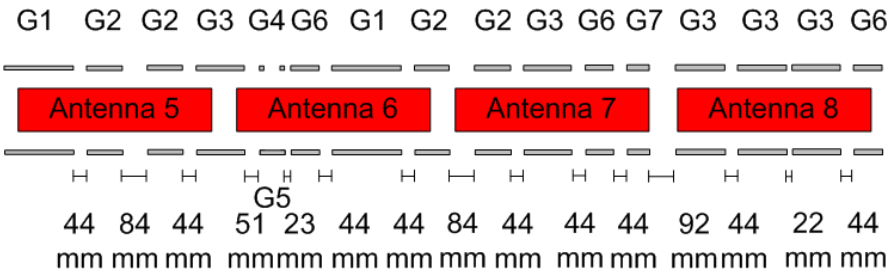

(b) Inboard

Figure 3.22: Final Gang Channel Configuration

Table 3.1: Gang Channel Dimensions

Gang Channel Number	Length (mm)
G1	235
G2	121
G3	165
G4	13
G5	83
G6	95
G7	76
G8	89
G9	152
G10	216

Since the skins were fabricated with the doublers sandwiched between fiberglass

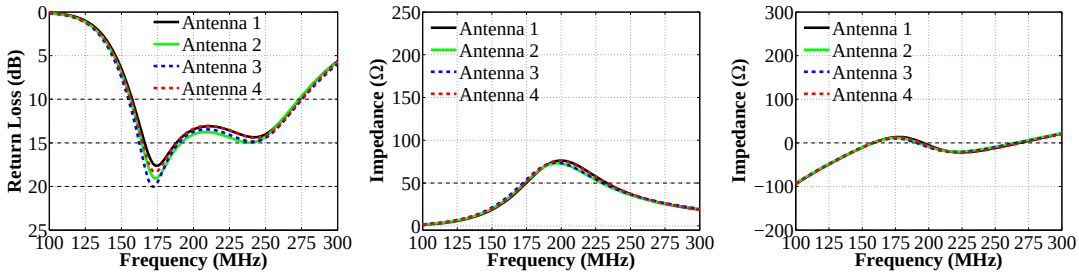

(a) Return Loss (b) Real Input Impedance (c) Imaginary Input Impedance

Figure 3.23: Simulation with Segmented Gang Channel Configuration for Outboard Fairings

layers, a post-fabrication solution involved slotting the doublers through the skin. The segmented doubler configuration is shown in Figure 3.25 with dimensions in Table 3.2. The lengths are defined in the same direction as their names. The gaps between each doubler for the first revision is 21.6 mm, and the separation between each doubler and antenna is 31.8 mm, except for doubler D3 that has a separation 8.3 mm. A side section view of the doublers inside the skins is shown in Figure 3.9. The distance from antenna 8 to the end-doublers (D13 and D9) was 2.5 mm, which is the same separation for antenna 7 to D8. The layer of Rohacell foam (Rohacell 71 IG) was added to decrease any dielectric effects through the glass.

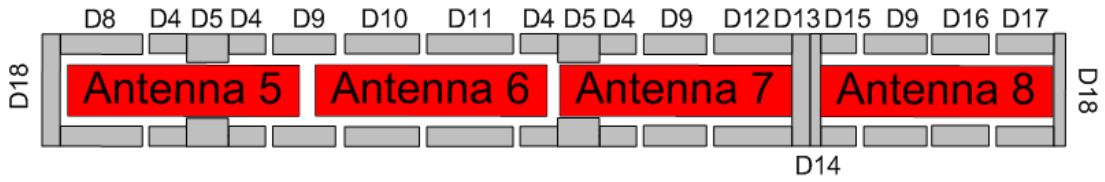

Figure 3.24: Revision 1 Doubler Dimensions and Gaps

The measured performance for the doublers are evaluated comparing symmetric antennas in Figure 3.27-3.29. The doubler design was symmetric for the inboard array, and the two outboard arrays were identical. One of the main contributions to antenna variations was attributed to the baluns, and the variations between baluns were more thoroughly investigated for the second revision in Section 4.2. The return loss plots indicate comparable performance for most of the symmetric antennas within this configuration. Similarly, the input impedance plots show that the real input impedance was similar as well. One of the largest variations was between antennas 2 and 14, where the real input impedance for antenna 14 is lower throughout the bandwidth than antenna

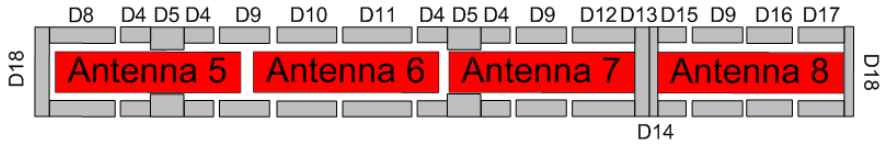

(a) Inboard

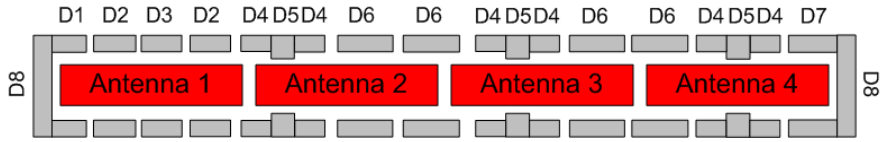

(b) Outboard

Figure 3.25: Rev. 1 Slotted Doubler Configuration for Outboard Fairings

Table 3.2: Rev. 1 Doubler Dimensions

Doubler Number	Length (mm)	Width (mm)
D1	88	59
D2	156	59
D3	155	59
D4	111	59
D5	127	82
D6	220	59
D7	333	54
D8	245	59
D9	188	59
D10	224	59
D11	233	59
D12	258	59
D13	56	333
D14	32	333
D15	106	59
D16	170	59
D17	171	59
D18	333	36

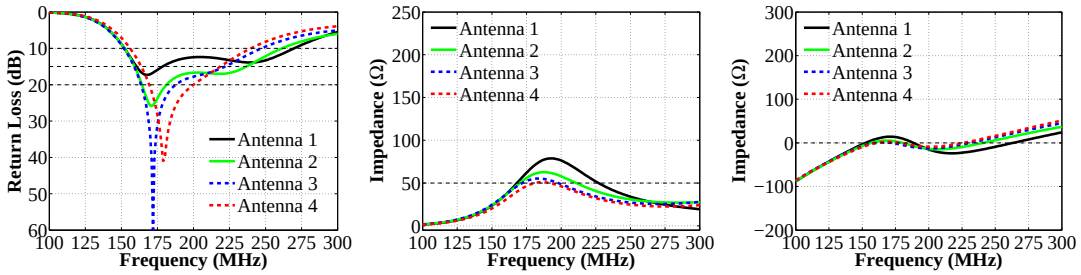

(a) Return Loss (b) Real Input Impedance (c) Imaginary Input Impedance

Figure 3.26: Simulation with Slotted Doubler Configuration for Outboard Fairings

2. As discussed above, this effect can be caused by the presence of more conductors around the antenna.

The worst performance was antenna 8, which had a return loss barely more than 10 dB throughout the bandwidth. The doubler configuration around this antenna featured doublers along the width at the ends of the antennas, which is similar to a top-hat loaded or capacitor plate antenna [8, 72]. The addition of disks or long wires from the top of a monopole has been shown to lower the resonant frequency [20, 21, 37, 48, 67, 68]. The current increases at the antenna ends due to these elements causing the distribution to transition from triangular to uniform [8, 21]. This decreases the effective height of the antenna [8, 21, 37]. This effect in terms of the imaginary input impedance is shown in Figure 3.30, and this result is increased with a "top-hat" as discussed in terms of increasing the length of support wires by Gangi et. al. [21]. This adds capacitance to store more charge at the ends of the antenna and forces the distribution to be more uniform [72]. When the current is more uniform, the antenna better utilizes its area. However, this is still undesirable since the current for a dipole is sinusoidal. The radiation resistance of a top-hat loaded antenna is less than the radiation resistance for a dipole having the same resonance but without the end-caps [37]. The concept of top-hat loading or top-loaded antennas has been used where practical and to reduce the lengths of antennas. Monopoles used for Very Low Frequencies (VLF) and Low Frequencies (LF) were electrically short or less than $\lambda/8$, but the addition of support wires or guy wires caused the top-hat loading [21]. As the length of these wires increased, the antenna inductance increased and the resonant frequencies decreased [21]. While a monopole or dipole has currents flow through the length, the currents flowing through the horizontal structure increases the effect.

The concept of end-loading has been intentionally used to decrease the length of antennas and achieve larger bandwidths for planar geometries [71]. The bow-tie designed

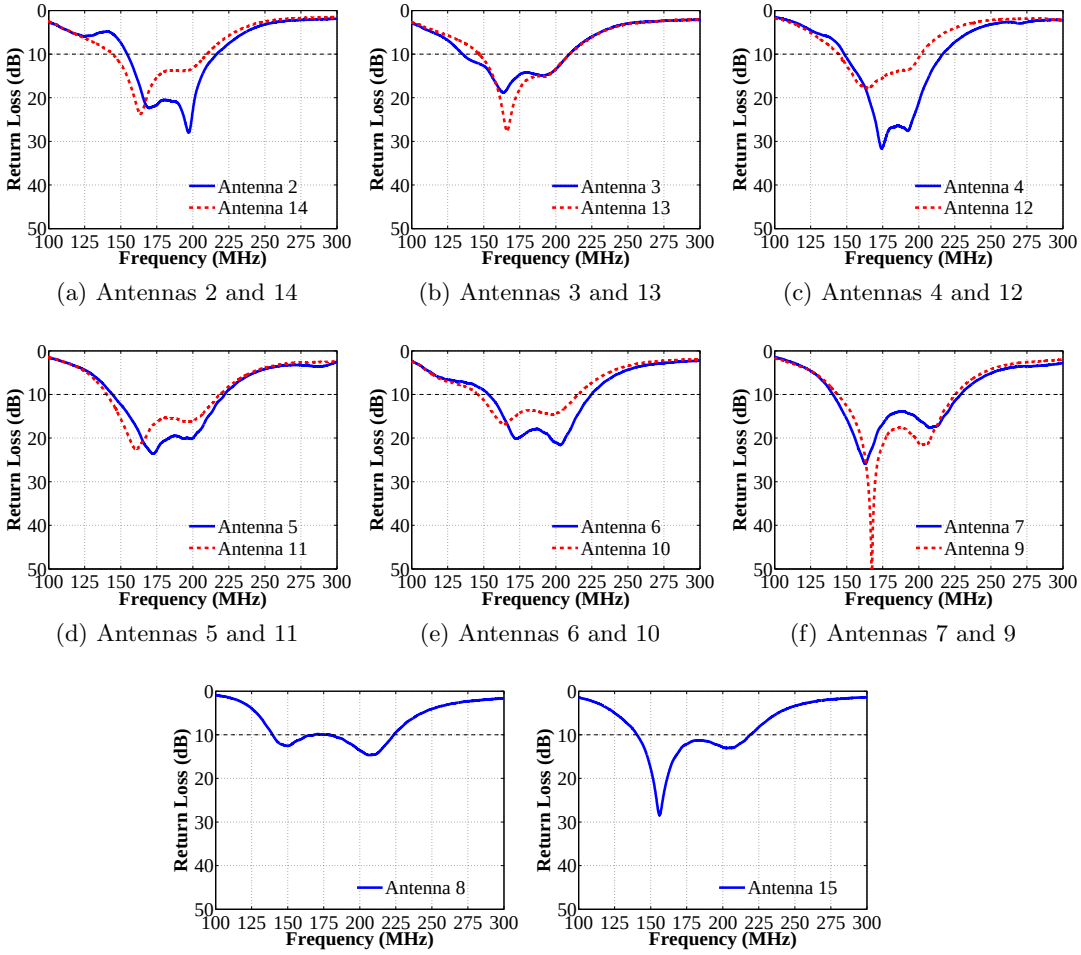

(a) Antennas 2 and 14 (b) Antennas 3 and 13 (c) Antennas 4 and 12

(d) Antennas 5 and 11 (e) Antennas 6 and 10 (f) Antennas 7 and 9

(g) Antenna 8 (h) Antenna 15

Figure 3.27: Skin Antenna Measured Return Loss Comparisons for Symmetric Antennas

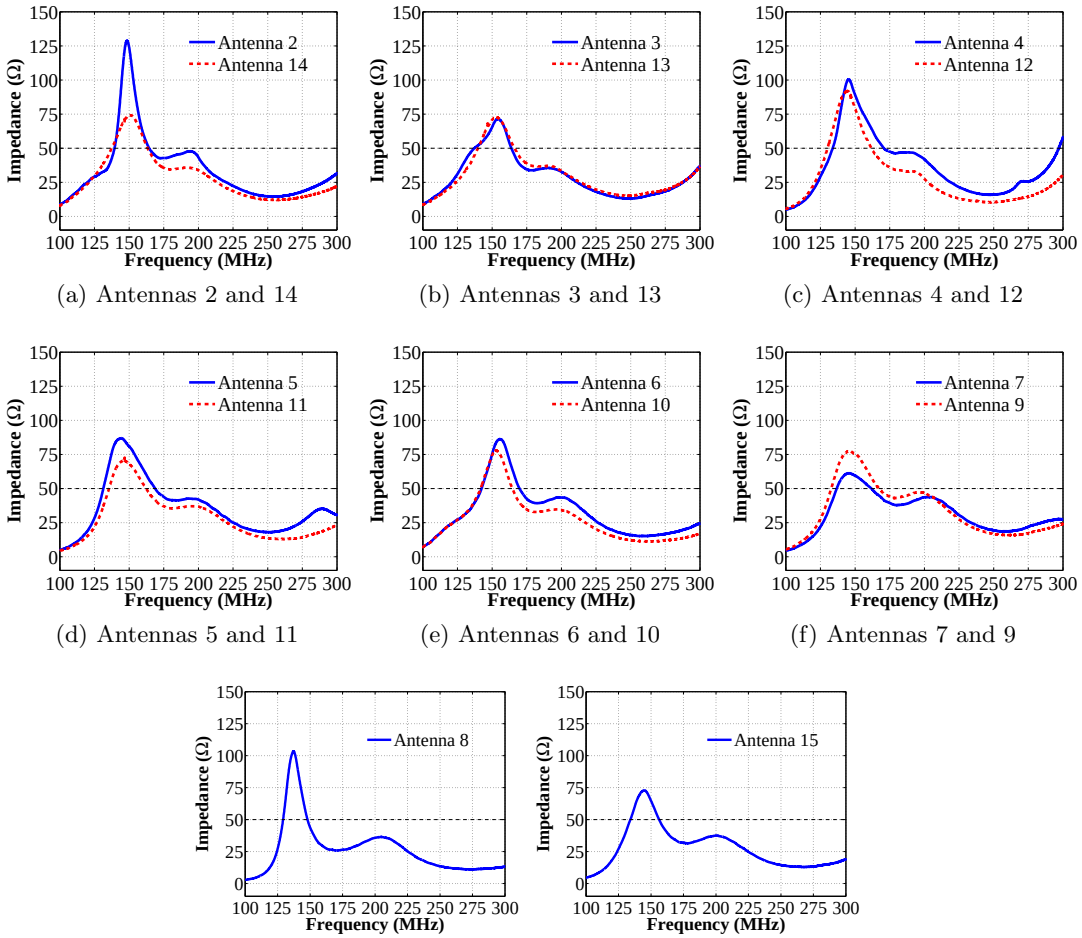

(a) Antennas 2 and 14 (b) Antennas 3 and 13 (c) Antennas 4 and 12

(d) Antennas 5 and 11 (e) Antennas 6 and 10 (f) Antennas 7 and 9

(g) Antenna 8 (h) Antenna 15

Figure 3.28: Skin Antenna Measured Real Input Impedance Comparisons for Symmetric Antennas

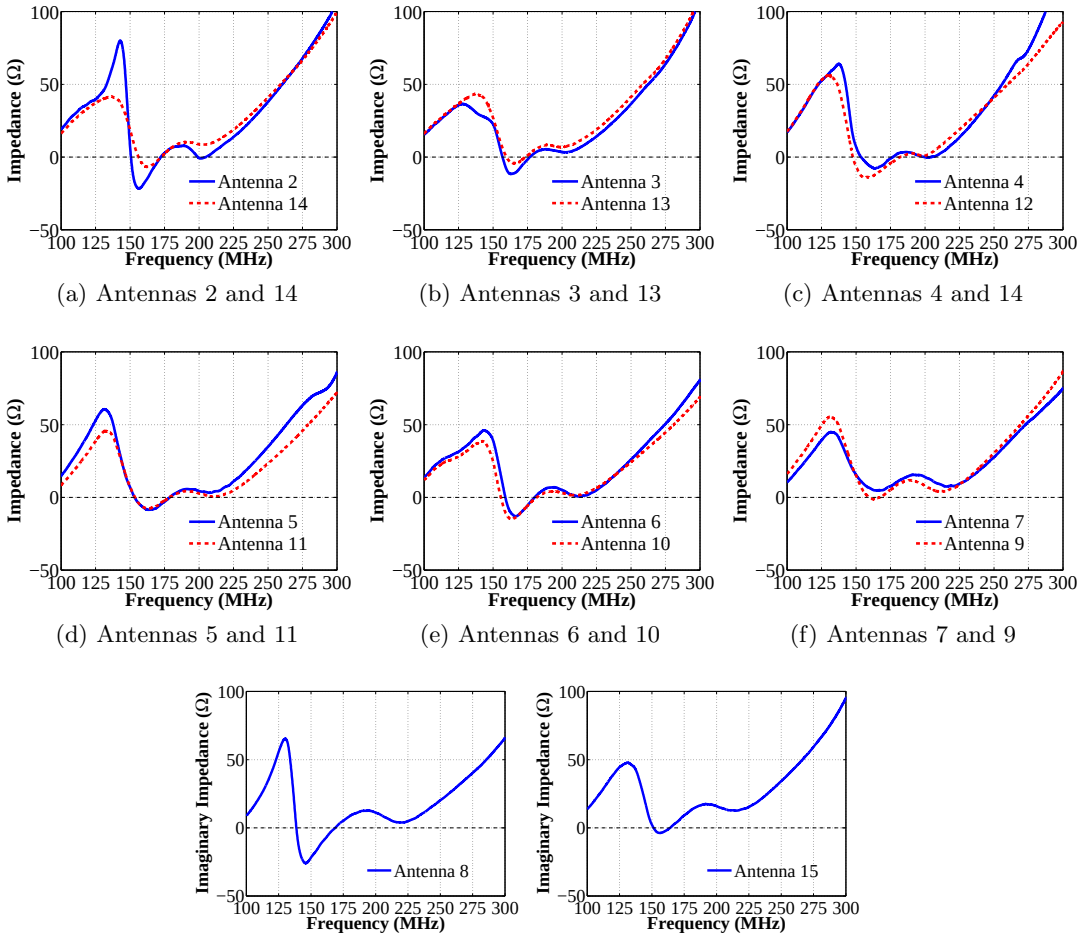

(a) Antennas 2 and 14 (b) Antennas 3 and 13 (c) Antennas 4 and 14

(d) Antennas 5 and 11 (e) Antennas 6 and 10 (f) Antennas 7 and 9

(g) Antenna 8 (h) Antenna 15

Figure 3.29: Skin Antenna Measured Imaginary Input Impedance Comparisons for Symmetric Antennas

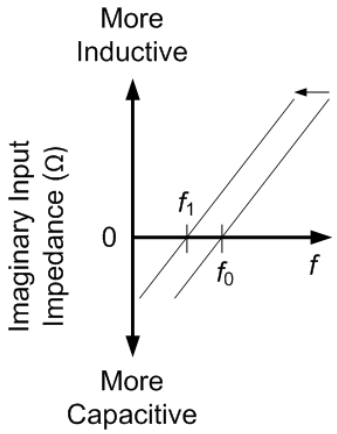

Figure 3.30: Resonant Shift for a Top-Hat Loaded Antenna

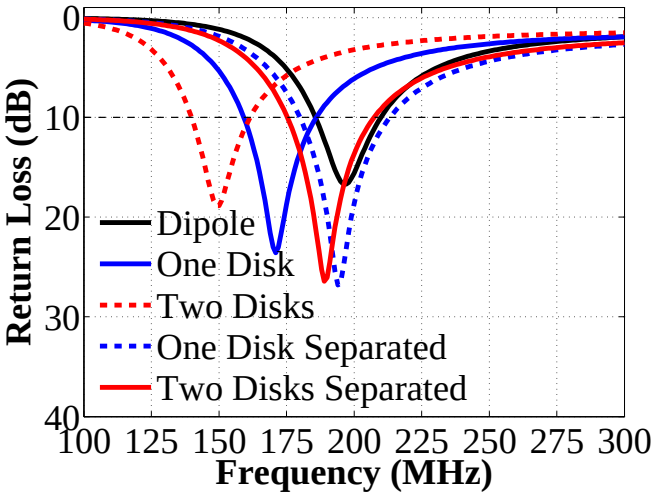

Figure 3.31: Top-Hat Loaded Dipole Comparing One and Two Disks Attached and Detached

by Werner and Spence has a planar rectangle similar to the end doublers in the aerospace fairing and is shown in Figure 2.6. End-loading can be anticipated for antennas close to this element such as antenna 8. End-loading is well documented when the extending geometry or "top-hat" is conductively attached to the antenna, but the configuration explored here has detached parasitic "top-hats". An investigation into the effects of end-loading with detached parasites was performed with a dipole. This dipole had a disk attached and detached to one side and two sides. These two situations are compared in Figure 3.31, and the dipole does not have any loading.

The end-loading shows both a decreased resonant frequency, and the resonance for antenna 8 occurs about 15 MHz below the other resonances. Antenna 8 has a resonance at 138 MHz while the resonance for the other antennas ranges from 148-158 MHz with most around 155 MHz. The length of the end doublers is 0.22λ at 195 MHz, so this corresponds to a large shift for two attached doublers that do not have a strong return loss at this resonant frequency. The shift experience by the attached disks was around 140 MHz, which is very large and would be expected to have a poor return loss.

On the other hand, the doubler configuration around antenna 8 is a planar set-up with detached doublers producing a top-loaded effect. The frequency shift is significant but not as great as the shifts for the dipole with two disks (attached or detached) at a radius of 0.22λ. The frequency shift for one disk separated by 5 mm is about 20 MHz for a radius of 0.22λ, and the same situation for two detached disks is about 40 MHz. While the performance is not exactly the same as the dipole with disks, the antenna 8 still experienced a significant resonant shift that was not present for the other antennas.

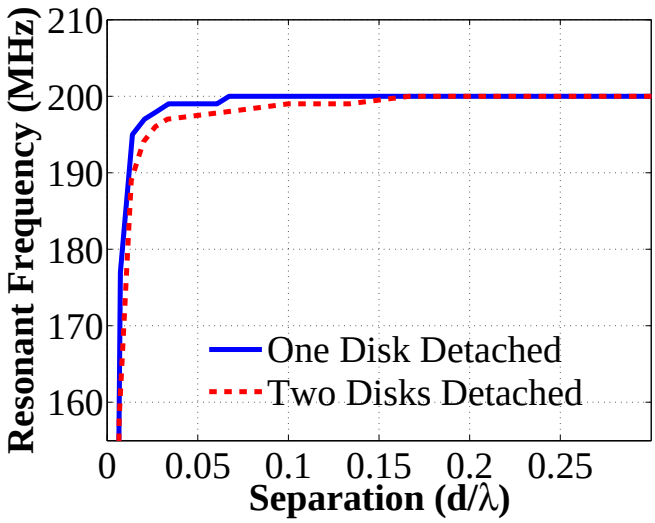

Figure 3.32: Top-Hat Loaded Dipole Comparing Separation of One and Two Detached Disks (Radius 100 [mm])

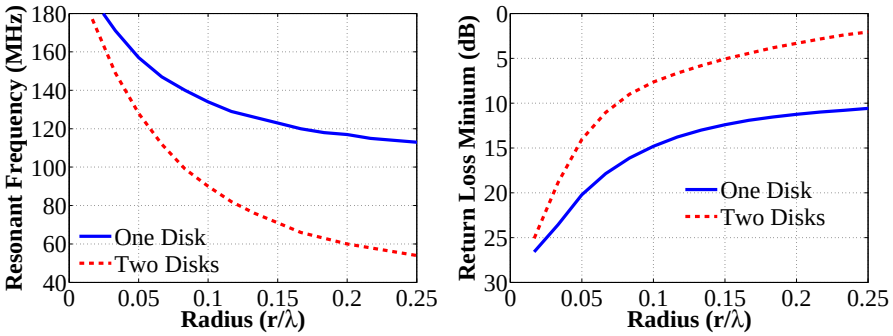

(a) Resonant Frequency

(b) Return Loss Magnitude at Resonant Frequency

Figure 3.33: Top-Hat Loaded Dipole Comparing Varying Radius of One and Two Attached Disks

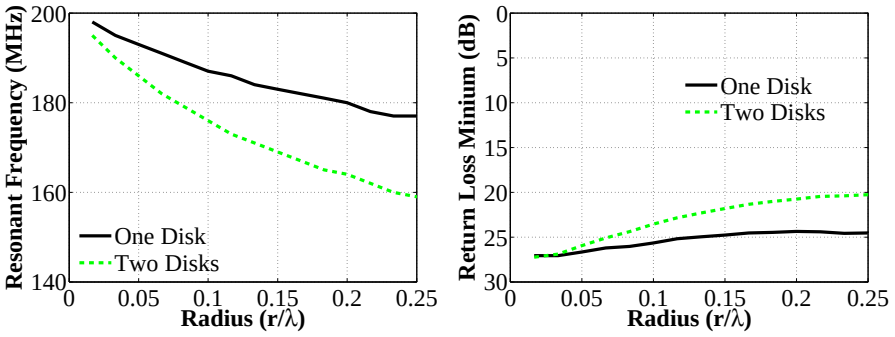

(a) Resonant Frequency

(b) Return Loss Magnitude at Resonant Frequency

Figure 3.34: Top-Hat Loaded Dipole Comparing Varying Radius of One and Two Detached Disks

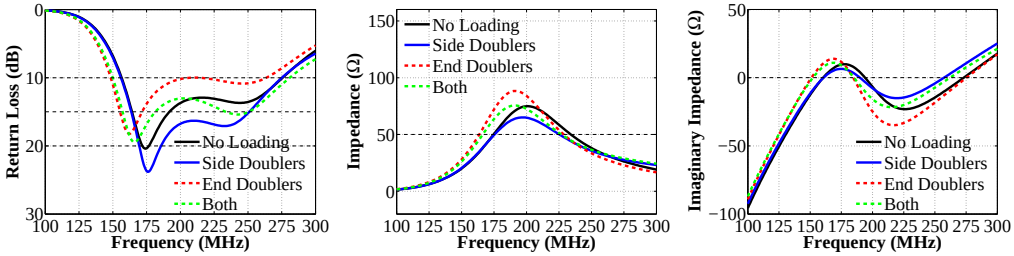

(a) Return Loss

(b) Real Input Impedance

(c) Imaginary Input Impedance

Figure 3.35: Rev. 1 Antenna 8: Separation of Side and End Doublers

This antenna not only was planar compared to the three-dimensional dipole, but there were doublers alongside the antenna as well. Simulations were performed in order to separate the influence of the end-doublers and side doublers for this antenna, and the results are shown in Figure 3.35. These simulations excluded any effects caused by the S2-glass.

3.3.2 Cables

Similar to the long gang channel and doublers, the antenna feed cables are long metallic cylinders that can also have an effect on antenna bandwidth. The antenna feed cables were positioned 90° to the antenna, and then run parallel to the antennas as shown in Figure 3.36. The feed cables are 1/4" Heliax Superflexible Foam coaxial cables (FSJ1-50A). Each feed cable is routed from the bulkhead on the P-3 skin to the appropriate antenna. Therefore, each cable is of different length. In the first revision, there were also accelerometer cables positioned next to several antennas. The antenna skins have

been removed from Figure 3.36 in order to view inside the fairing.

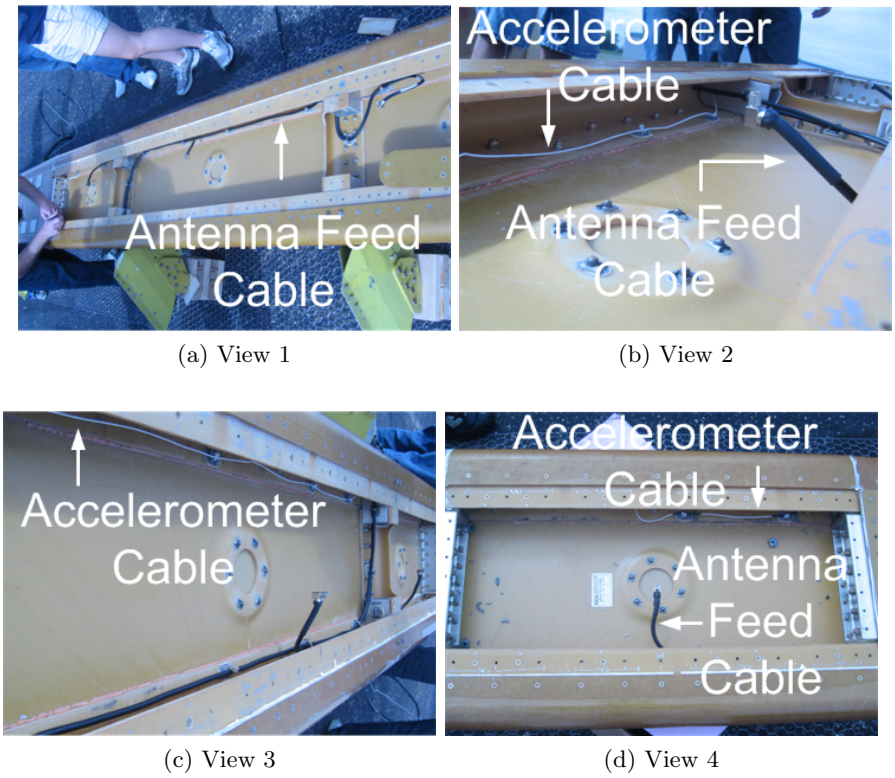

(a) View 1 (b) View 2

(c) View 3 (d) View 4

Figure 3.36: Inside of the Rev. 1 Inboard Array Fairing

The following figure shows a controlled test of the cables' effects on the antenna performance. The accelerometer cable was replaced with a RG-58, a slightly thicker cable. The controlled cable experiment shown in Figure 3.37. A solid ground plane is used under part of the array but was not larger enough, so a mesh ground plane was added. The maximum dimension of the hexagons in this ground plane was 35 mm (0.028λ at 240 MHz). This separation is electrically small and much smaller than wavelength, so can be approximated as a conducting sheet [24].

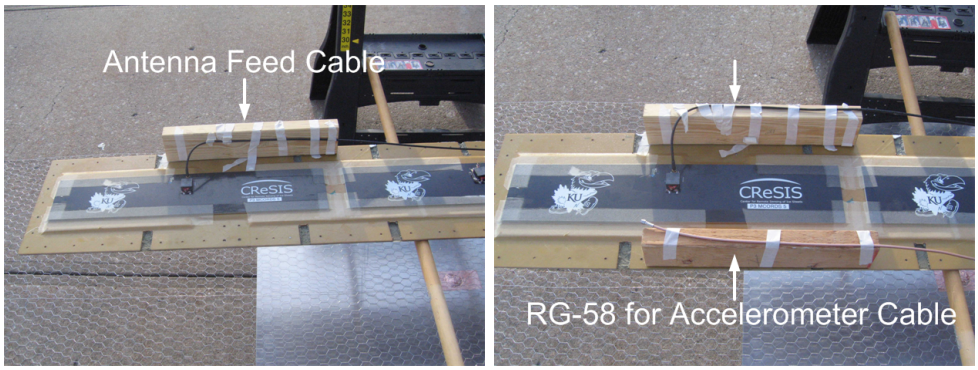

(a) Only the feed cable (b) Both the feed cable and accelerometer

Figure 3.37: Test Setup Comparing the Cable's Effects Next to Antenna 5

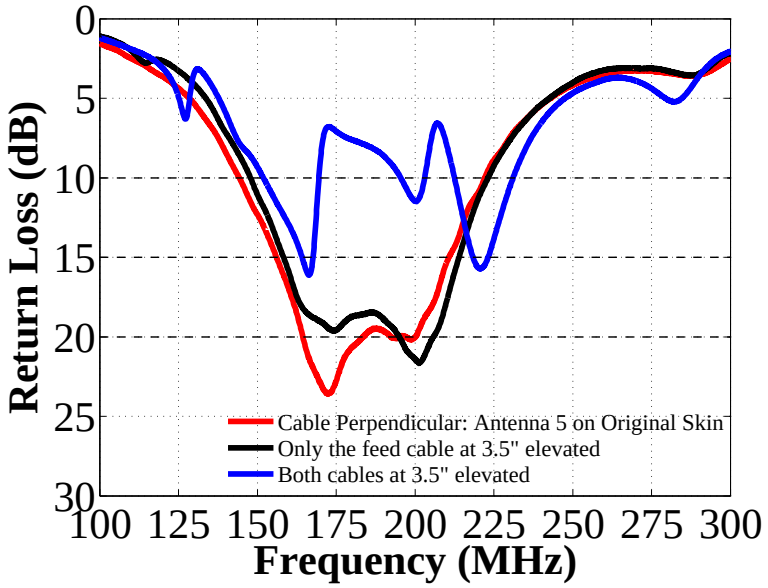

Figure 3.38: Antenna Element 5: Measurements Comparing Cable Effects on Skin

3.3.3 Miscellaneous Metallic Components' Effects

As shown in Figure 3.8, the fairing contains other metallic objects for structural support such as the rib inserts, feed and accelerometer cables and the pylons. The integration with the full fairing also contains glass completely surrounding the antenna with a space between the antenna and glass. Measurements were performed on the inboard array inside the fairing on a ground plane. This measurement setup is shown in Figure 3.39. These measurements were performed at the Lawrence airport. The change in performance including the cables, pylons and rib inserts from the antennas on the skins is shown in Figure 3.40.

(a) View 1 (b) View 2

Figure 3.39: Measurements Setup for Fairing on Ground Plane

The fairing measurements were only done for the inboard fairing, but every antenna was measured during a the test flight and installed on the aircraft. These results are presented in Figure 3.42. These results were time-gated for the long cables in between the network analyzer and the antennas. The full description of the time-gating performed is described in Appendix C. Also, these return losses have the cable loss removed according to a two way propagation for the cable distances provided in Appendix B.

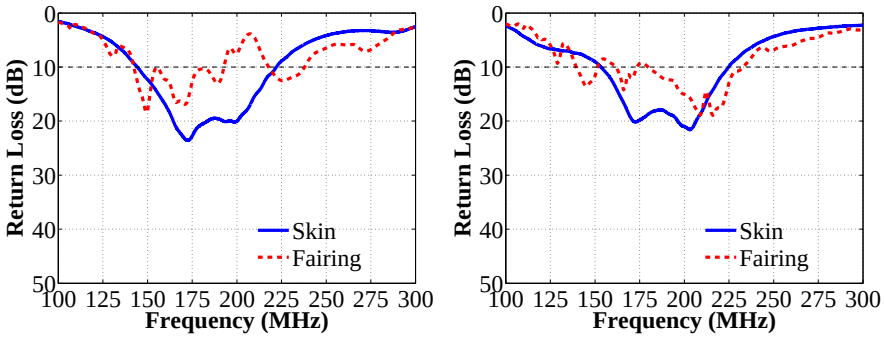

(a) Antennas 5

(b) Antennas 6

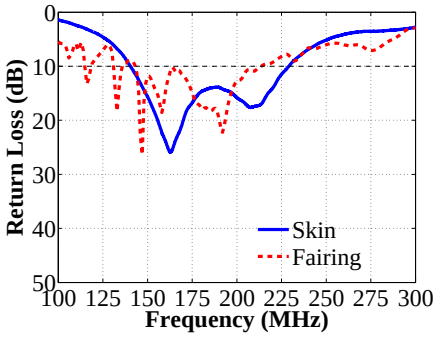

(c) Antennas 7

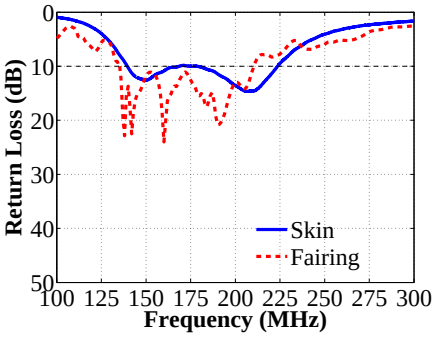

(d) Antenna 8

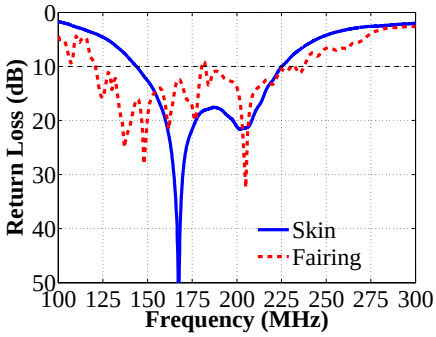

(e) Antenna 9

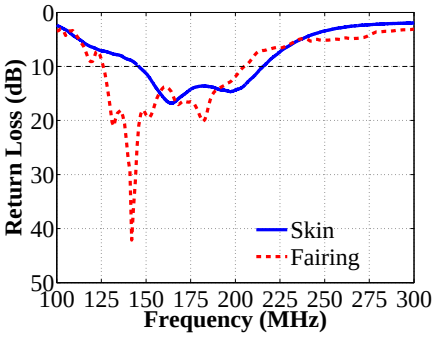

(f) Antenna 10

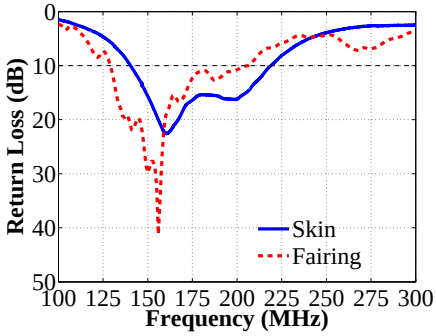

(g) Antenna 11

Figure 3.40: Rev. 1 Inboard Skin and Fairing Return Loss Measurements Comparison

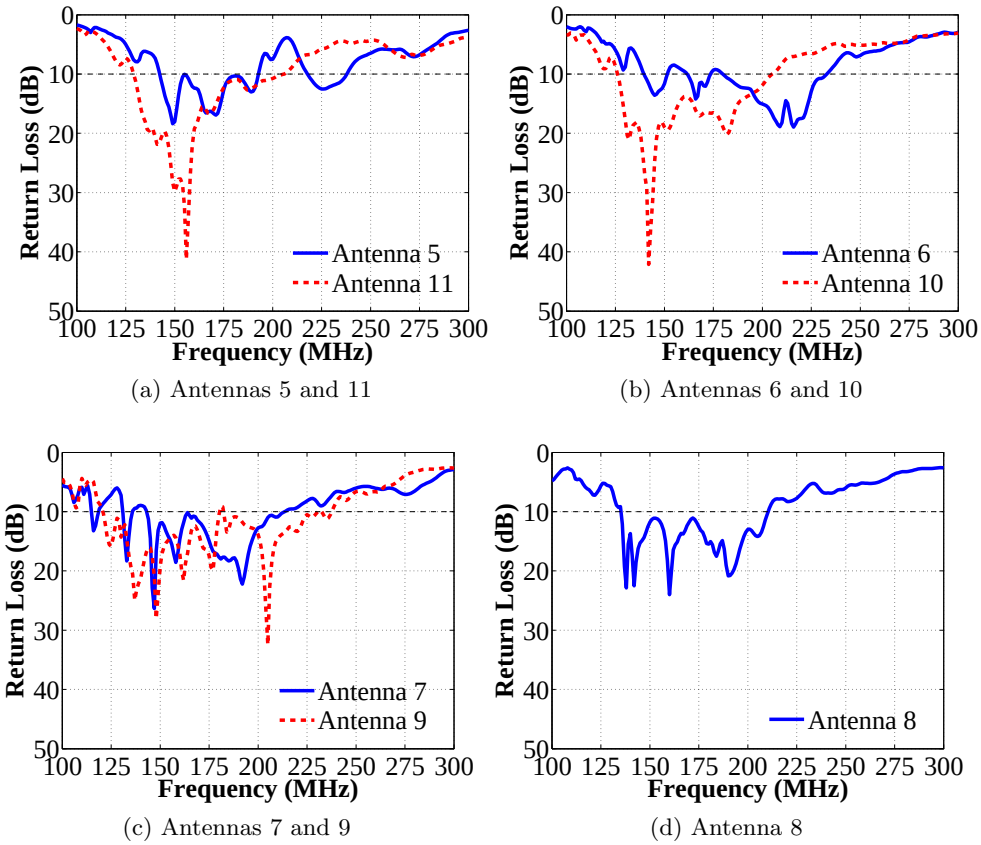

(a) Antennas 5 and 11

(b) Antennas 6 and 10

(c) Antennas 7 and 9

(d) Antenna 8

Figure 3.41: Rev. 1 Inboard Fairing Return Loss Measurements Comparing of Symmetric Antennas

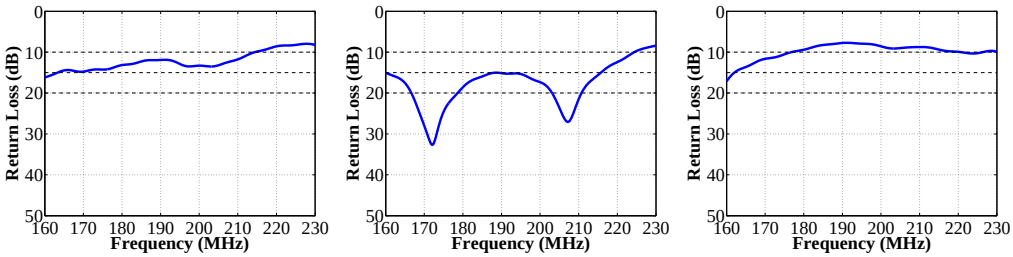

(a) Antenna 1 (b) Antenna 2 (c) Antenna 3

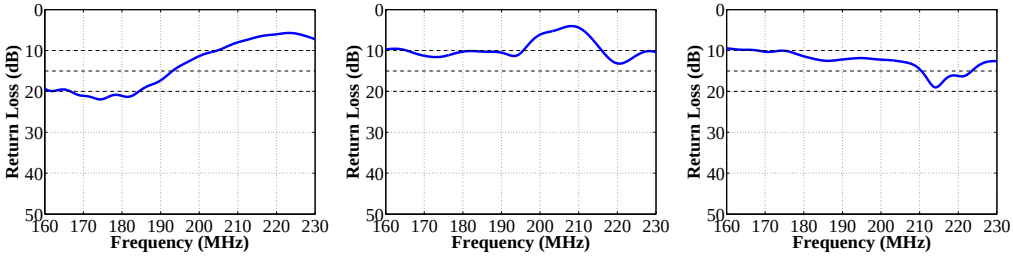

(d) Antenna 4 (e) Antenna 5 (f) Antenna 6

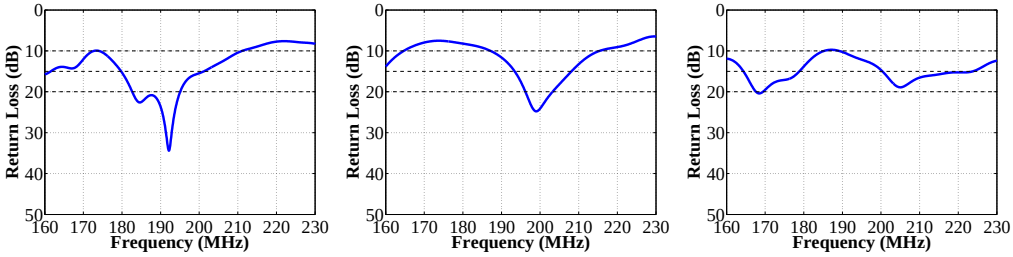

(g) Antenna 7 (h) Antenna 8 (i) Antenna 9

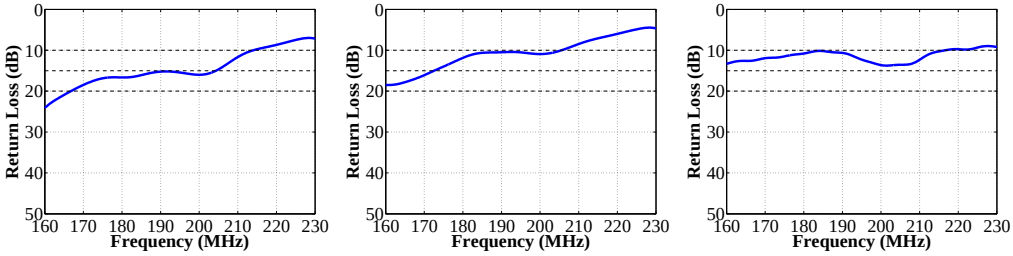

(j) Antenna 10 (k) Antenna 11 (l) Antenna 12

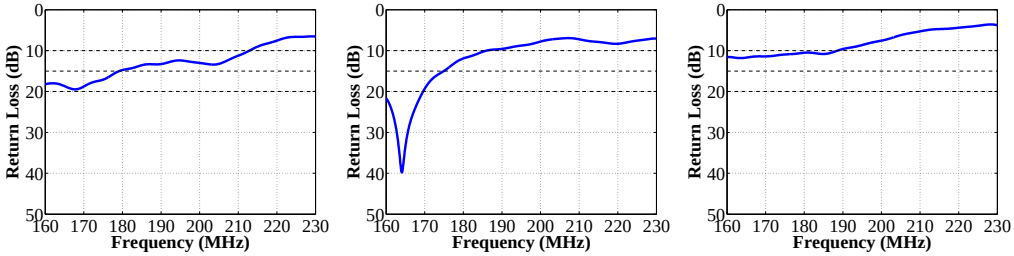

(m) Antenna 13 (n) Antenna 14 (o) Antenna 15

Figure 3.42: Installed Return Loss Measurements for Rev. 1

3.4 Mutual Coupling

The mutual coupling observed in the first revision of the antennas and fairings is shown in Figure 3.43. This represents a high level of mutual coupling that peaks at the lower frequencies for both these elements in terms of 10 dB return loss. The maximum coupling of 7.2 dB occurs around 160 MHz. The simulated coupling follows the same trend beyond 200 MHz for both the real and imaginary components of the mutual impedance, but there is a deep null in the real part of the mutual impedance at 150 MHz that is not indicated through simulation. Also, there is a large discontinuity in the measured imaginary component around 150 MHz from -75 Ω to 70 Ω. As shown by [72], the real and imaginary components approach zero as the spacing increases. The coupling demonstrated between these two elements is capacitive for low frequencies but abruptly becomes more inductive. The high level of mutual coupling provides motivation for improvement in revision 2.

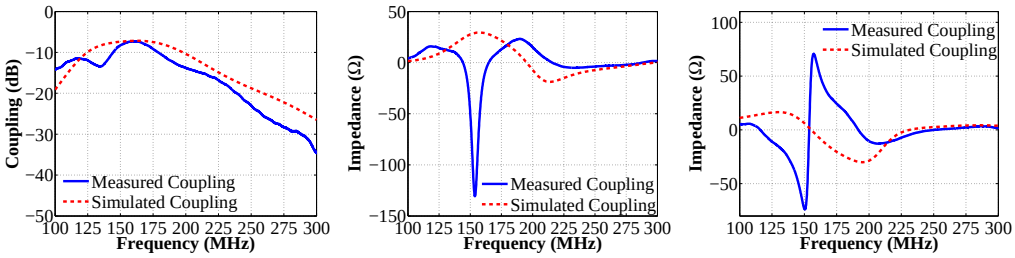

(a) S_{56} (b) Real Z_{56} (c) Imaginary Z_{56}

Figure 3.43: Mutual Coupling of Rev. 1 Antennas 5 and 6 on Skins

Chapter 4

Array Design Revision 2

Revision one of the fairing was deployed in Greenland during the spring of 2010. The fully installed antenna array showed room for improvements for future missions. In revision one, the resonant frequency for most antennas in revision one was shifted below 195 MHz, and the bandwidth lower and upper frequencies were shifted lower as well. Increasing the bandwidth with the center frequency around 195 MHz and increasing the return loss throughout the bandwidth was the primary goal for the second revision. The mutual coupling between elements was also strong, so decreasing this was also desirable. The second revision of the array was deployed in fully installed on February 17, 2011 and deployed in Greenland March 15th–May 15th, 2011.

4.1 Antenna Changes

The revision one antenna array performance needed several improvements. The approach was to more extensively anticipate and minimize the effects of the surrounding aerospace structure. The aerospace structure consisted of conductive and dielectric materials that affected the antenna. These effects were investigated, compensated and mitigated for in revision two to improve the antenna bandwidth.

4.1.1 Dielectric Loading

The results of a simulation including the glass addition required for the aerospace structure for the input impedance is shown in Figure 4.1. There was a shift lowering the resonant frequency of the antenna, so it was logical to shorten the antenna. The magnitude of the shift was 3 MHz on the lower side of the bandwidth and 12 MHz on the upper side of the bandwidth. The antenna length was adjusted. After running several iterations, it was found that for about every 1 cm decrease in antenna length,

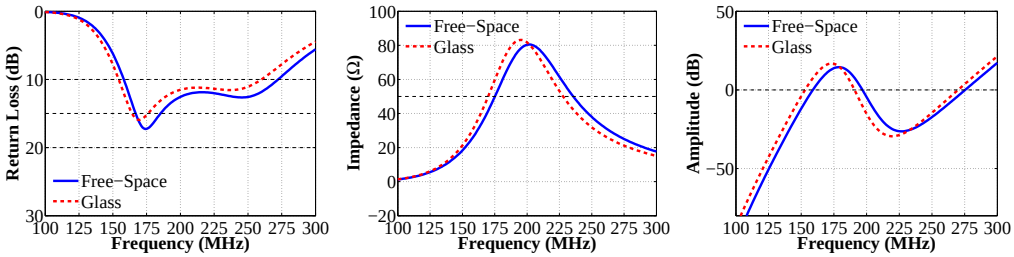

(a) Return Loss (b) Real Input Impedance (c) Imaginary Input Impedance

Figure 4.1: Free-Space and Only Glass Simulation Results Comparing the Rev. 1 Antenna

the lowest 10 dB bandwidth increased by 2 MHz. Therefore, the antenna length was shortened from 69 cm to 68 cm.

The reduction in antenna length with dielectric loading has been studied in many cases in order to construct antennas with reduced sizes [10, 12, 29, 40, 59, 70]. This size reduction is considered through the propagation velocity, phase constant and wavelength comparison in free-space and a dielectric. Each of these properties are dependent on the dielectric constant as shown in Equations 4.1, 4.2 and 4.4. First, the propagation velocity in free-space is given by Equation 4.1, where μ is the permeability and ϵ is the permittivity and has units of meters/seconds [58]. As the dielectric constant increases, the velocity of propagation decreases and is independent of frequency. However, the phase constant and wavelength are dependent on frequency. The phase constant provides the change in phase per unit length for each wave component and is given in Equation 4.2 [58]. The phase constant has units of meters^{-1}. At a particular frequency, the phase constant is referred to as the wave number and describes the propagation of the plane wave in terms of phase and attenuation as further shown in Equation 4.3, where α is the attenuation constant and β is the phase constant [58]. Therefore, the wave number describes the attenuation and phase of a plane wave within various materials. Finally, the wavelength is defined as the distance the wave propagates in one period and causes the phase factor to change by 2π. This is given in Equation 4.4 [58]. This shows that as the dielectric constant increases, the wavelength decreases.

$$v = \frac{1}{\sqrt{\mu\epsilon}} \tag{4.1}$$

$$k = \frac{\omega}{v} = \omega\sqrt{\mu\epsilon} \tag{4.2}$$

$$jk = \alpha + j\beta \tag{4.3}$$

$$\lambda = \frac{2\pi}{k} = \frac{2\pi}{\omega\sqrt{\mu\epsilon}} = \frac{v}{f} \tag{4.4}$$

In James et. al. the antenna dimensions are scaled down by a factor of $e_r^{0.5}$ from the free-space antenna length for when the antenna is enclosed within a dielectric medium, and this is shown in Equation 4.4 [29]. The bow-tie investigated in this problem operates at 195 MHz. In free-space, this wavelength is about 1.54 meters. Completely enclosed in S2-glass ($e_r = 5.2$), the wavelength is about 0.67 meters. This means that the antenna has a shorter electrical dimension, and the current distribution experiences a half-wave distribution at a lower frequency. Longer wavelengths in free-space have an effectively shorter wavelength in the dielectric medium, so a current will need a shorter dipole to produce a half-wave pattern. However, the antenna is not completely enclosed in S-2 glass, but rather the antenna has a thin layer of glass around the edges structurally connecting the antenna to the solid glass skin. Also, there is glass on about two inches on the other side of the antenna towards the aircraft and separated by air. Therefore, this relationship describes the wavelength change but an effective dielectric constant would need to be calculated including the FR-4 substrate ($e_r = 4.0$). Therefore, the complex and irregular geometry has been modeled.

While reducing the dimensions of antennas are often desirable, the compromise is a narrowing of the bandwidth [40, 59]. Lamensdorf showed that the bandwidth decreases as the dielectric constant increases for a given geometry through the widths of admittance curves narrowing [40]. The narrowing in the curve limits the frequencies where the antenna exhibits a good input match with the feeding transmission line. The antenna integrated with the S2-glass shown in Figure 4.1 shows the reduction in bandwidth as indicated by these studies. The shift in resonant frequency is more dominant at the higher frequencies than the lower frequency. The glass increases the Q value or the energy stored in the reactive near-field of the antenna, which reduces the bandwidth [20]. The dielectric glass increased the reactive near-field and decreased the bandwidth, which had a greater impact on the higher frequencies as the capacitance increased. Compensation for this effect can be accomplished as shown in Figure 4.2 with the wing elements, which is a unique feature of this antenna. The wing length adjustments modify the other resonant frequencies and shifts them closer to the primary resonance occurring around 150 MHz.

The result for an antenna in free-space and on only glass is shown in Figure 4.3, which

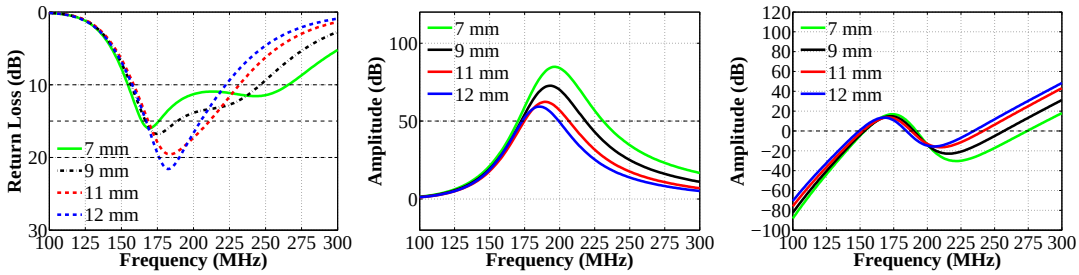

(a) Return Loss (b) Real Input Impedance (c) Imaginary Input Impedance

Figure 4.2: Compensate for Glass with Wing Length

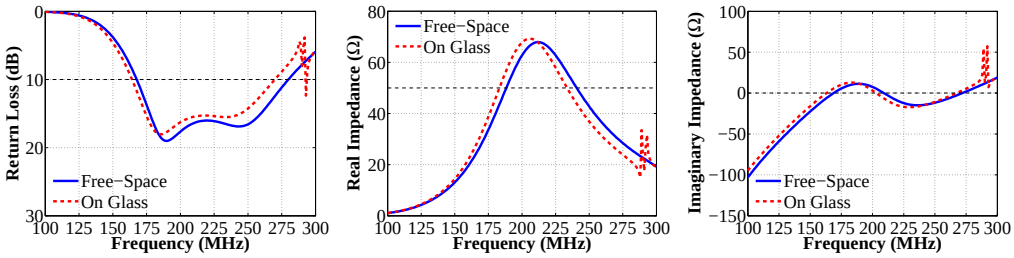

(a) Return Loss (b) Real Input Impedance (c) Imaginary Input Impedance

Figure 4.3: Free-Space and Only Glass Simulation Results Comparing the Rev. 2 Antenna

does not include any balun integration. The simulation indicates that the glass shifts the impedance higher when at the maximum and shifts the results to lower frequencies for the real part of the input impedance. Also, the imaginary component does become more capacitive at the null and shifts to lower frequencies too. Therefore, these simulations have indicated that the measured lowering of the maximum real input impedance is caused by the presence of the doublers. These doublers also appear to cause an increase in the null of the input impedance. The glass is responsible for increasing the capacitance and shifting the response to the lower frequencies as demonstrated by both components of the input impedance. This in agreement with previous studies on dielectric loading antennas. It has been shown that a larger relative permittivity will lower the resonant frequency, increase the peak admittance and narrow the bandwidth [59].

4.1.2 Mutual Coupling

The integration of the antenna with the glass and doublers motivated the antenna modifications but also the high levels of mutual coupling. As described in Section 2.2.1, mutual coupling can adversely affect the radiation pattern, input impedance/match and

signal quality. Several approaches were taken to understand and then reduce the mutual coupling. First, sweeping the length of the antenna showed that the mutual coupling linearly decreases by shortening the antenna. The mutual coupling was strongest around the lower frequency of operation. This separation between the antennas is electrically shortest at the lower frequencies, so logically the coupling would be the strongest. Distance is a known contributor to mutual coupling. The bow-tie elements had a set spacing, which could not be adjusted between the revisions without shrinking the size of the antennas. This is due to the fixed size of the aerospace fairing. Therefore, the centers of the antennas are confined to the same positions and coupling cannot be reduced through separation or orientation. The characteristics of each antenna must be modified to reduce the coupling.

The fundamental mechanisms of coupling are capacitive and inductive. Capacitive coupling can be achieved through parallel plates that provide places for charge to accumulate and a create voltage difference. Similarly, parallel current paths or loops of currents cause inductive coupling. The bow-tie antennas have wide flat surfaces at the antenna ends. When in the array, these ends are two flat surfaces separated by the distance in between antennas and can appear to be plates in the same plane, which have capacitive coupling but not as much as parallel plates [77]. Similarly, currents flowing across these elements produce magnetic fields, which then create inductive coupling with the adjacent element. The charge difference between the ends of the two plates and the presence of currents on the ends provide explanations for capacitive and inductive coupling between antennas.

These fundamental mechanisms are abstract explanations for the mutual reactance between multiple bow-tie antennas, but currents have been shown to exist along the back edge where they do not contribute to the radiation. As discussed in 2.1.2, the biconical antenna has similar characteristics as the bow-tie antenna, but it is three-dimensional. The current flows along the length of the antenna and then along the rim of the cone at the ends [76]. This current would ideally produce radiated fields if the structure was infinite, but the finite structure provides a current path at the end caps. This current is equivalent with current flowing along the bow-tie's edge due to its finite length. Several papers have presented results showing currents along this edge [27, 41, 42, 57]. These currents would produce magnetic fields that interact with the magnetic field produced by the adjacent element and create a mutual inductance term. From the revision one measurements, the mutual reactance becomes inductive around 150 MHz where the mutual coupling is highest, as shown in Figure 3.43. Therefore, currents along the back edge of the bow-tie are assumed to contribute to the mutual coupling.

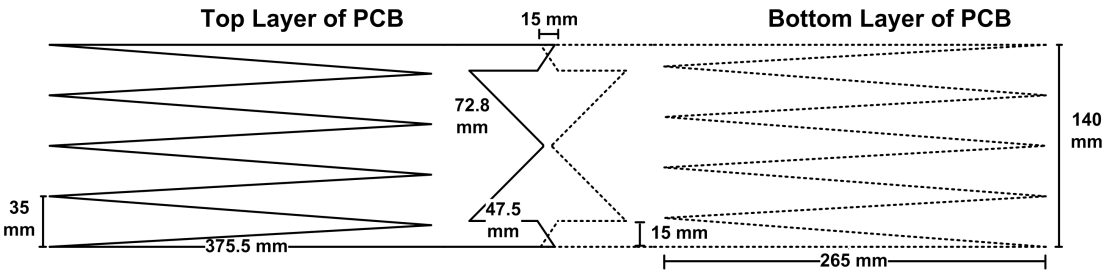

Figure 4.4: Revision 2 Antenna Dimensions

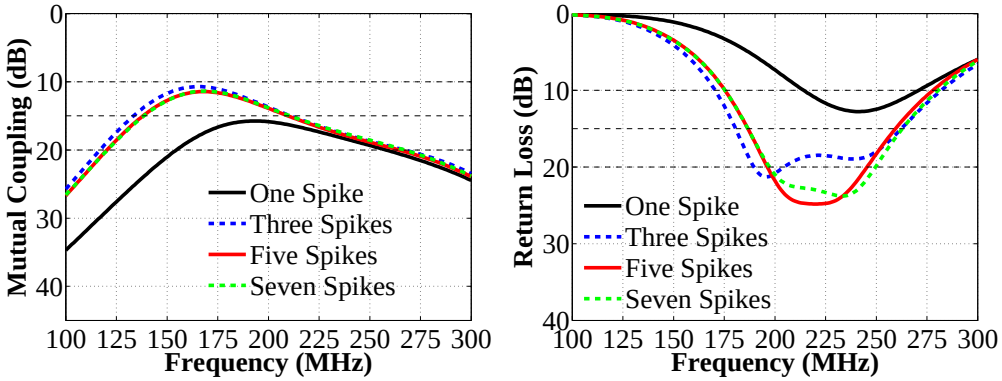

(a) Mutual Coupling

(b) Return Loss

Figure 4.5: Spiked Elements Affect on Mutual Coupling and Return Loss

Reduction of the mutual coupling required limiting the transverse currents flowing along the back side of the bow-tie. These currents were reduced by not allowing a straight line for the currents to flow. This concept was implemented by adding spikes that went from one side to another as shown in Figure 4.4. Several designs were simulated with one through seven spikes along the back edge. A comparison for the different spikes is shown in Figure 4.5. The addition of the spikes increased the mutual coupling, but improved the bandwidth response for the antenna. As more spikes were added, the bandwidth is less impacted by the addition of the spikes, but after five spikes little difference is noted in the return loss. Similarly, the mutual coupling increased with the addition of the spikes but remained consistent beyond one spike. The final configuration with five spikes reduced the mutual coupling by 3.5 dB (from -7.2 dB to -10.7 dB) at the peak as shown in Figure 4.6.

The reduced mutual coupling may be bounded by antennas that do not have transverse currents, and thin dipoles are assumed not to have transverse currents and exhibit a theoretical limit to the mutual coupling. Many have studied the effects

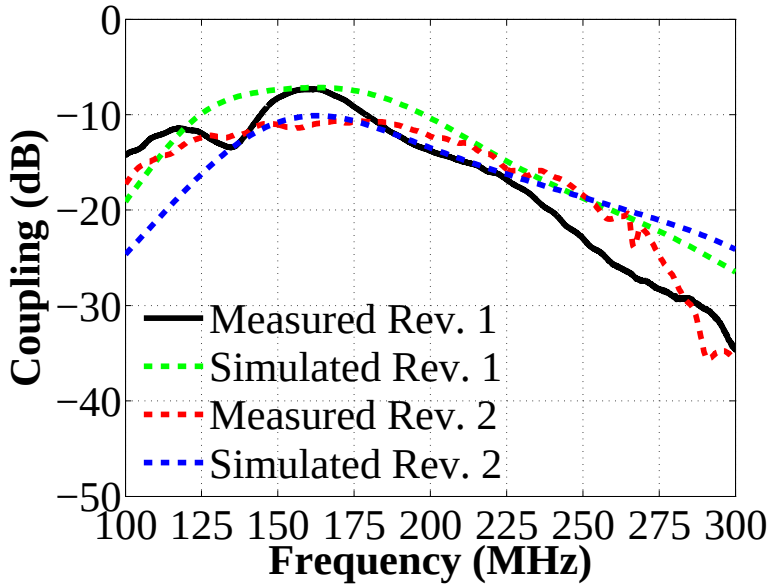

Figure 4.6: Mutual Coupling of Rev. 2 Antennas 5 and 6 on Skins

of mutual coupling for thin dipoles showing various results, and these results do not completely agree [8, 18, 72, 76]. Several studies propose mutual impedance values for half-wave dipoles with values below $\lambda/2$, which is not physically possible due to the dipole's physical space overlapping the adjacent element. Elliot considered the space that the dipoles occupied, and solved equations based on Maxwell's equations shown in his book [18]. This result shows the mutual impedance up to about 0.6λ, where the real component is around 15 Ω. This result is fairly close to an HFSS simulation consisting of a thin dipole operating at a center frequency of 195 MHz, where the real component of the mutual impedance at 0.6λ was around 25 Ω. It is worth noting that the simulation produced a result that was not completely the same as the results proposed by Elliot, but at this same separation, Stutzman and Thiele proposed a real mutual impedance around 7-9 Ω [72]. The method used by Stutzman and Thiele is not explicitly stated. Also, Balanis presented results around -4 Ω using an induced electromagnetic force method and Method of Moments (MoM) [8]. Therefore, the variation calculated using HFSS was taken as acceptable.

The thin dipole example was further explored to more closely resemble the configuration for the bow-tie antennas, because the presence of a ground plane affects the mutual coupling. The simulation results below show the mutual coupling and mutual impedance for varying ground plane distances. The presence of the ground plane increases the mutual coupling for a distance of 0.5λ by 1.4 dB to a maximum of

11 dB from 12.4 dB without a ground plane. Therefore, the measured and simulated peak for the bow-tie antennas around -10.7 dB approaches the level for thin dipoles, which do not exhibit currents at the end-caps.

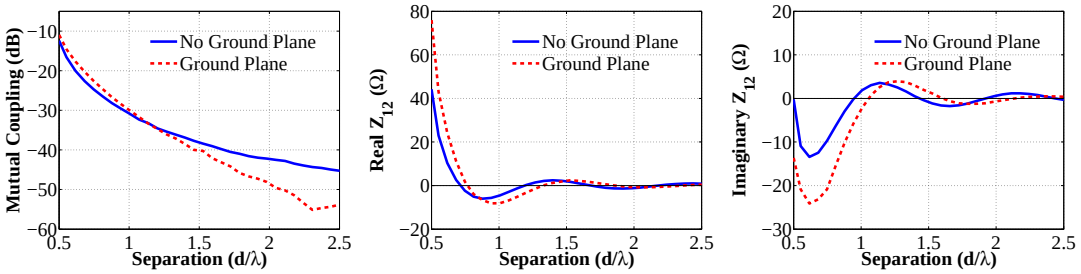

(a) Return Loss (b) Real Input Impedance (c) Imaginary Input Impedance

Figure 4.7: Collinear Array Mutual Coupling for Thin Dipoles

4.1.3 Design Comparison for Various Array Positions

This final design was also simulated with doublers. Doubler sizes, positions and gaps were not kept constant across each antenna, so analysis was performed on all the doubler configurations for in the inboard array during the initial design phase. Two results were presented in Figure 4.8 with the antenna lengths of 68 cm and 64 cm. The shortest antenna offered the best mutual coupling advantages as well, since the distance between elements was electrically longest. Note that Figure 4.8a showed resonances occurring around 280 MHz. These artifacts occur as the simulation becomes more complex with thin doublers in close proximity to the glass and antenna.

At this point the discussion will not focus on the doubler configuration, but rather the antenna performance across the different relative positions. The doubler configuration used for these antennas is discussed in Section 4.3 and shown in Figure 4.22d. Variation 1 performs more consistently across several doublers with the lowest operating frequency ranging from 165–170 MHz. As the antenna shrunk in size, the doubler configurations increasingly affected the performance from one antenna to another. The relative dimensions of the doublers had a greater impact when the antenna was shorter. These two iterations had the same wing length of 7.5 mm, which may be adjusted to improve antenna 5 for variation 2. Note that this wing length had improved results after adding the spikes and doublers. However, this tended to decrease the performance of antenna 8. This trade-off was noticed for other designs such as variation 1, but the difference between the two were less noticeable. Antenna 5 has doublers around the center of the antenna, while antenna 8 was free of doublers except for the ends. In this configuration,

the longer antenna was less affected by the doublers near the input. This concept will be further discussed in Section 4.3. In general, each antenna should perform the same, so it is desirable to reduce the variations from one antenna to another.

The spiked elements also had an impact on the end-loading effect discussed in Section 3.3.1. The shift caused by these doublers did not impact this antenna as much as in the revision one antenna as shown in Figure 4.9. The decreased currents along the back edge of the bow-tie also had an impact on the coupling to the parasitic top-hat. Less current is coupled onto the doubler, so the current distribution is not altered as much. In the case of the top-hat, current continues to travel outward allowing the current distribution to become more uniform for the lower frequencies. This current is not coupled onto the doubler, and this effect does not occur as much as the first revision antenna.

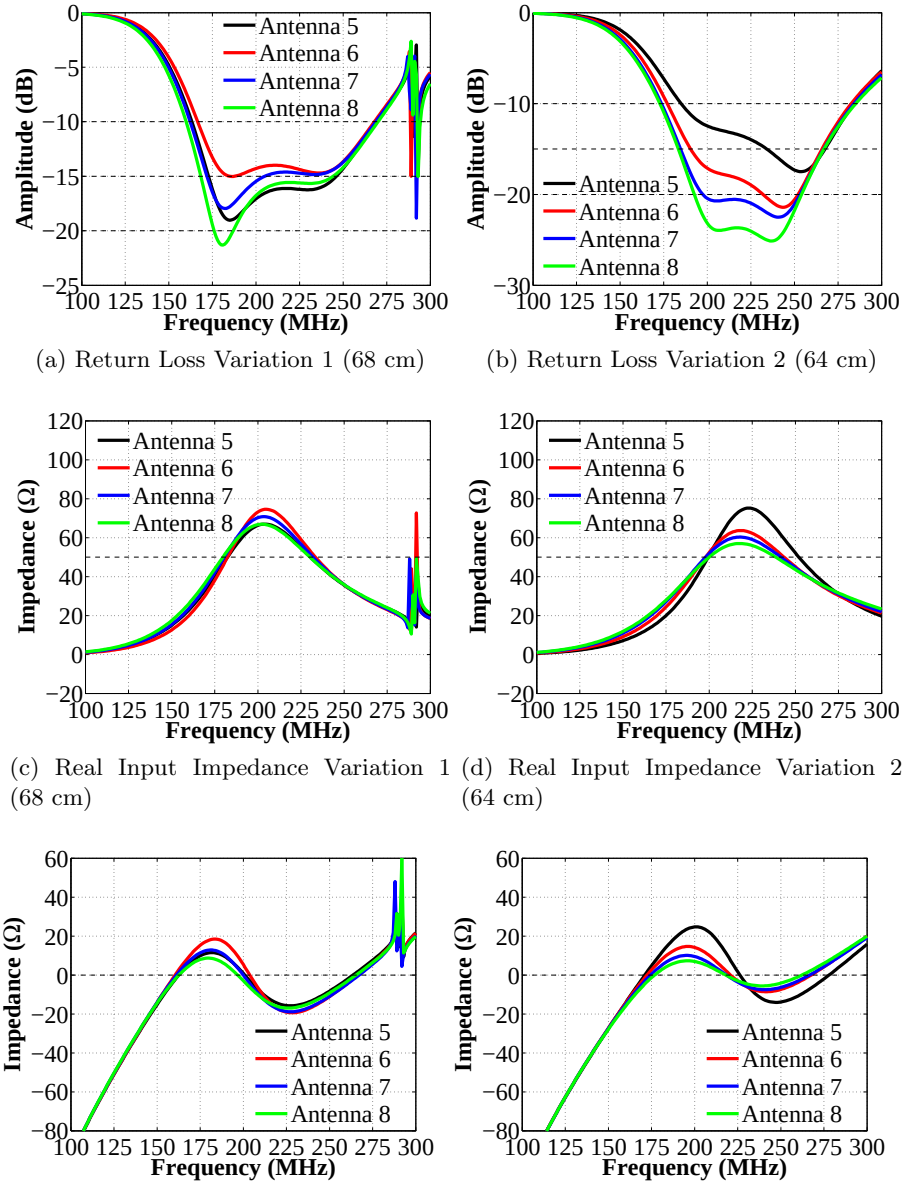

(a) Return Loss Variation 1 (68 cm)

(b) Return Loss Variation 2 (64 cm)

(c) Real Input Impedance Variation 1 (68 cm)

(d) Real Input Impedance Variation 2 (64 cm)

(e) Imaginary Input Impedance Variation 1 (68 cm)

(f) Imaginary Input Impedance Variation 2 (64 cm)

Figure 4.8: Return Loss for Two Antenna Iterations

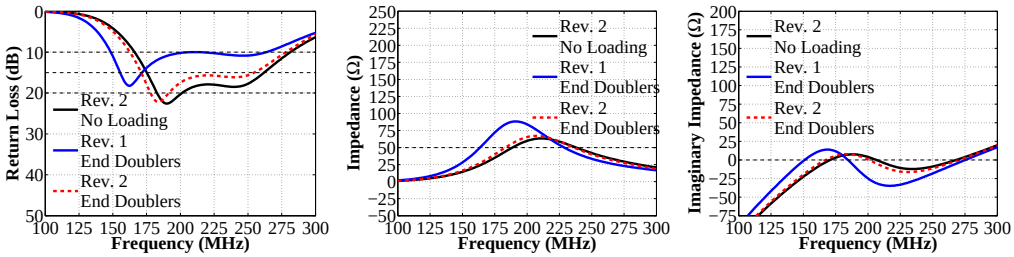

(a) Return Loss (b) Real Input Impedance (c) Imaginary Input Impedance

Figure 4.9: Comparison of End-Doubler's Effects on Rev. 2 Antenna 8 Compared with Rev. 1

4.2 Balun Improvement

The first revision baluns were functional, but it is desirable to reduce the insertion loss and maintain better balance. For the second revision, the balun design remained a ferrite transmission line transformer as was used in the first revision for the wideband operation and high power handling capabilities. This balun is constructed using 20 AWG twisted-pair and a 43 material ferrite binocular core (Fair-Rite Part Number 2843009902). As mentioned in Chapter 3, the large 43-material ferrite balun did not experience as much heating as smaller, similar binocular core ferrites operating at high power. The heating occurred due to the magnetic flux being absorbed into the ferrite material, which is a loss of energy and one cause for the insertion loss. However, mitigating the loss due to the magnetic flux is dependent on the ferrite material. On the other hand, wire loss is another factor in the insertion loss. During balanced operation, most losses are resistive and little is lost in the ferrite core [49]. Some transmission line transformers consist of trifilar designs. These designs improve the lower frequency response of the balun, but add approximately 0.5 dB of loss to the higher frequencies [60]. The higher frequencies needed the improvement from revision one. The approach for minimizing the loss was to reduce the number of turns. The reduction of turns from three to two minimizes both the loss absorbed in the ferrite and the wire loss. Since the ferrite has one less turn, then less wire is used and less current passes through the ferrite, which means less magnetic flux coupled into the ferrite. The results from the first revision are shown again next to the results for the balun with less turns in Figure 4.10. As shown in Figures 4.11a and 4.11b, the insertion loss for the revision 1 baluns was never below 0.5 dB for both outputs and the loss for each output began diverging at 160 MHz.

After the turn was removed, the loss was the same at both outputs and was slightly lower as shown in Figures 4.11a and 4.11b. However, the insertion loss exceeded

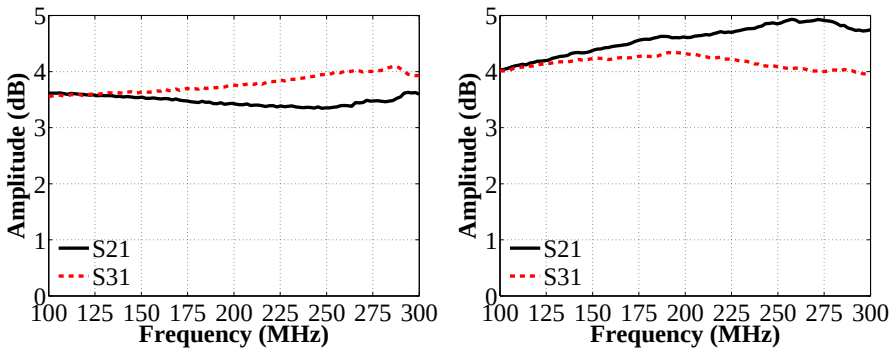

(a) Balun 1 (b) Balun 2

Figure 4.10: Original Balun: Loss to Each Output

1 dB around 240 MHz and was close to 1.5 dB by 260 MHz. If the antenna return loss measurement was performed at 240 MHz, then the two way loss of the balun would be 2 dB, or in other words, there was 2 dB of loss from the radar signal from transmit and received signals combined. Similarly, there would be 3 dB of loss at 260 MHz. Mini-Circuits provides similar baluns that generally have an insertion loss of 0.5 dB throughout antenna bandwidth for low power applications (Example Mini-Circuit Part Numbers: ADT1-6T+, TC1-1-13MA+, TCL1-ED12665/1, and ADTL1-12+). However, this balun was designed for high power applications than the commercially available baluns of similar design. Future work may be desirable to limit the increasing insertion loss at the higher frequencies.

In comparison with revision 1, the loss was equally spread between the two output ports. As the signal was either transmitted or received from the antenna with unequal loss to each side, this causes the current distribution to vary from the desired half-wave dipole and will cause radiation to be in an undesirable direction [72]. In order to maintain proper radiation characteristics, the dipoles should have equal magnitude but opposite phased currents on both halves. The insertion loss through the balun being unequal may disrupt the currents.

The baluns were measured using a 4-port network analyzer (Agilent N5230C) on a revised test jig to better emulate the balun as mounted on the antenna. The original test jig had two separate ports for the outputs as can be seen in Figure 4.12 with the top copper removed. The output wires were twisted and separated to connect to the ports. The input cable is used to create a common reference or ground as it is soldered to the ground plane on the back, which connects to the shields of the other ports through the SMA connectors. The improved test jig utilized vias to solder the wires, which was also incorporated into the second revision of the antenna. In both the antenna and the

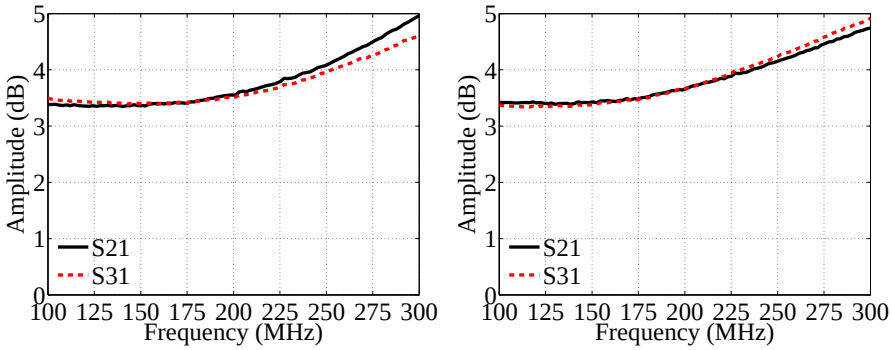

(a) Balun 1 (B02) (b) Balun 2 (B20)

Figure 4.11: Revision 2 Balun: Loss to Each Output

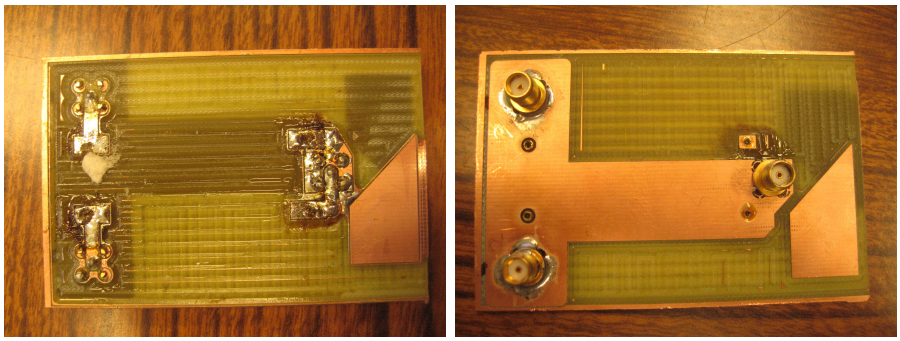

(a) Top (b) Bottom

Figure 4.12: Revision 2 Balun Test Jig

test jig, the vias ensured that the balun wires were mounted in the exact position and improved consistency through testing and antenna fabrication. The new test jig is shown in Figure 4.12a and 4.12b. Note that the bottom shows the reference connected using a ground plane, which was not part of the antenna and therefore a deviation from testing in the installed environment. These balun measurements were measured as Touchstone files (.s3p) and imported to Agilent Design Studio (ADS) to be integrated with the HFSS antenna simulation. Note baluns B01-B06 and B20 were measured correctly with the test jig, and the other baluns were not soldered correctly to the test jig. This was not noticed until after the antennas were tested and sent to the aerospace team for installation onto the fiberglass skins.

The balun influenced the antenna performance. During validation of the second revision of the antenna several tests demonstrated that the same antenna can have a more narrow bandwidth or a wide bandwidth, depending on the balun. As shown in

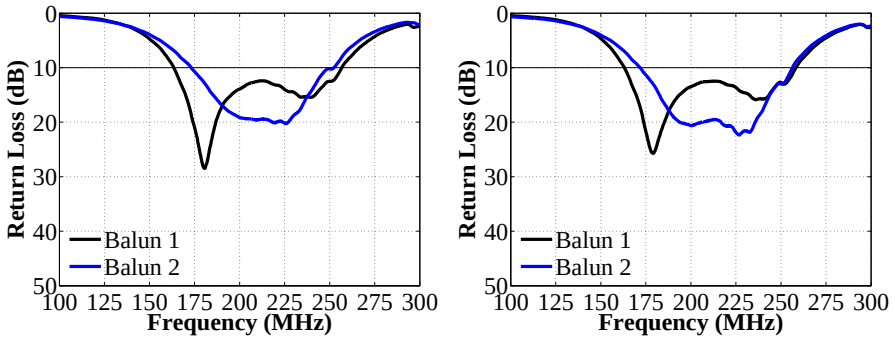

(a) Antenna A (b) Antenna B

Figure 4.13: Revision 2 Antennas with 2 Baluns

Figure 4.13a the same antenna with two different baluns performed differently. The same effect was repeated with a different antenna and the same two baluns in Figure 4.13b. The two different antennas performed very similarly when the same balun was attached.

Further analysis of the baluns showed that balun orientation affected the input match as shown in Figure 4.15. Four different orientations are possible for a balun with a twisted pair. Assume after the balun was wound that there is a top, bottom, front and back, then there can be 4 different positions for this balun. Calling the standard position where the top is shown from an aerial perspective with the front attached to the antenna input port. This can be flipped if the front is attached to the feed cable port and the top is still shown from an aerial perspective. Next the balun can be upside down with the bottom showing from an aerial perspective. Again the front can be positioned at the antenna port (upside down) or at the feed cable port (upside down and flipped). During the process of re-orientating the balun, care was taken as to not change the wire positions more than necessary. While the same balun has generally the same trends, there are notable differences in performance particularly shown in Figure 4.14a from the standard to the flipped.

The balun orientation study indicates that the difference between how the wires exit the front and back affect their impedance. It has been shown that the twist angle, wire size, wire insulation thickness, and insulation relative dielectric constant affect the characteristic impedance of two parallel wires [44]. While equations may provide ideal impedance values, construction of transmission line transformers in reality have uncertainty and inconsistent wire spacing and the effects of mutual reactance (inductive and capacitive) with neighboring turns [65]. Therefore, inconsistencies with spacing and turn position are to be considered in order to improve performance across multiple

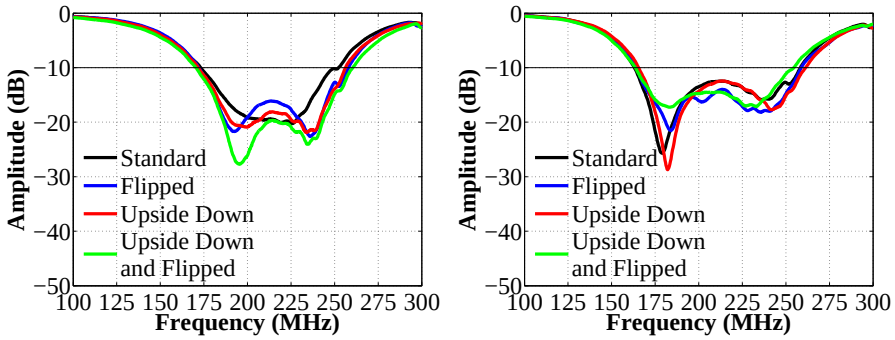

(a) Antenna A with Balun 2

(b) Antenna B with Balun 1

Figure 4.14: Revision 2 Antennas with Different Balun Orientations

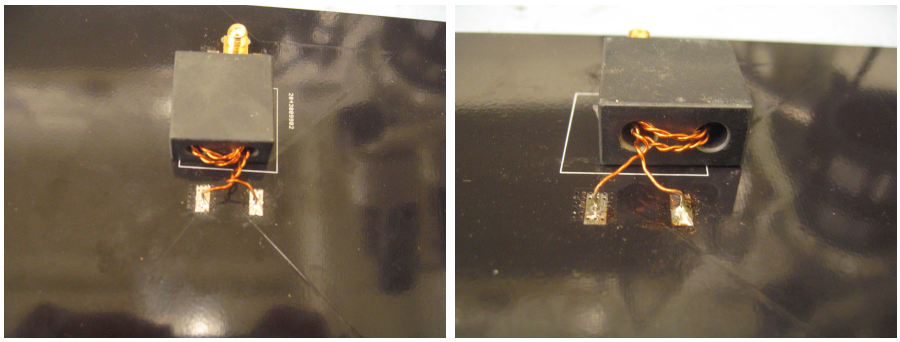

(a) Low Exit

(b) High Exit

Figure 4.15: Balun Wires at Antenna Port

baluns and antennas. Most notable visual differences in the baluns measured above are the wire winding, lead lengths and the position exiting the balun. As shown in Figure 4.15a the twisted pair exit the balun from the lower right hole for this perspective. Similarly, Figure 4.15b shows the wires exiting the top, left hole. The tightness of the twisted pairs is also notably different in the two images.

After comparing the results of the pair exiting the top and the bottom, it was decided to manufacture the baluns with the baluns exiting from the bottom. This implies twisting each balun using the same method. Maintaining consistent the same twists per inch, lengths of twisted pair on both sides of the balun and the same relative position of twists within the core are important for the consistency from one balun to the next. The measured results for 15 baluns is shown in Figure 4.16. Note that balun numbering omits certain baluns that did not perform as well as others and therefore were not installed on the antennas for the free-space measurement. These measurements assume that the baluns were the major contributing factor to the antenna performance

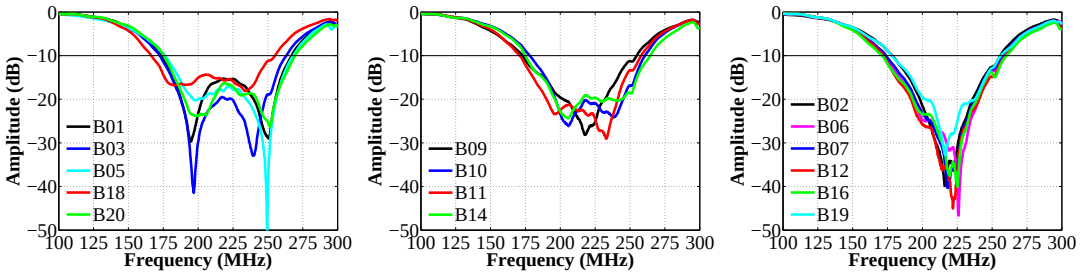

(a) Antenna Set 1 (b) Antenna Set 2 (c) Antenna Set 3

Figure 4.16: Antenna Free-Space Results showing balun impact on antenna performance

variations. It can be seen from these results that the baluns either produce a wider dual resonance or a more narrow dual resonance with a deeper null. However, the peak between the wider dual resonance remained greater than 15 dB return loss, and therefore is acceptable. These baluns were constructed having 1.25 mm twisted pair length on the feed cable connector side and 2 mm on the antenna input port side. Since some baluns were not properly measured on the network analyzer with the test jig, the simulations in ADS will include baluns that performed similarly or within the same set in Figure 4.16. Each group, except antenna set 2, had at least one balun with valid test jig measurement results. The coordination of each balun with the installed antenna position is shown in Table 4.1. Also, the baluns were glassed onto the antennas with a thin strip of S2-Glass that did not cover the magnet wires. This made sure the baluns were secured to the antennas to avoid vibrations during flights.

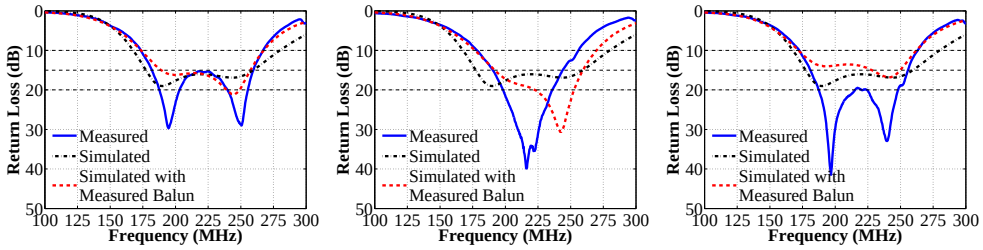

(a) Antenna 1 (b) Antenna 2 (c) Antenna 3

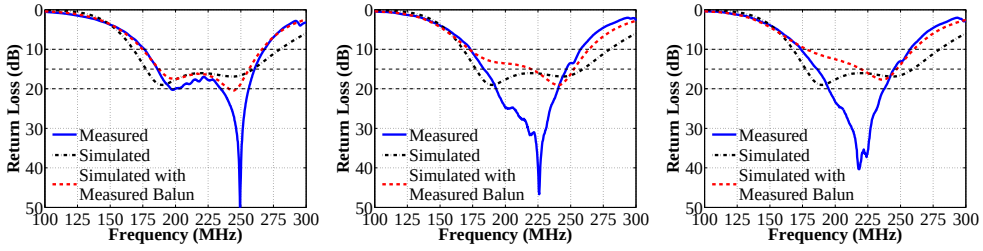

(d) Antenna 4 (e) Antenna 5 (f) Antenna 6

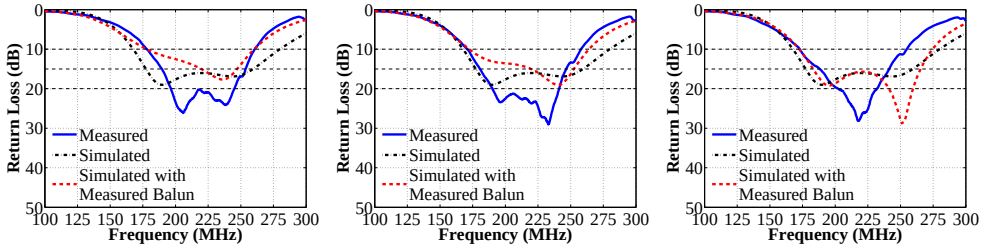

(g) Antenna 7 (h) Antenna 8 (i) Antenna 9

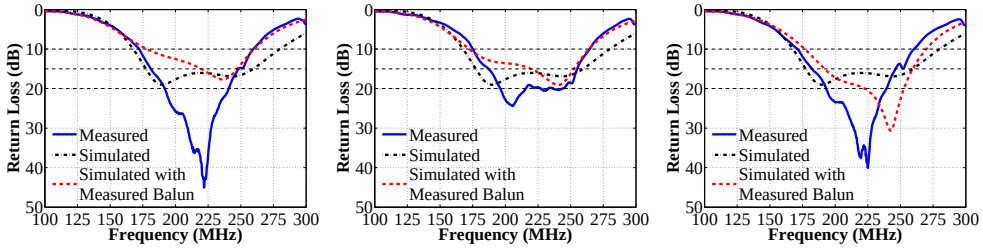

(j) Antenna 10 (k) Antenna 11 (l) Antenna 12

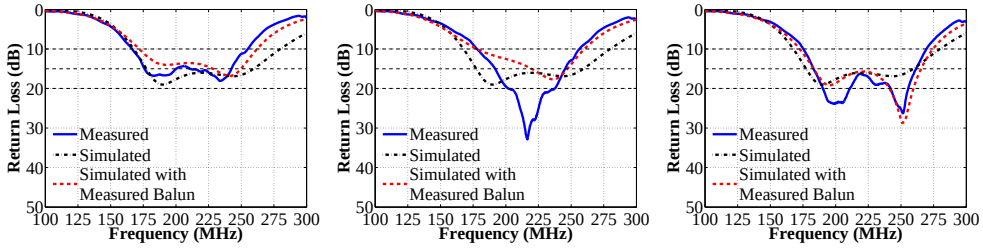

(m) Antenna 13 (n) Antenna 14 (o) Antenna 15

Figure 4.17: Free-Space Return Loss Measurement and Simulation Comparison for Rev. 2

Table 4.1: Antenna and Balun Numbering

Antenna Position	Array Position	Antenna Number	Balun Number	Balun Used for ADS Simulations
1	Port	A01	B01	B01
2	Port	A02	B02	B02
3	Port	A03	B03	B03
4	Port	A04	B05	B05
5	Inboard	A05	B06	B06
6	Inboard	A06	B07	B07
7	Inboard	A07	B09	B07
8	Inboard	A08	B10	B06
9	Inboard	A09	B11	B20
10	Inboard	A10	B12	B07
11	Inboard	A12	B14	B06
12	Starboard	A14	B16	B02
13	Starboard	A16	B18	B03
14	Starboard	C	B19	B07
15	Starboard	D	B20	B20

4.3 Doubler

During the design of the first revision fairing, long doublers adversely affected the antenna performance. Modifications were applied after fairing construction, and slots were drilled through the doublers. These slots mitigated the degradation but potential improvements through further modifications were possible for the second revision. The goal of these modifications was to reduce the doubler parasitic effects on the antennas, so the bandwidth would not be diminished. Maintaining the bandwidth through the different stages of integration with the structure indicates the effect of each structural component had on the antenna performance. The mitigation approach was to reduce the doubler lengths, increase gaps between doublers and increase the distance separating the antenna from the doubler. As shown in Section 3.3.1, the parasitic lengths and separation from the antennas affect their influence on the antennas. The gaps also played a roll in the capacitance between the parasitic elements. The maximum gaps were limited due to structural needs, and as the gap increased, the overall lengths of the doublers decreased since the fairing had a confined length. The first section shows a controlled measurement study showing the investigation of the doubler effects. The next section describes the physical changes implemented to the doublers while the final section presents results and discussion regarding the doubler changes.

4.3.1 Controlled Measurement Study

An experiment evaluated the effects of the doublers while minimizing the complexity of the aircraft fairing to a controlled measurement setup. One antenna was set on a polycarbonate sheet in order to provide a planar support for both the antenna and the doublers. The antenna alone was measured with and without the polycarbonate dielectric. The polycarbonate caused the resonance to shift 5 MHz lower. The aluminum doublers used in this study are all 23.5 cm x 5.9 cm x 0.1 cm. Three collinear doublers parallel to and on both sides of the test antenna are arranged in different combinations to investigate their effects. In the first variation, the distance between the antenna and the doublers was varied to find an acceptable distance without a significant degradation in performance. Mutual coupling between the antenna and the doublers is primarily determined by the distance between them. In the second variation, the gaps between the doublers were varied, keeping the distance between the antenna and the doublers constant to find the optimal gap size. The structural requirements limit the gap size to provide strength throughout the fairing. The gaps between the doublers determine the coupling between doublers and may be improved to limit the magnitude of current that can be capacitively coupled from one doubler to another.

Polycarbonate was mounted between plastic sawhorses using wooden dowel rods and elevated above a ground plane as shown in Figure 4.18. The dimensions of the polycarbonate are 107.9 cm x 100.3 cm x 0.6 cm. The ground plane was spaced at a distance of 41.91 cm and has dimensions of 121.9 cm x 121.9 cm. Care was taken to minimize the cable effects by directing it up and away from the antenna and perpendicular to the feed. The antenna was measured using an Agilent N5230C vector network analyzer (VNA) and a 5.2 meter LMR200 cable.

The measurement results with and without the three doublers on each side of the antenna are shown in Figure 4.19. These doublers are spaced at 3.1 cm, 8.2 cm and 13.3 cm away from the antenna. During each iteration of antenna-to-doubler distance, the gaps between the doublers were held at a constant 1.9 cm.

The doublers of the same length and same gap size lowered the resonant frequency to approximately 185 MHz and increased the return loss to around 17 dB. This remained true regardless of the spacing between the antenna and the doublers. The currents coupling between the doublers and the antenna has an effect similar to the well-known end-loading technique to reduce the resonant length of an antenna. This may be a desirable characteristic, but in the configuration shown, the the return loss is also reduced. The return loss demonstrates an antenna's radiation efficiency and this characteristic is crucial to radar systems for the reception of weaker target returns.

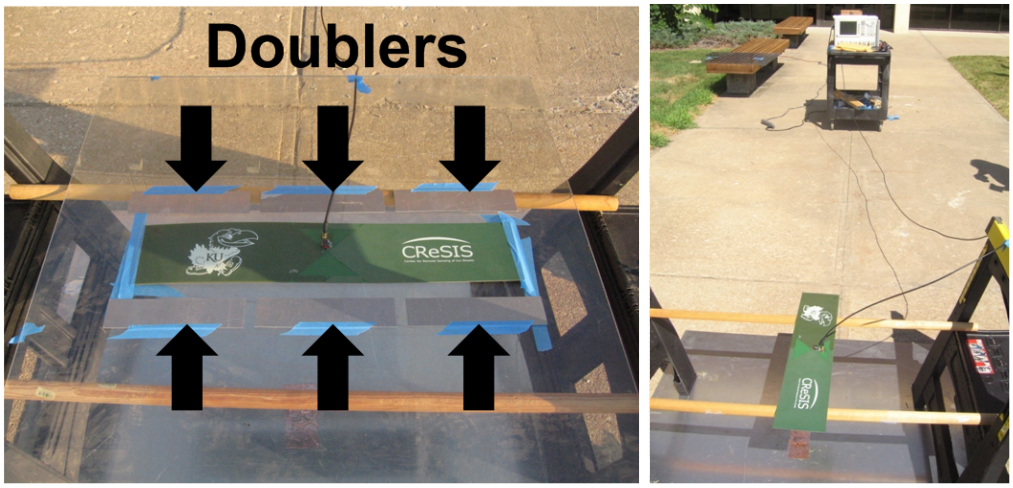

(a) Antenna Setup (b) Measurement Setup

Figure 4.18: Controlled Measurement Setup

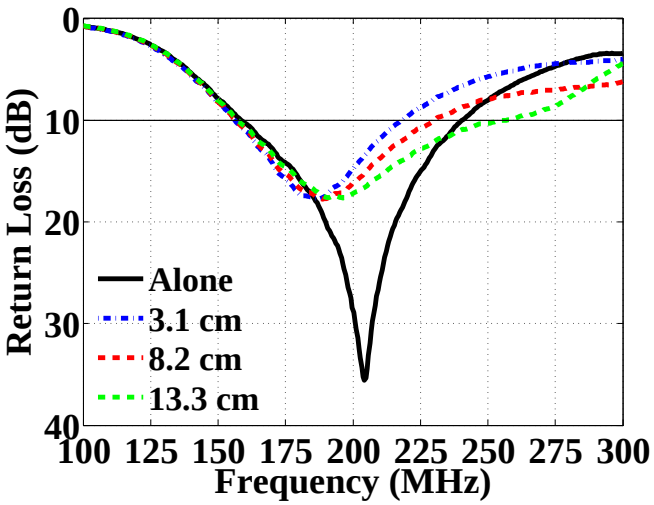

Figure 4.19: Doublers at Varied Distance Away from Antenna and Constant Gap

As the doublers increased in distance from the antenna, the bandwidth improved at the upper frequencies. This is an improvement, but the magnitude of the return loss is also reduced. It is generally desirable to increase both the bandwidth and the return loss when improving antenna performance. In practice the fairing contains other metal features that degrade the antenna's performance.

The return loss for the doublers at a constant distance of 3.1 cm away from the antenna and with varied gaps is shown in Figure 4.20. The gaps are 1.9 cm, 3.1 cm and 5.7 cm between each doubler. There were three doublers on each side of the antenna oriented in a collinear fashion.

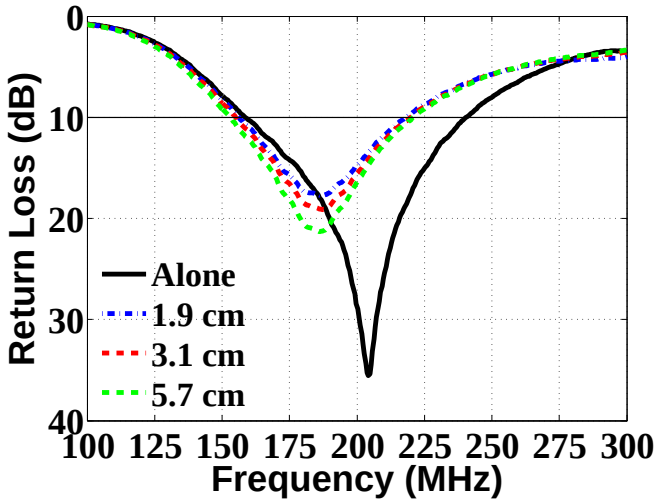

Figure 4.20: Doublers with Doublers Gap Increased at a Constant 3.1 cm Away from the antenna

As the gaps between each doubler were increased, the magnitude of the resonance was increased. The bandwidth did not improve as it had done when increasing the doubler's distance. Reducing the gaps to zero would result in one long conductor. As the gap increases, the three doublers on either side appear more individual and separated, though a certain amount of capacitance remains. As the gap increases, the electrical length increases but still remains small (3.1 cm $= 0.021\lambda$ and 5.7 cm $= 0.038\lambda$). Although this is not an ideal separation to minimize degradation to the bandwidth, these are the realistic constraints necessary to provide strength to the structure.

This study also included two measurement setups that indicated which doublers had the strongest impact. The nominal test setup had three doublers 3.1 cm away from the antenna on either side with 1.9 cm gaps between the doublers. The center doubler was removed, leaving the two outer doublers. Similarly, the two outer elements were removed leaving the center doubler. These results are shown in Figure 4.21. These

results are similar to configurations optimal for producing parasitic elements that create dual resonances or wide-band operation. When the center doubler was removed, leaving the two outer doublers, the result indicated that increasing the gap has a dimensioning effect. In comparison with Figure 4.20, the resonance does not appear shifted, rather the upper frequencies appear unable to resonate as efficiently. The return loss practically overlaps the measurement of the antenna without any doublers up to 190 MHz where it loses its radiation efficiency.

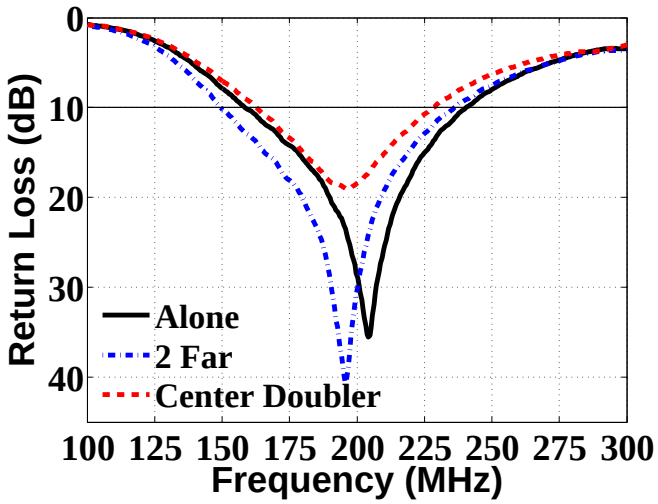

Figure 4.21: Center Doubler Removed Leaving Two Outer Doublers; Two Outer Doublers Removed Leaving Center Doubler

4.3.2 Rev. 2 Doubler Modifications

The implementation of these changes required the cross-discipline collaboration between electrical engineers and aerospace engineers to achieve performance regarding antenna bandwidth and aerospace structural strength. Stress reports analyzed by the aerospace team allowed removing several doublers, decreasing the lengths of existing doublers, splitting a doubler into two separate doublers and increasing the separation between the doublers. These changes were implemented and are shown in Figure 4.22 with their dimensions in Table 4.2 for half the inboard array. The inboard array is symmetric so the same doublers that surround antenna 5 also surround antenna 11, similarly for the following pairs: (antenna 6 and antenna 10) and (antenna 7 and antenna 9). This figure has revision 1 on top and revision 2 on bottom. The gaps between each doubler for the first revision is 21.6 mm. The separation between each doubler and antenna is 31.8 mm, except for doubler D3 that has a separation 8.3 mm. These separations were

increased to the following: 66.5 mm and 26.9 mm, respectively. The doublers kept the same names from one revision to the next and their dimensions are tabulated in Table 4.2 with the length defined following the same direction as the doubler name, i.e. the name doubler D13 is horizontal so the length is defined vertically.

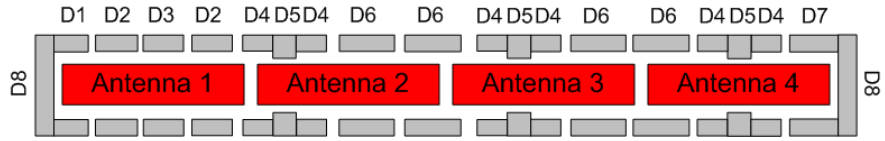

(a) Outboard Revision 1

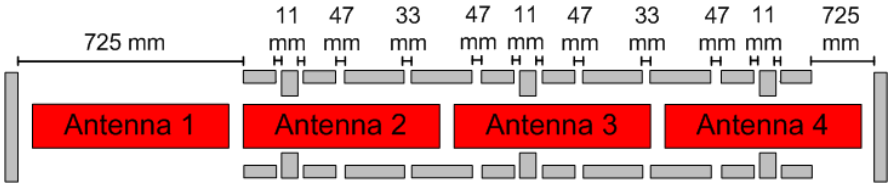

(b) Outboard Revision 2

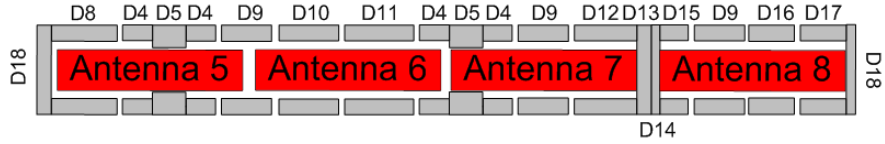

(c) Inboard Revision 1

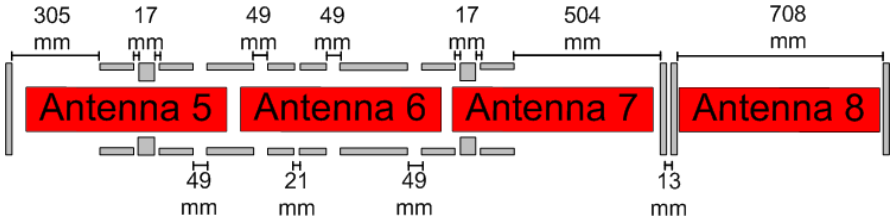

(d) Inboard Revision 2

Figure 4.22: Doubler Configurations for Rev. 1 and Rev. 2

Table 4.2: Doubler Dimensions

	Rev. 1		Rev. 2		Difference	
Doubler	Length (mm)	Width (mm)	Length (mm)	Width (mm)	Length (mm)	Width (mm)
D1	88	59	Removed	Removed	88	59
D2	156	59	Removed	Removed	156	59
D3	155	59	Removed	Removed	155	59
D4	111	59	111	31	0	28
D5	127	82	115	21	12	61
D6	220	59	213	31	7	59
D7	333	54	333	30	0	24
D8	245	59	Removed	Removed	245	59
D9	188	59	160	21	28	38
D10	224	59	90	21	43	18
			90	21		
D11	258	333	203	21	55	313
D12	233	59	Removed	Removed	233	59
D13	56	333	23	313	33	20
D14	31	333	21	313	10	20
D15	106	59	Removed	Removed	106	59
D16	170	59	Removed	Removed	170	59
D17	171	59	Removed	Removed	171	59
D18	333	36	313	21	20	15

4.3.3 Rev. 2 Doubler Modification Results and Discussion

First, the improvement between revision one and revision two is compared in Figure 4.23. Note that the connector for antenna 1 from revision one was broken during the removal of the skin from the fairing, so the return loss was not measured. In general, the average lowest frequency of the 10 dB bandwidth shifted from 145 MHz to 170 MHz between revisions. Similarly, the average high side of the bandwidth shifted from 217 MHz to 250 MHz. In addition, the bandwidth on average increased by about 5 MHz. The antennas integrated with the glass and doublers improved both in terms of center frequency and operational bandwidth from revision 1 to revision 2. This improvement includes the antenna and balun modifications.

While the 10 dB bandwidth indicates the operating range for each antenna, the magnitude of the return loss shows the input match through the operating band. The 10 dB bandwidth is one metric for comparing the improvement and the magnitude of the return loss is another. The most dramatic improvement is for antenna 8, which went from approximately 10 dB return loss to having a bandwidth greater than 20 dB. This can be accounted for by decreasing the top-hat loading from the spiked elements and the removal of side doublers. The majority of the revision one bandwidths greater than 15 dB were centered below 180 MHz, which was below the radar operating frequency. The average improvement for the 15 dB bandwidth was 37 MHz removing

the antenna bandwidths that do not include 195 MHz from the average. Similarly, the average improvement was 15 MHz for the 20 dB bandwidth. The average improvement for the 15 dB bandwidth was 17 MHz, and 20 dB bandwidth was 9 MHz without excluding the shifted resonant antennas. Therefore, the antenna re-design and doubler modifications were properly done to improve the center frequency considering that the glass and doublers were the major contributors to lowering the resonant frequency. Also, the limiting bandwidth effects caused by a combination of improvements between revisions, including the baluns and doubler configurations improved the bandwidths of the antennas integrated into the skins.

Analysis was also performed between the free-space and glassed to the skin return loss measurements. The results are shown in Figures 4.24, 4.25 and 4.26 for the return loss, real input impedance and the imaginary input impedance, respectively. As described in Section 3.3, the glass lowers the return loss by 4 MHz and 12 MHz for the 10 dB lower and upper bandwidth, respectively. This analysis was done through simulation, which showed agreement with the results in Figure 4.24. In general, the bandwidth at 10 dB was reduced by 8 dB with about a 9 MHz shift lower at the higher side and and 1.5 MHz on the lower side. This trend indicates that the dielectric loading limits the bandwidth more on the upper frequencies than the lower.

Further investigation into the skins' effect on the antenna was performed through the input impedance. The free-space and skin comparison of the real input impedance is shown in Figure 4.25 with a line at 50 Ω. A large spike in the input impedance occurs around 165 MHz. This maximum across most antennas decreases after the antenna was attached to the skin by about 37 Ω. This decrease in the maximum occurs around 160 MHz and did not sufficiently bring the input impedance close to the target 50 Ω. The lowering of the peak radiation resistance occurred due to coupled currents between the parasitic doubler and the antenna. The antenna couples current onto the doubler, which then a portion may be radiated or coupled back onto the antenna. This interaction occurs due to the magnetic fields of the current elements. The current induced back onto the antenna effectively reduced the input impedance.

Also, the null increases by about 6 Ω. Some antennas have the null below 50 Ω, so the impedance increase improved the antenna input match. The antennas that had improved input impedance matches include antennas 2, 5, 6, 8, 9, 10, 12 and 13. Most of these antenna showed return loss improvements are the frequencies where the null occurred indicating an improved input match. This is particularly noticeable in antenna 13 shown in Figure 4.25m where the input impedance was much below 50 Ω, but after integration with the skins the null was centered at 50 Ω. This then corresponds to an increasing of the return loss as shown in Figure 4.24m to more than 20 dB. On the other

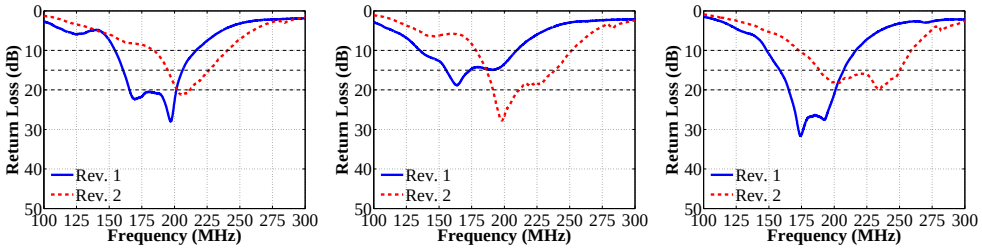

(a) Antenna 2

(b) Antenna 3

(c) Antenna 4

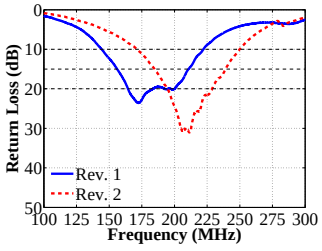

(d) Antenna 5

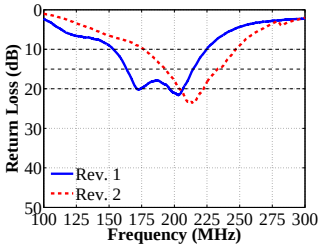

(e) Antenna 6

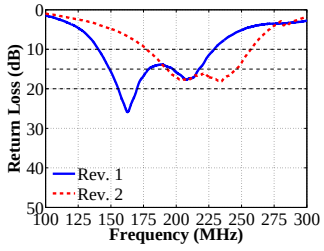

(f) Antenna 7

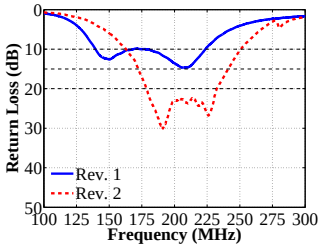

(g) Antenna 8

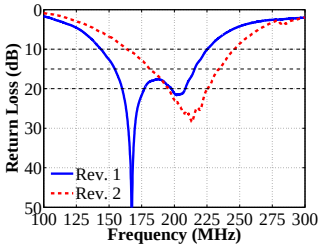

(h) Antenna 9

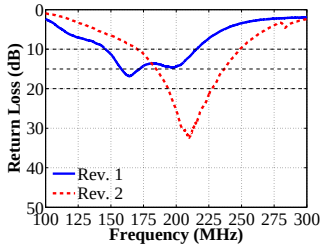

(i) Antenna 10

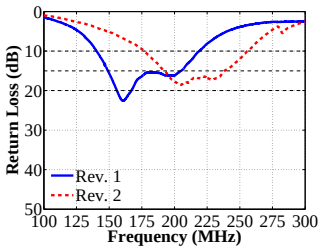

(j) Antenna 11

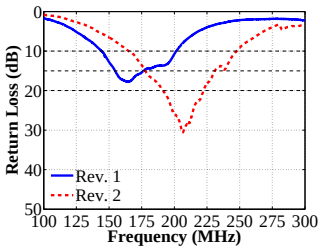

(k) Antenna 12

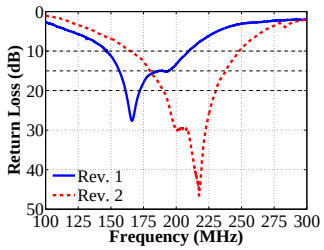

(l) Antenna 13

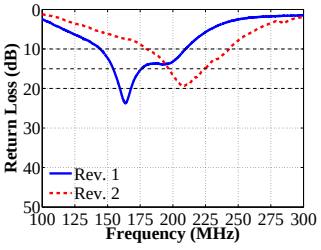

(m) Antenna 14

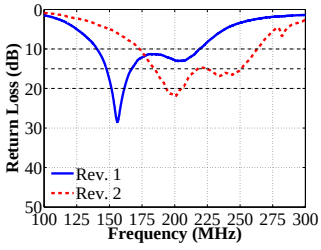

(n) Antenna 15

Figure 4.23: Skin Antenna Measured Return Loss Comparisons between Rev. 1 and Rev. 2

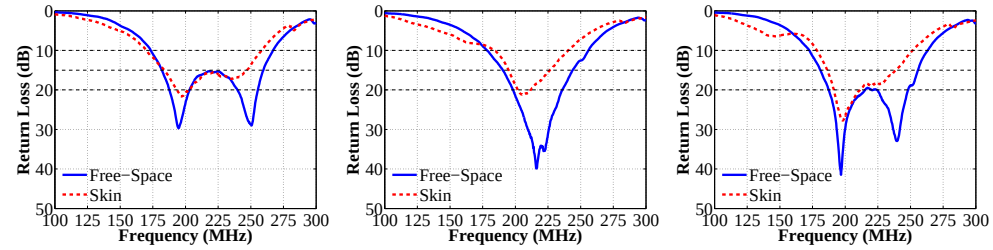

(a) Antenna 1 (b) Antenna 2 (c) Antenna 3

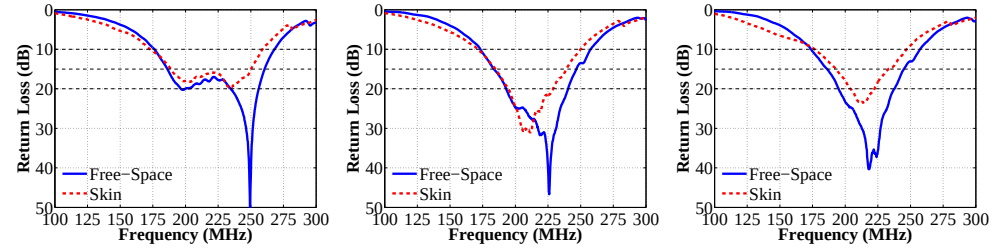

(d) Antenna 4 (e) Antenna 5 (f) Antenna 6

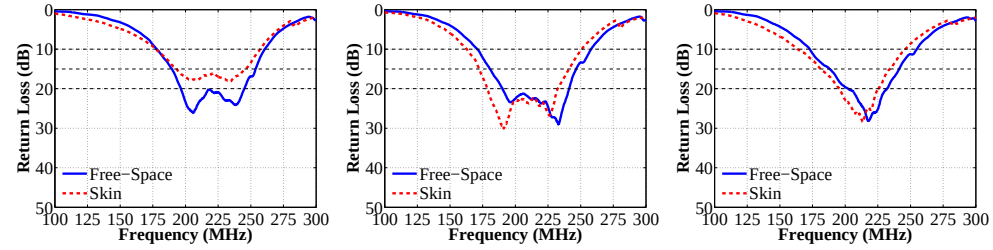

(g) Antenna 7 (h) Antenna 8 (i) Antenna 9

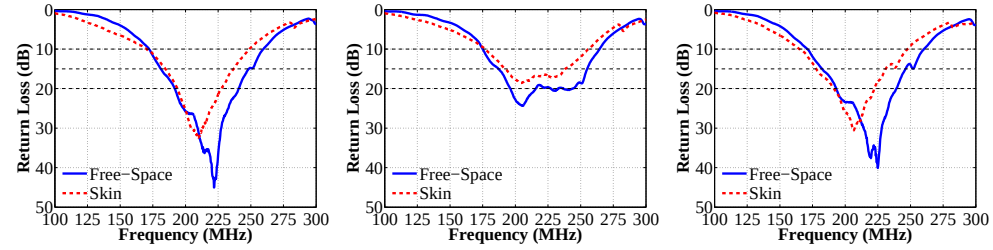

(j) Antenna 10 (k) Antenna 11 (l) Antenna 12

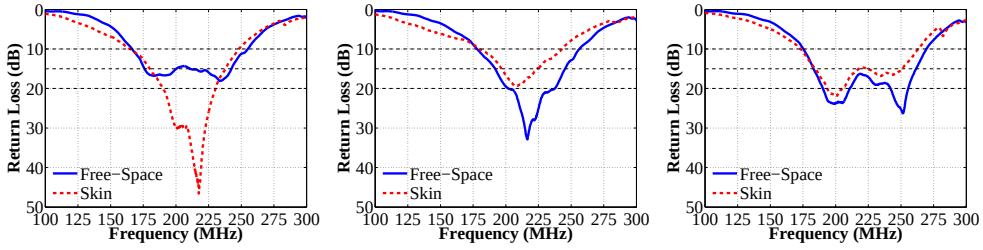

(m) Antenna 13 (n) Antenna 14 (o) Antenna 15

Figure 4.24: Free-Space and Skins Antenna Comparisons for Rev. 2 for the Measured Return Loss

side, antennas 2 and 6 had nulls below 50 Ω, and the return loss did not improve like antenna 13. This difference will be explained in the section discussing the imaginary component of the input impedance. The combined effect of lowering the peak and raising the null around the resonance is called resonance damping [48]. This effect can be desirable to broaden the bandwidth. In this case, the damping by increasing the null improved the antenna response more than lowering the peak.

While the skin had a positive contribution to the real input impedance, it had a negative impact on a few antennas. The null for some antennas was above 50 Ω and increased, which caused an increase in the separation from 50 Ω line. This occurred in antennas 1, 3, 4, 7, 11, 14 and 15. Each one of these antennas showed a decreased return loss.

In general, the addition of the skin caused the maximum in the input impedance to decrease and the null to increase. A conducting sleeve around the center of a dipole will increase the resistance [35]. This is observed with the decrease in the null, and the decrease in the real part of the input impedance is mainly attributed to the antenna's radiation resistance. This null is critical in the antenna performance, and in general the frequencies closest to 50 Ω should be maximized.

The imaginary component of the input impedance is important for the return loss and antenna bandwidth as well. The reactive component of the input impedance corresponds to the power stored in the antenna near-field [72]. Therefore, the imaginary component should ideally be zero, so the power is radiated rather than stored. As shown in Figure 4.26, the skin shifts the reactive component too. In general, the input impedance became more capacitive with the addition of the skin. The second null was often shifted to the left. The upward trend occurring around 160 MHz was often shifted to the left too. The combination of the downward and leftward shift was responsible for the decrease in the bandwidth at the higher frequencies. Similarly, the first null was increased around 175 MHz. This was responsible for the decrease in the lowest 10 dB frequency. As mentioned earlier, antennas 2 and 6 had a desirable shift in the real part of the input impedance but the return loss did not improve. In Figure 4.26b, the imaginary component of the input impedance had a peak at 0 Ω, which became more capacitive when the skin was added. This effect occurred most dramatically in antennas 2, 11, 12 and 14, which all had decreased return loss. This occurred to a slight degree for antenna 6. However, the first null increased and improved the antenna performance at the lower portion of the bandwidth.

While the glass alone was shown to increase the capacitance of the antennas, the doublers also increased the capacitance. The addition of a sleeve had the effect of adding a lumped capacitance in parallel with the antenna impedance, which would decrease

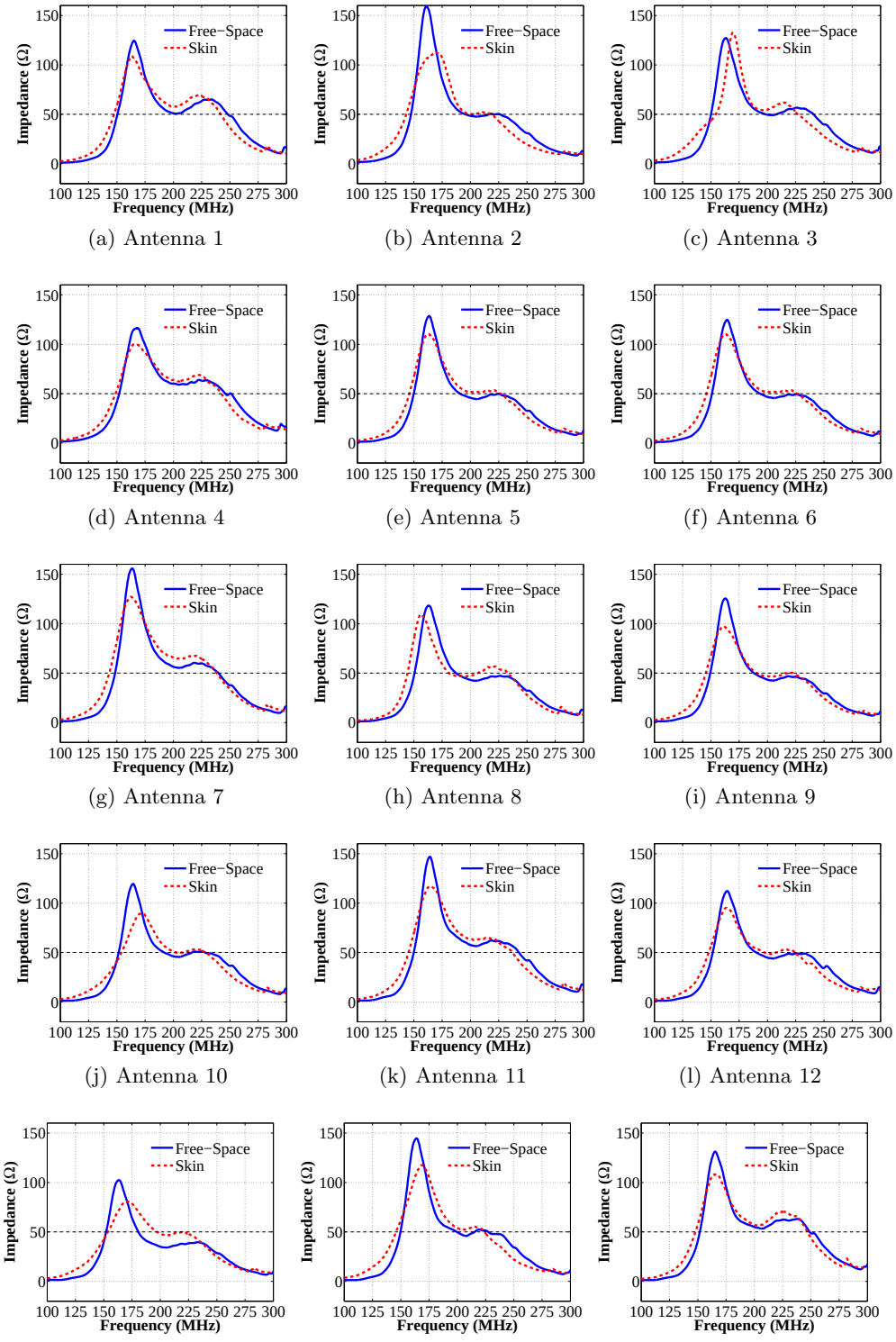

(a) Antenna 1 (b) Antenna 2 (c) Antenna 3

(d) Antenna 4 (e) Antenna 5 (f) Antenna 6

(g) Antenna 7 (h) Antenna 8 (i) Antenna 9

(j) Antenna 10 (k) Antenna 11 (l) Antenna 12

(m) Antenna 13 (n) Antenna 14 (o) Antenna 15

Figure 4.25: Free-Space and Skins Antenna Comparisons for Rev. 2 for the Measured Real Input Impedance

the reactive component of the input impedance and lower the resonant frequency of the antenna [35]. The doublers and glass lowered the impedance of the antenna and decreased the resonant frequency. Therefore, it can be concluded that in general the skins increased the capacitance of the antenna as a combination of the parallel capacitance from the aluminum doublers and from the increased relative permittivity from the glass.

The setup for measuring the antennas glassed to the skins was simulated with HFSS and imported to ADS to integrate the measured balun as discussed in Section 4.2. These results are shown in Figure 4.27. Overall, the measurements and simulations were in good agreement. Antenna 4 was the least matched up with the measurement. The majority of the difference occurred for return losses greater than 20 dB. A 5 dB increase in return loss becomes progressively closer to 0 on a linear scale as the return loss decreases. As the return loss increases, the incremental changes in decibels is progressively smaller on a linear scale. In other words, a 5 dB change in the return loss indicates a greater change in the amount of reflected power at the port when the return loss is 10 dB versus 20 dB. This concept is shown in Table 4.3, where the same incremental change in decibels is converted to a linear scale.

Table 4.3: Return Loss Changes by 5 dB in Linear

Change in Decibels	Change in Linear
10 dB to 15 dB	0.0684
15 dB to 20 dB	0.0216
20 dB to 25 dB	0.0068
25 dB to 30 dB	0.0022
30 dB to 35 dB	6.84e-4
35 dB to 40 dB	2.16e-4
40 dB to 45 dB	6.84e-5
45 dB to 50 dB	2.16e-5

The results in Figure 4.27 validate the models of the antennas with the doublers and skins, and using modeling tools offers capabilities for analysis that are more challenging to implement with measurements. In this case, simulation tools provided the ability to analyze the antenna with only the doublers, which would be inserted into the glass for measurements. Modeling this problem provides insight as to the doubler effects rather than the combined glass and doubler effects as discussed previously. The real component of the input impedance is compared between the free-space in Figure 4.17 and the antenna next to only the doublers in Figure 4.29. These results indicate that the doublers lowered the impedance maximum and increased the impedance of the null

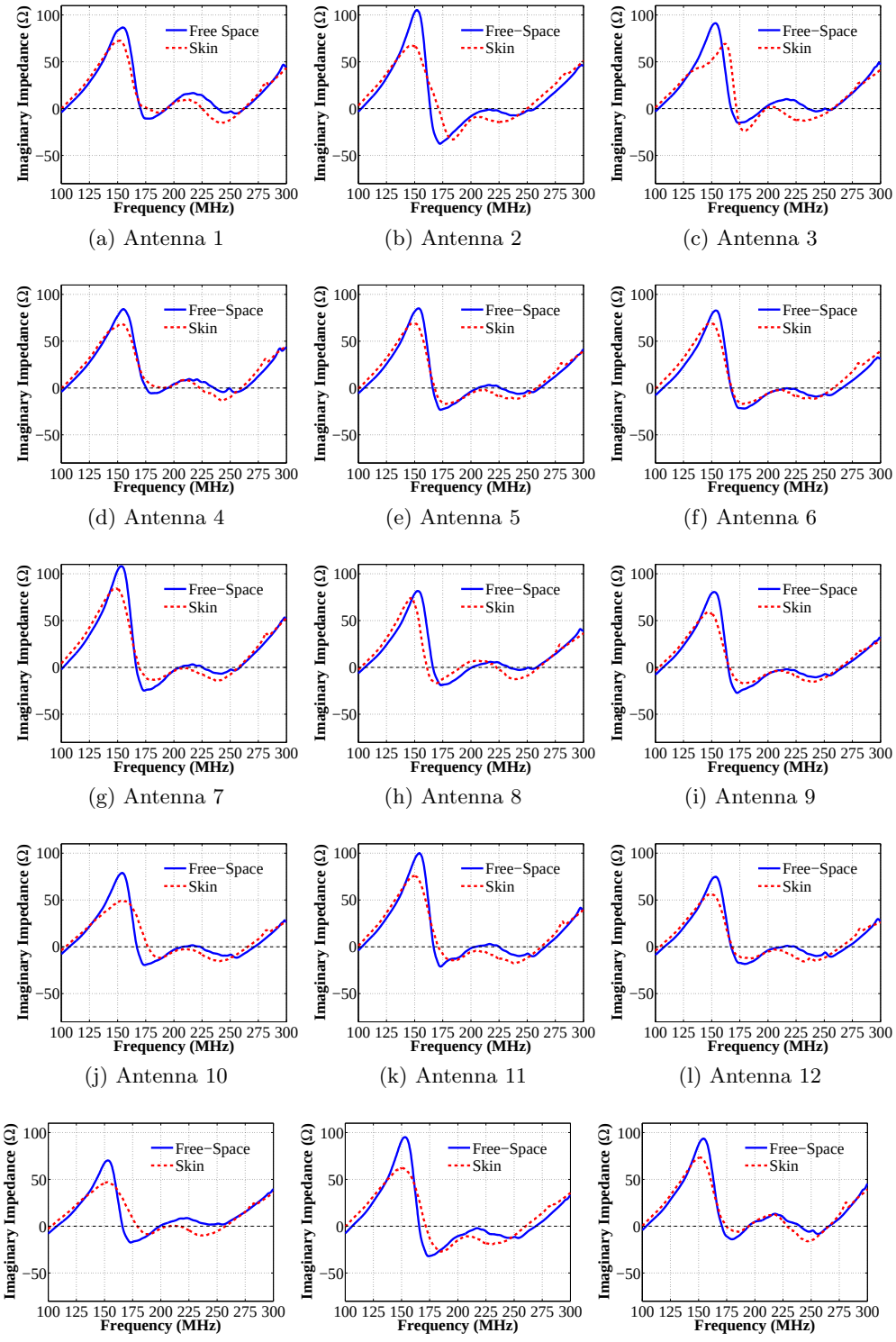

(a) Antenna 1 (b) Antenna 2 (c) Antenna 3

(d) Antenna 4 (e) Antenna 5 (f) Antenna 6

(g) Antenna 7 (h) Antenna 8 (i) Antenna 9

(j) Antenna 10 (k) Antenna 11 (l) Antenna 12

(m) Antenna 13 (n) Antenna 14 (o) Antenna 15

Figure 4.26: Antenna Free-Space and Skins Comparisons for Rev. 2 for the Measured Imaginary Input Impedance

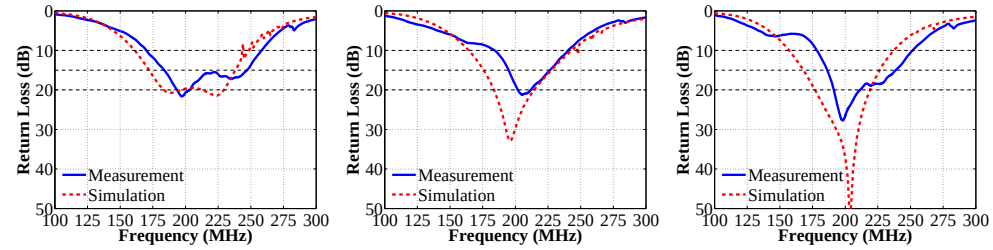

(a) Antenna 1 (b) Antenna 2 (c) Antenna 3

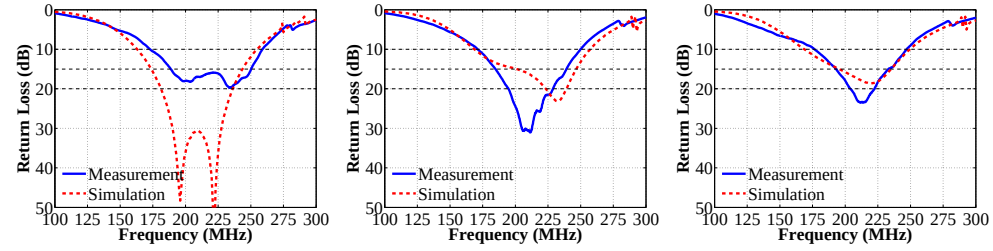

(d) Antenna 4 (e) Antenna 5 (f) Antenna 6

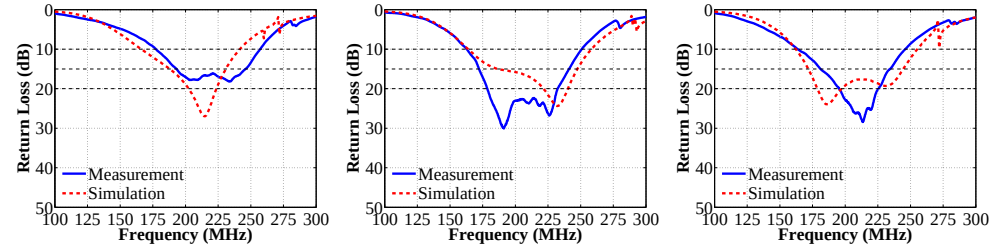

(g) Antenna 7 (h) Antenna 8 (i) Antenna 9

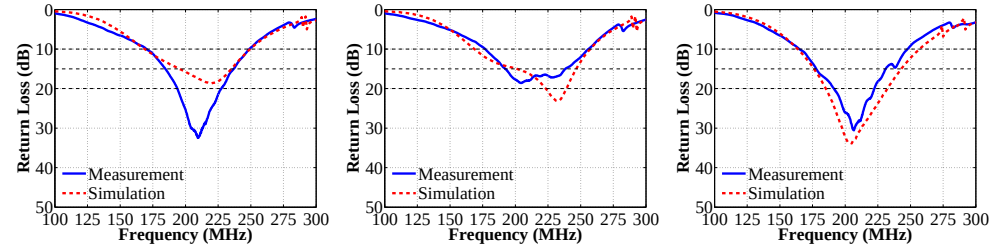

(j) Antenna 10 (k) Antenna 11 (l) Antenna 12

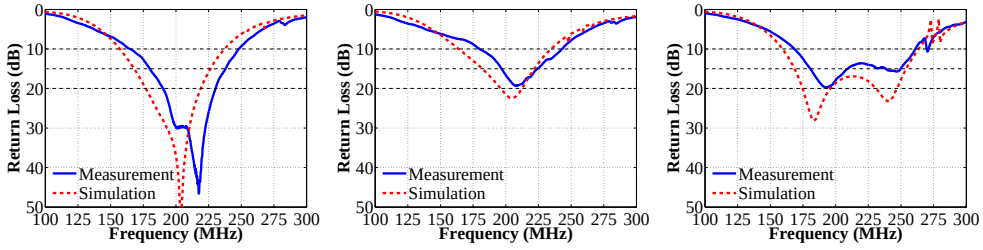

(m) Antenna 13 (n) Antenna 14 (o) Antenna 15

Figure 4.27: Skin Return Loss Measurement and Simulation Comparison for Rev. 2

immediately following the maximum. These results follow the same trend.

Similarly, the imaginary component of the input impedance is shown in Figure 4.30. The imaginary input impedance did not change much for most of the antennas. However, the general trend was a damping effect where each peak was lowered and the null between the two peaks was increased. Antenna four showed a large increase in this null, and the real input impedance had a null around the same frequencies that rose to 50 Ω. Both these effects explain the strong return loss in these frequencies.

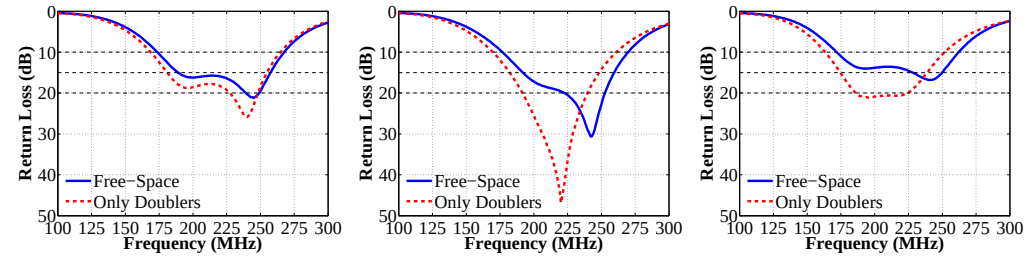

(a) Antenna 1 (b) Antenna 2 (c) Antenna 3

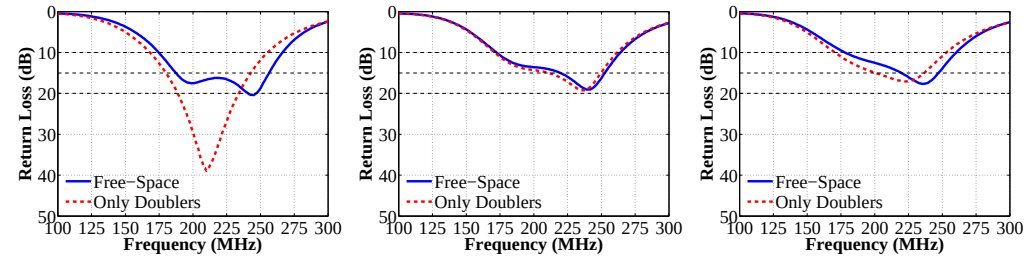

(d) Antenna 4 (e) Antenna 5 (f) Antenna 6

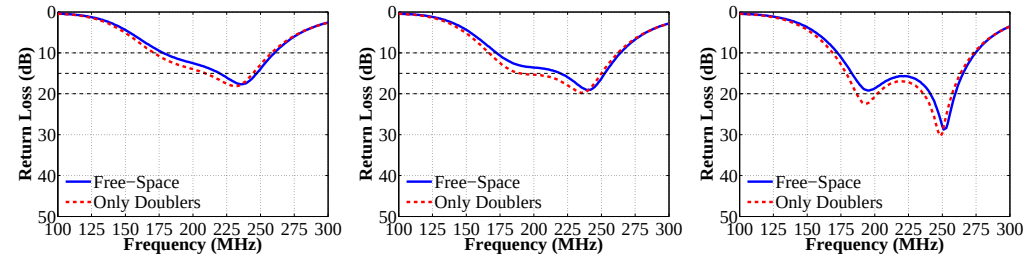

(g) Antenna 7 (h) Antenna 8 (i) Antenna 9

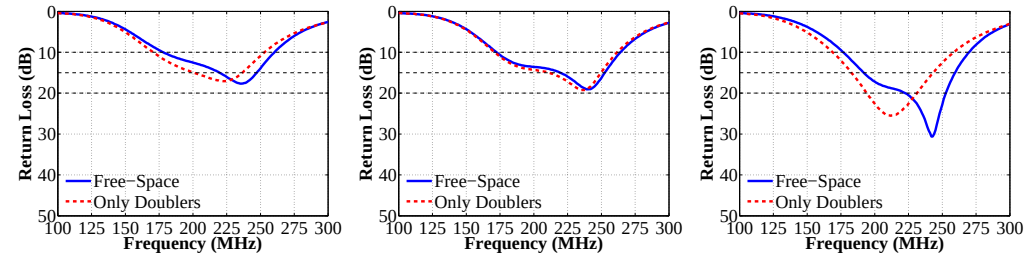

(j) Antenna 10 (k) Antenna 11 (l) Antenna 12

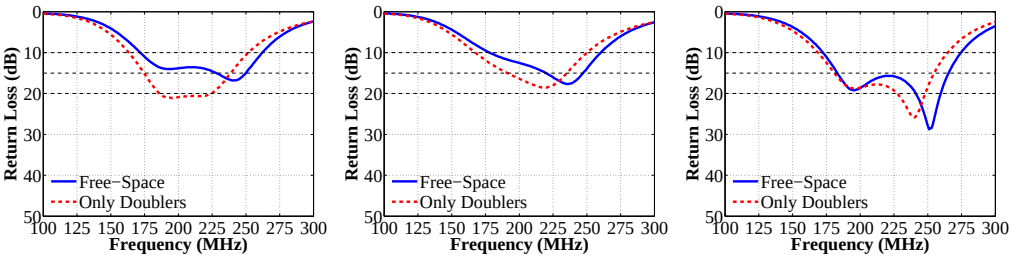

(m) Antenna 13 (n) Antenna 14 (o) Antenna 15

Figure 4.28: Free-Space and Only Doubler Antenna Comparisons for Rev. 2 for the Simulated Return Loss

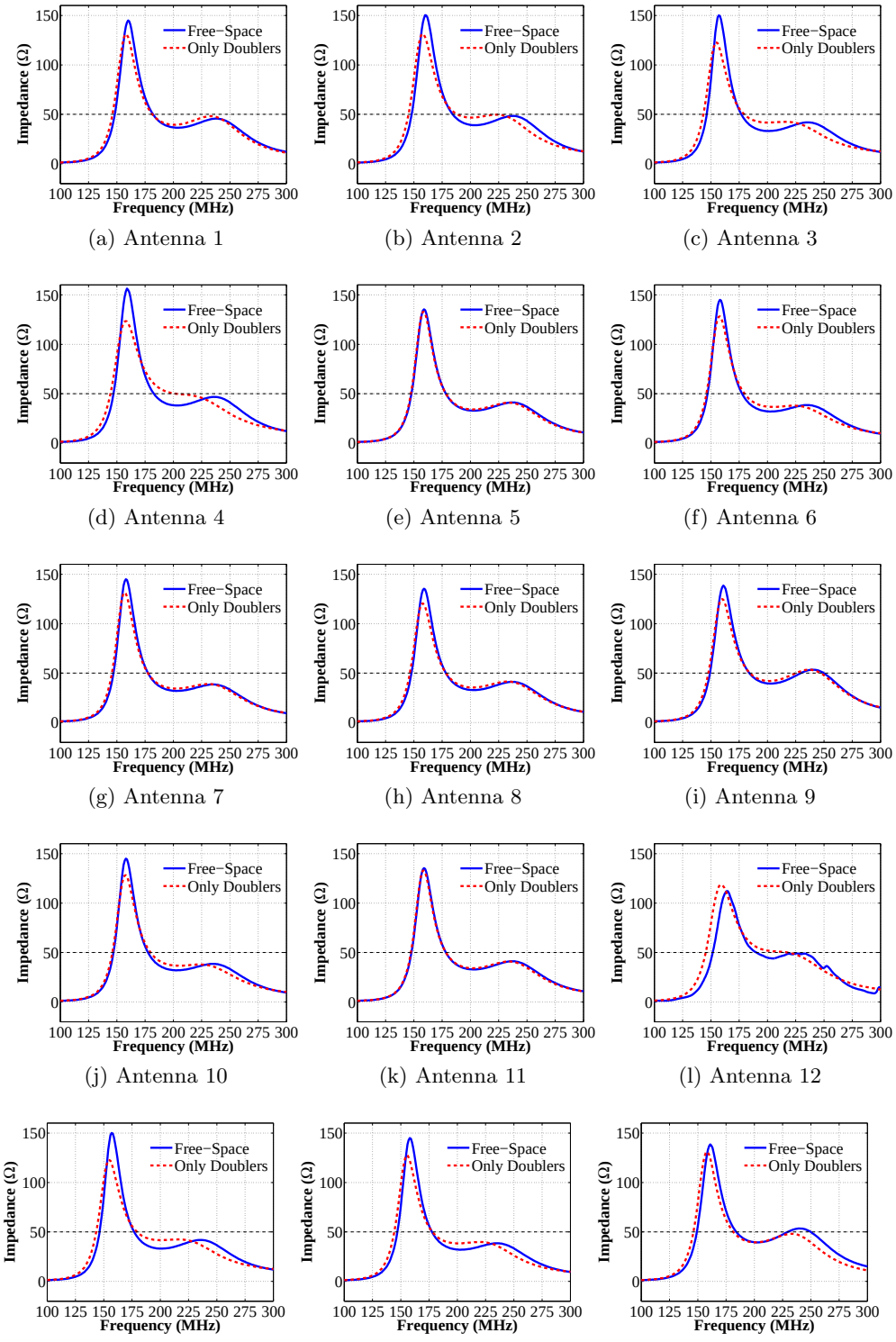

(a) Antenna 1 (b) Antenna 2 (c) Antenna 3

(d) Antenna 4 (e) Antenna 5 (f) Antenna 6

(g) Antenna 7 (h) Antenna 8 (i) Antenna 9

(j) Antenna 10 (k) Antenna 11 (l) Antenna 12

(m) Antenna 13 (n) Antenna 14 (o) Antenna 15

Figure 4.29: Free-Space and Only Doubler Antenna Comparisons for Rev. 2 for the Simulated Real Input Impedance

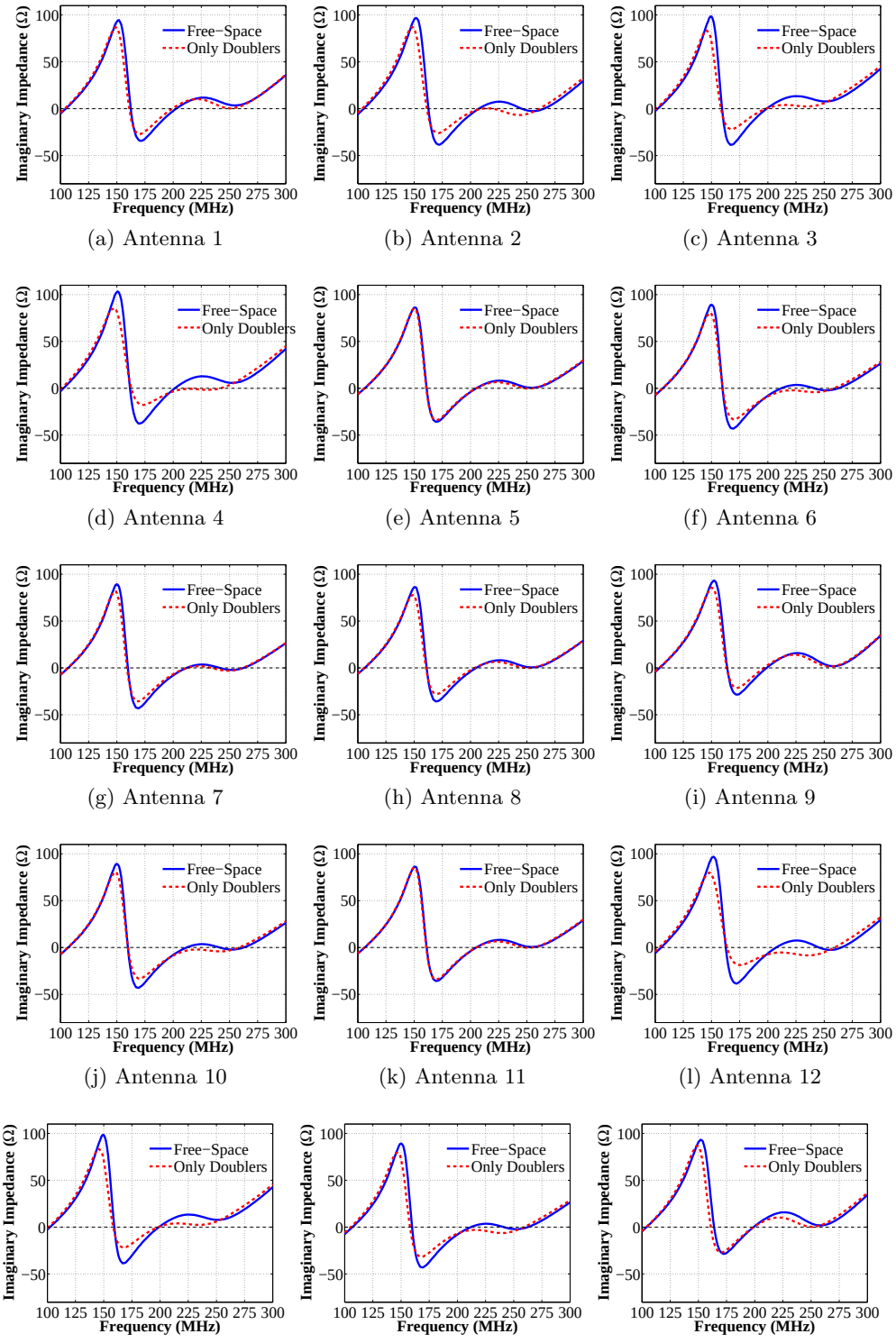

(a) Antenna 1 (b) Antenna 2 (c) Antenna 3

(d) Antenna 4 (e) Antenna 5 (f) Antenna 6

(g) Antenna 7 (h) Antenna 8 (i) Antenna 9

(j) Antenna 10 (k) Antenna 11 (l) Antenna 12

(m) Antenna 13 (n) Antenna 14 (o) Antenna 15

Figure 4.30: Free-Space and Only Doubler Antenna Comparisons for Rev. 2 for the Simulated Imaginary Input Impedance

4.4 Ferrites Along Cables

It is known that currents can be induced on the outer conductor of the feed cable of an antenna that can affect the antenna input impedance and gain. These currents are considered common-mode, because there is not a return current flowing in the opposing direction on a nearby conductor. A ferrite is a practical common-mode choke and acts as a frequency-dependent resistance in series with the common-mode currents [54]. The ferrite controls the impedance of the current as a result of the magnetic flux interaction with the ferrite permeability [11]. The ferrite suppresses the currents from flowing through the magnetic flux.

Several studies have shown the impact of applying ferrites to antenna feed cables [16, 28, 26, 63]. Saario et. al. have studied the effects of adding ferrite beads to the feed cables of monopoles using Finite-Difference Time-Domain (FDTD) modeling. The authors have concluded that the feed cable becomes a part of the antenna and causes a 27° shift in the radiation pattern, lowering the main beam in the horizontal plane [63]. Also, applying a lossless ferrite bead to a cable causes a reflection in the currents flowing on the outer conductor [63]. This change in the radiation pattern can be explained by an asymmetrical dipole where mis-balanced currents are flowing on two sides. In this case, the cable acts as half of the dipole. Since the ferrites cause a reflection, then it is desirable to place ferrites close to the port of the antenna port and limit the length that the current can flow. Similarly, Icheln et. al. have modeled ferrite chokes as a quarter-wavelength "cap" over the coaxial cable to act as a open circuit. The results show similar effects as if a ferrite was placed at the port, but the ferrites absorb more energy and the pattern is slightly more accurate as a reference case [28]. Therefore, it is necessary to note that energy may still be coupled to the cable but absorbed by the ferrite, which will eliminate re-radiation from the cable. Another study has shown the additional ferrites improve the return loss measurements [26]. The ferrite reduces leakage currents from the input port onto the feed cable, which are manifested as ripples on the return loss measurement.

As shown in Chapter 3, the antenna with both the feed cable and the accelerometer cable adversely affected the antenna performance far worse than having only the feed cable attached. The second revision of the P-3 fairing removed the accelerometer cable and added ferrites to the feed cables. Measurement results showing the effect of adding ferrites along the feed cable are in Figure 4.31. The feed cable was elevated 2.5" above the antenna with wood above the first revision antenna 5, which was secured with glass to the skin. Adding the ferrites decreased the affect of the feed cable. There was a diminishing return on adding more ferrites along the cable. The addition of the first

ferrite had the largest effect, and the second ferrite improved the response further. There was a minimal improvement with the addition of a third ferrite. The feed cables for the second revision had ferrites installed along the lengths of the cables. Fair-Rite part number 0443164251 was installed approximately every 4 inches along the lengths of each feed cable, and Fair-Rite part number 0431178281 was installed at the feed on the shorter, pig tail cable (RG-316 DS).

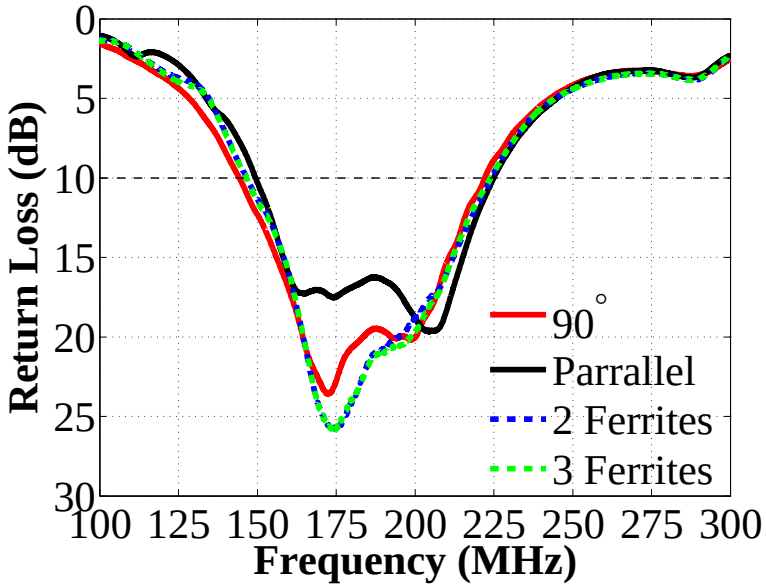

Figure 4.31: Ferrites on the Feed Cable

4.5 Full Assembly

A fully integrated antenna into the fairing features all of the parasitic metallic components, glass components, feed cables and ground plane effects. Therefore, the problem is complex with many variables. Both revisions had test flights with antenna measurements performed in the air. The measurements were done through long cable runs. The complete cable specs for revision 2 are included in Appendix B. Time-gating was applied to remove reflections caused by the long cables, and cable attenuation was removed from the return loss as described in Appendix C. The measured antenna performance without time-gating and the time-domain, range bins also can be found in Appendix C. As shown in Figure 4.32, each antenna showed improvements from the previous revision, except for antennas 7 and 8.

The measurement for the revision one was narrow bandwidth that did not include the full operational bandwidth of the antennas. Therefore, no assumptions were made

as to the antenna performance outside the measured bandwidth. If the return loss was even as far as 20 dB at either 160 or 230 MHz, then this was considered the lowest or highest operating frequency. This reduction should be kept in mind for the following average improvements. The average 10 dB bandwidth improvement was 18 MHz. Similarly the improvement for the average 15 dB bandwidth was 26.5 MHz. Finally the improvement for the average 20 dB bandwidth was 12.8 MHz between the revisions. Some of the resonances do include the target center frequency of 195 MHz, so these were removed from the following average calculations. The average bandwidth improved for a 15 dB return loss is 26.4 MHz, and the 20 dB bandwidth improved 11.65 MHz. These improvements exclude any increase in bandwidth when the bandwidth does not include 195 MHz.

Figure 4.33 shows the fully installed antennas compared with the results for the same antennas glassed onto the skins as reported in 4.3. In most cases, the installed antennas performed worse than the skins, but there are exceptions such as antennas 2, 9 and 14. Antennas 2 and 14 are symmetric, so the doublers are the same. Also, antenna 9 is symmetric with antenna 7, which had results that were much different. Antennas 1, 3, 4, 5, 6, 10, 12 and 15 did not shift or change much between being glassed on the skin and installed in the fairings. While the exact cable contributions to the antennas inside the fairings are still ambiguous, the results seem to indicate that the feed cables for the surrounding antennas running parallel did not seem to shift the antennas as dramatically as shown in Figure 3.38 with two cables running parallel to the antenna. The cables do not appear to be the cause for the degradation in antenna 7, which suffered a shift in resonant frequency and lowering of its return loss across the lower frequencies. The cable effects appear to be sharper with multiple resonances.

Simulations using HFSS were performed including the skins, doublers, gang channels, ribs, pylons and ground plane. The comparison between measurements and simulations are shown in Figure 4.34. As the complexity of the problem increased, the agreement between simulation and measurements decreased. Many antennas still showed strong agreement such as antennas 1, 2, 3, 5, 6, 10, 11, 12, 13, 14 and 15. Others such as 4, 7, 8, and 9 had many of the same features but with stronger resonances that appeared in one but not the other.

Converting the return loss to the real and imaginary components was not practical with measurements taken using long cables. This is exasperated with the time-gating, which improves the representation of the return loss in decibels but removes data. However, it is still desirable to inspect the differences in the input impedances between the skin and the fully installed antennas. Since there is good agreement for the majority of the simulations, inspecting the input impedance through simulations provides another

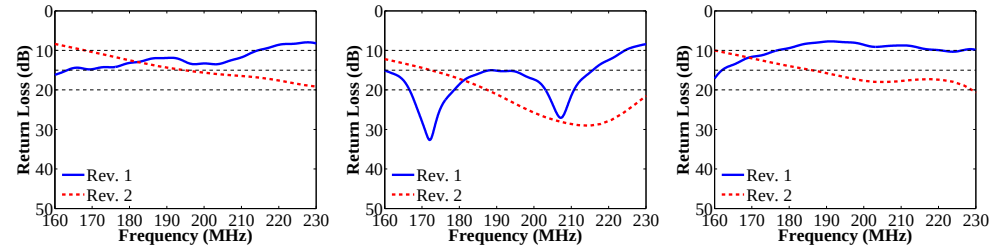

(a) Antenna 1 (b) Antenna 2 (c) Antenna 3

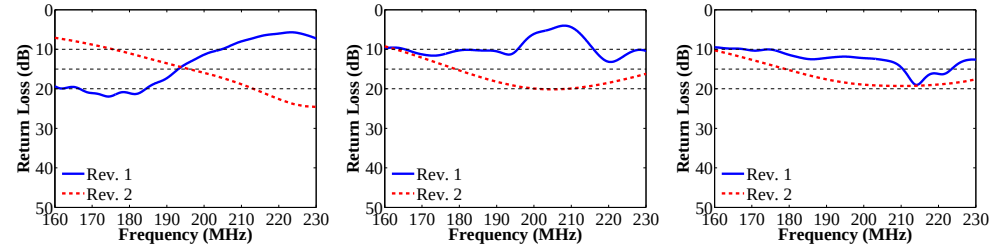

(d) Antenna 4 (e) Antenna 5 (f) Antenna 6

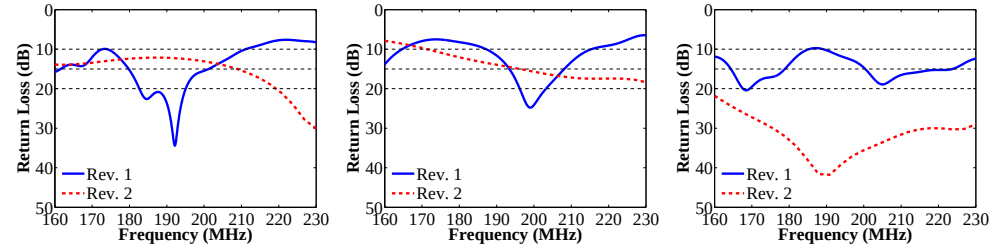

(g) Antenna 7 (h) Antenna 8 (i) Antenna 9

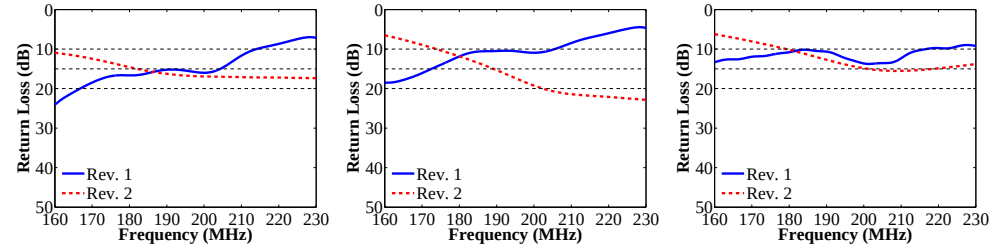

(j) Antenna 10 (k) Antenna 11 (l) Antenna 12

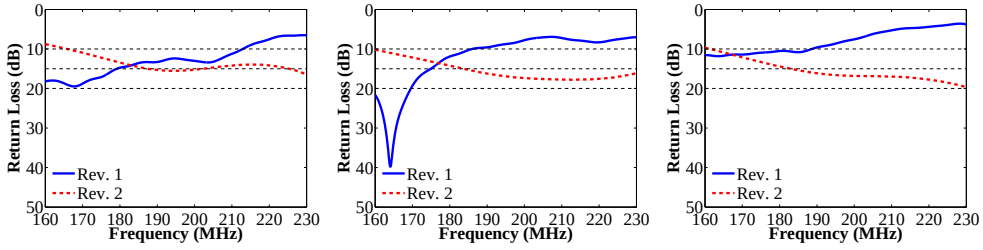

(m) Antenna 13 (n) Antenna 14 (o) Antenna 15

Figure 4.32: Installed Return Loss Measurement Comparisons between Rev. 1 and Rev. 2

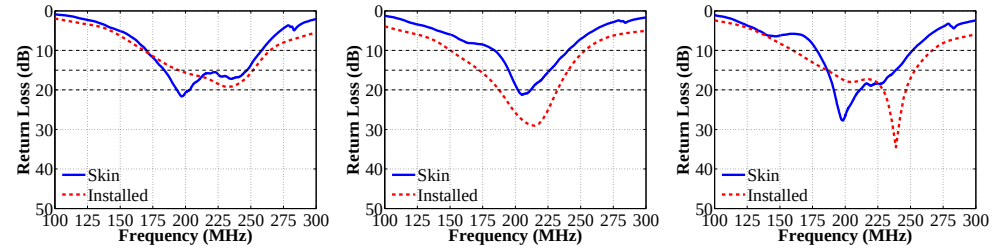

(a) Antenna 1 (b) Antenna 2 (c) Antenna 3

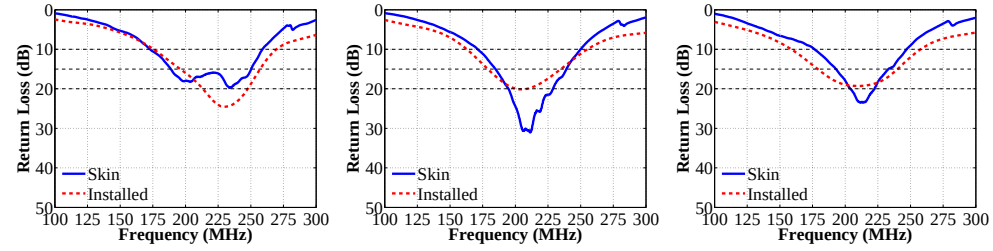

(d) Antenna 4 (e) Antenna 5 (f) Antenna 6

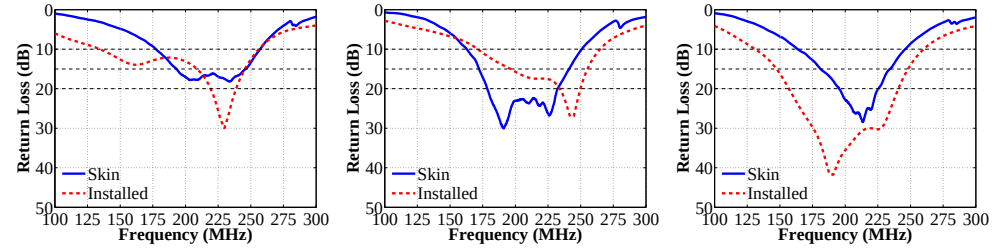

(g) Antenna 7 (h) Antenna 8 (i) Antenna 9

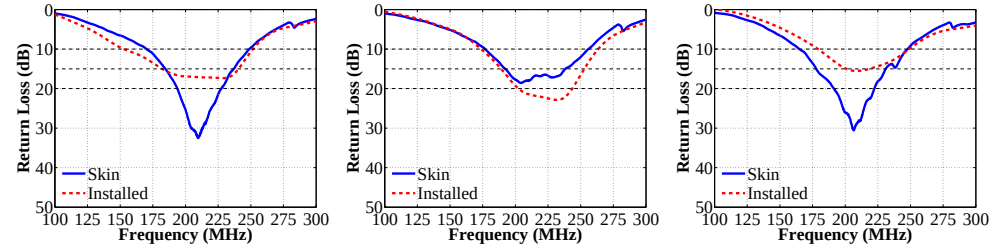

(j) Antenna 10 (k) Antenna 11 (l) Antenna 12

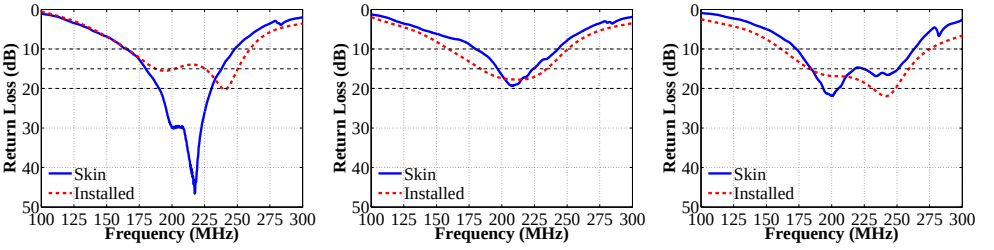

(m) Antenna 13 (n) Antenna 14 (o) Antenna 15

Figure 4.33: Skin and Installed Return Loss Measurement Comparison for Rev. 2

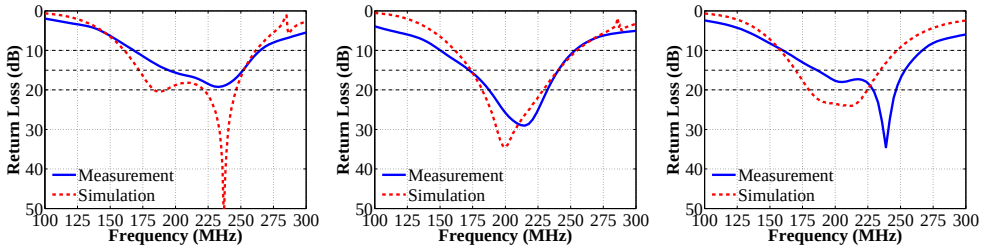

(a) Antenna 1

(b) Antenna 2

(c) Antenna 3

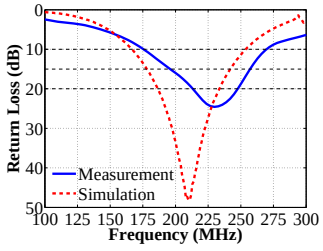

(d) Antenna 4

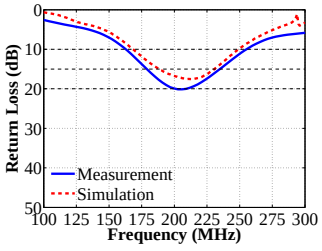

(e) Antenna 5

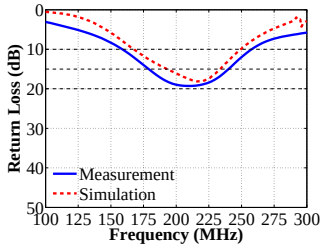

(f) Antenna 6

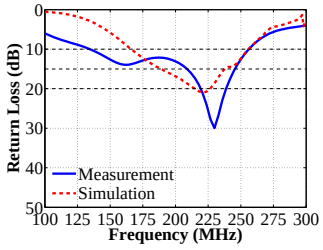

(g) Antenna 7

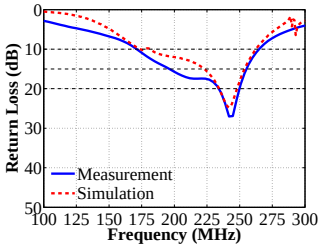

(h) Antenna 8

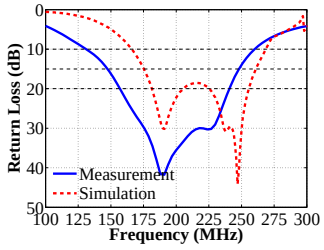

(i) Antenna 9

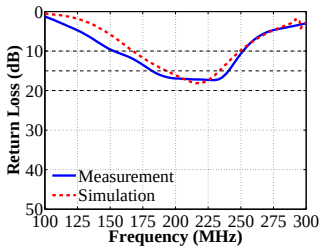

(j) Antenna 10

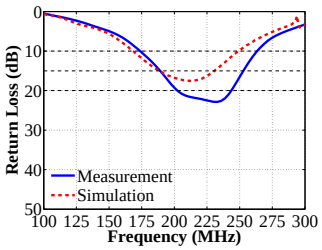

(k) Antenna 11

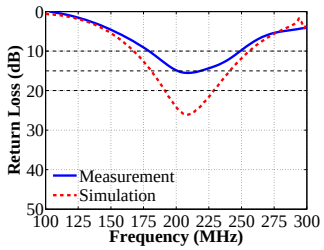

(l) Antenna 12

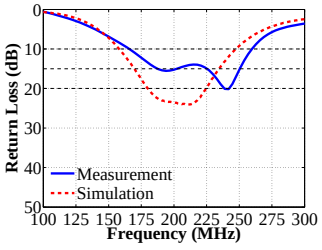

(m) Antenna 13

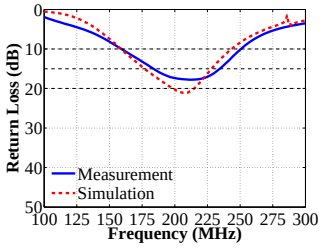

(n) Antenna 14

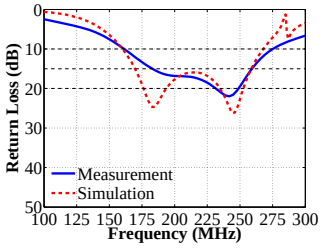

(o) Antenna 15

Figure 4.34: Installed Return Loss Measurement and Simulation Comparison for Rev. 2

tool for performance analysis. The simulated antennas least like the measurements are considered to provide less insight. The real part of the input impedance representations for the simulated antennas on skins and installed is shown in Figure 4.35. First, the antennas 1, 2, 3, 6, 10, 12, 13, 14 and 15, which had the best agreement with measurements are evaluated. Antenna 1-3, 10, 13 and 14 featured a decrease in the input impedance overall with some variations such as a slight increase at the null in antennas 2 and 14. As seen with the doublers, the strips of metal cause a decrease in the impedance. The gang channels were not in the skin measurements but cause a similar influence on the antenna input impedance as the doublers. Although the results do not agree as well with measurements, antennas 7 and 9 indicate a lowering of the spike with a shift toward higher frequencies. The second maximum is also decreased. These may be caused by the gang channels as well.

Similar results for the imaginary component of the input impedance is shown in Figure 4.36. Antennas 1, 2, 3, 5, 11, 13, 14 and 15 showed decreases in the capacitance around the two nulls bringing the reactive component of the input impedance at these frequencies closer to 0 Ω. Antenna 12 showed a slight increase in capacitance. The decrease in capacitance and shifting to the higher frequencies is not explained by the presence of the conductive parasitic features such as the ribs and the pylons.

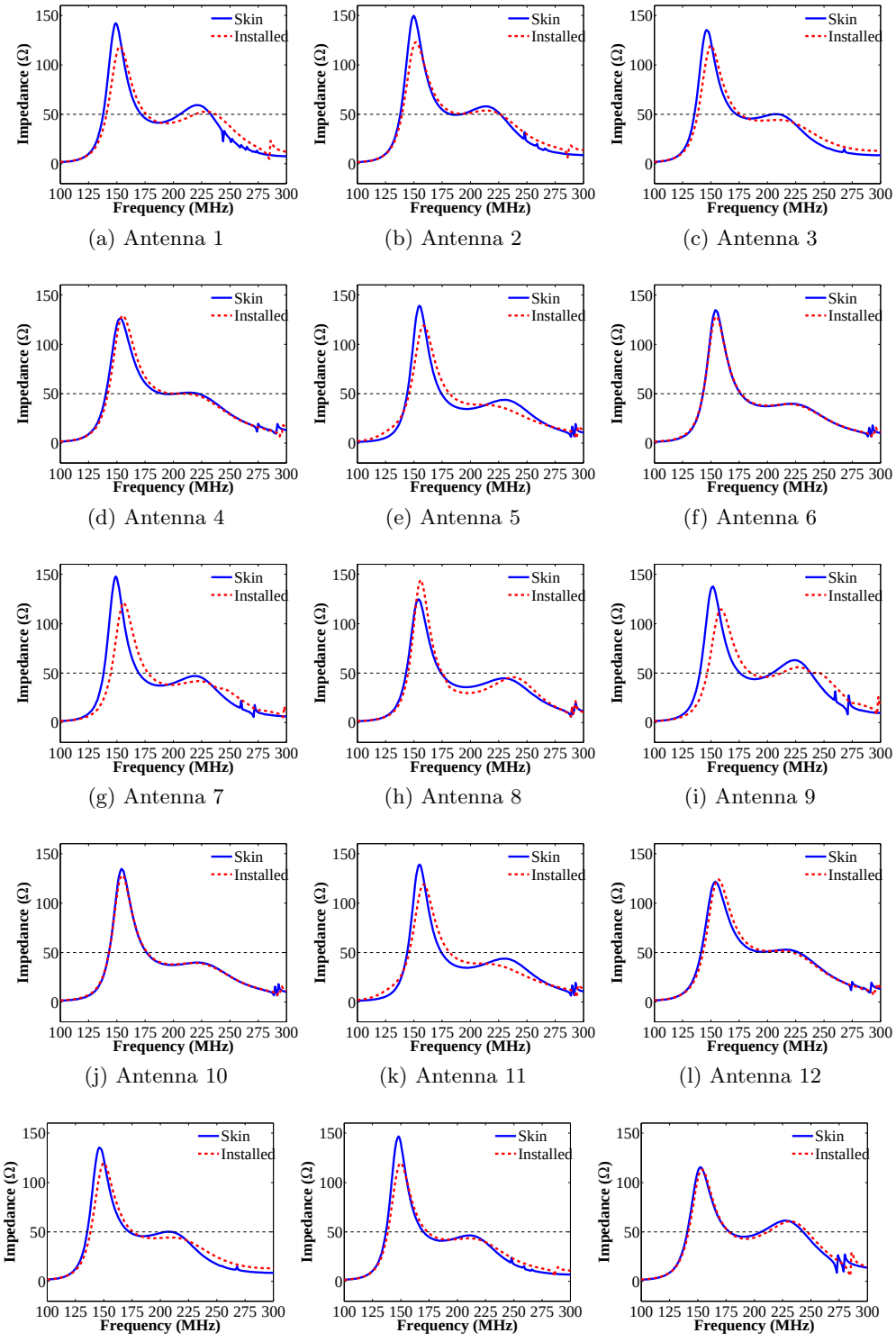

(a) Antenna 1 (b) Antenna 2 (c) Antenna 3

(d) Antenna 4 (e) Antenna 5 (f) Antenna 6

(g) Antenna 7 (h) Antenna 8 (i) Antenna 9

(j) Antenna 10 (k) Antenna 11 (l) Antenna 12

(m) Antenna 13 (n) Antenna 14 (o) Antenna 15

Figure 4.35: Skin and Installed Real Input Impedance Simulation Comparison for Rev. 2

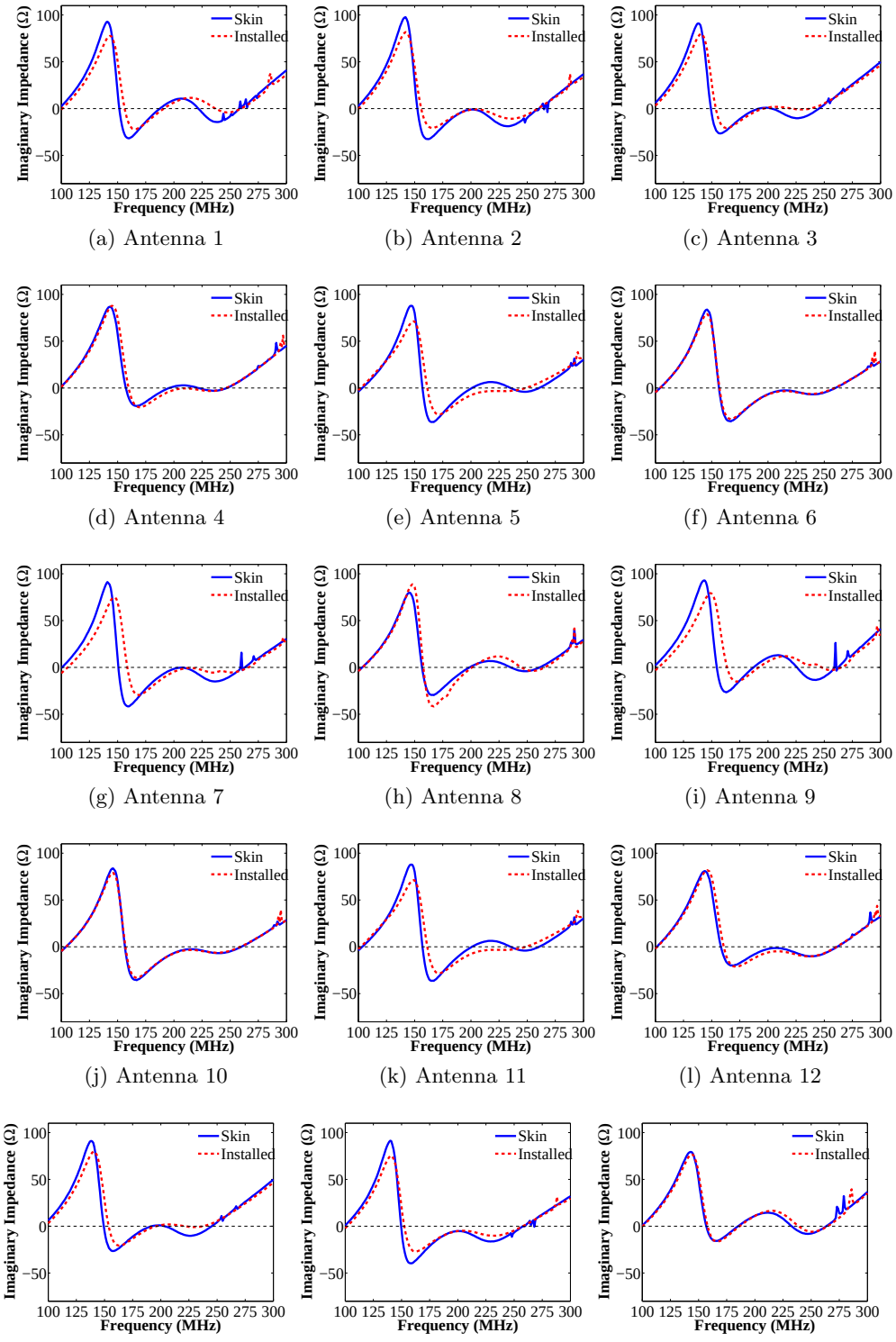

(a) Antenna 1 (b) Antenna 2 (c) Antenna 3

(d) Antenna 4 (e) Antenna 5 (f) Antenna 6

(g) Antenna 7 (h) Antenna 8 (i) Antenna 9

(j) Antenna 10 (k) Antenna 11 (l) Antenna 12

(m) Antenna 13 (n) Antenna 14 (o) Antenna 15

Figure 4.36: Skin and Installed Imaginary Input Impedance Simulation Comparison for Rev. 2

4.5.1 Simulated Radiation Patterns

Up to this point, results have been based on return loss and bandwidth. However, analysis of antennas requires a radiation pattern as well. This particular array design has metallic objects near the antennas that can off balance the current distribution and cause a shift or squint in the radiation pattern [8]. These near-field, parasitic elements can be any of the metallic features discussed previously, which have their impact on the input impedance as has been discussed. Furthermore, the inboard array has an irregular ground plane with a receded section below the center antenna. First, this discussion will consider the parasitic, structural components in close proximity to the antenna, and their effects on the radiation pattern. Then, a discussion on the unequal ground plane and its effect on the gain of the array elements will be discussed.

Parasitic elements the same length as the antenna have been shown to cause more ripples in the beam patterns when there was a large spacing between the antenna and the parasitic element. On the other hand, the beam pattern is less affected with the same length parasitic element at a smaller spacing (0.2λ) [2]. The P-3 array consists of multiple smaller parasitic elements in close proximity to the antenna of varying length and position from one antenna to another. A few of the co-polarized, E-Plane patterns are shown in Figure 4.37. Over the frequency range the E-plane keeps consistent patterns with some higher side lobes in antennas 7 and 9 due to the displaced ground plane, which causes a discontinuity in the ground plane off to the side. More individual antenna element's radiation patterns are presented in Appendix D.

The inboard array was spaced irregularly from the ground plane due to an aircraft antenna port consisting of an ADF and a marker beacon. The configuration for this receded ground plane is shown in Figure 4.38. The distance from antenna 8 to the ground plane was 61 cm (0.3965λ at 195 MHz) while the other elements were around 34.5 cm (0.224λ at 195 MHz) away from the ground plane. The ground plane was 27.9 cm below the fiber glass radome (0.181λ at 195 MHz). This was a considerable difference in the ground plane separation.

An antenna operating in close proximity to a ground plane can be explained with image theory and array theory. First, image theory is used to simplify the representation of the geometry. Image theory states that an equivalent geometry is created for a source in close proximity to a ground plane by removing the ground plane and creating a source of equal magnitude but opposite phase [72]. An antenna with a distance d from the ground plane has the equivalent antenna spaced 2d between the source antenna and the equivalent antenna. Therefore, the representation of an antenna close to a ground plane is equivalent an array consisting of two elements for the antenna side of the ground

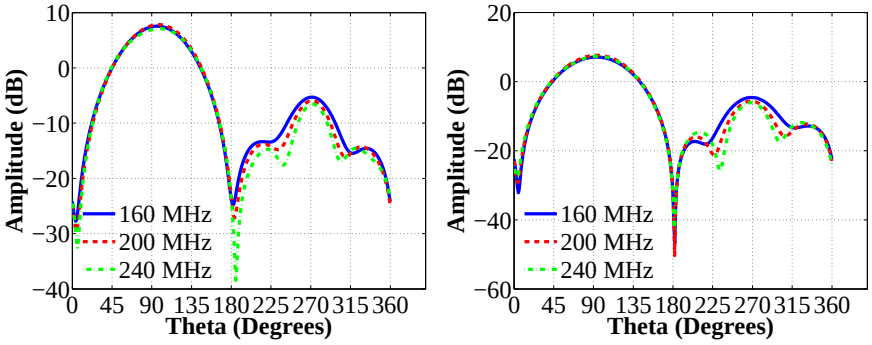

(a) Antennas 5 and 11

(b) Antennas 6 and 10

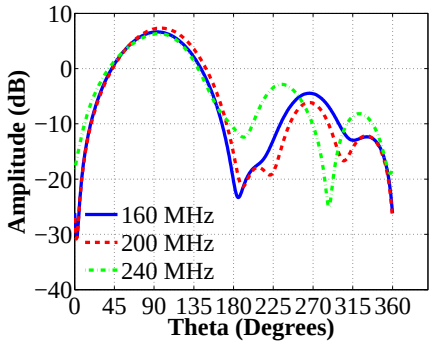

(c) Antennas 7 and 9

Figure 4.37: Rev. 2 Installed Inboard Antenna Simulated E-Plane Radiation Pattern

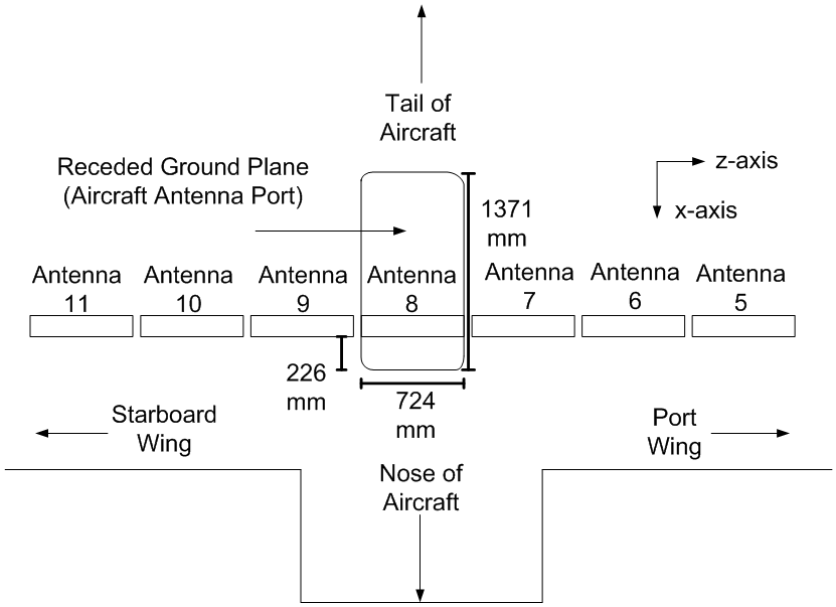

(a) Top View

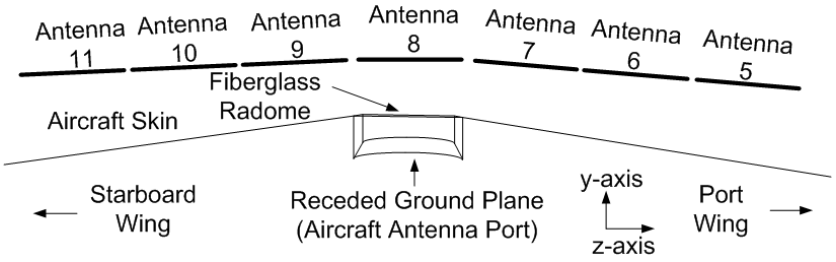

(b) Side View

Figure 4.38: Inboard Array with Unequal Ground Plane

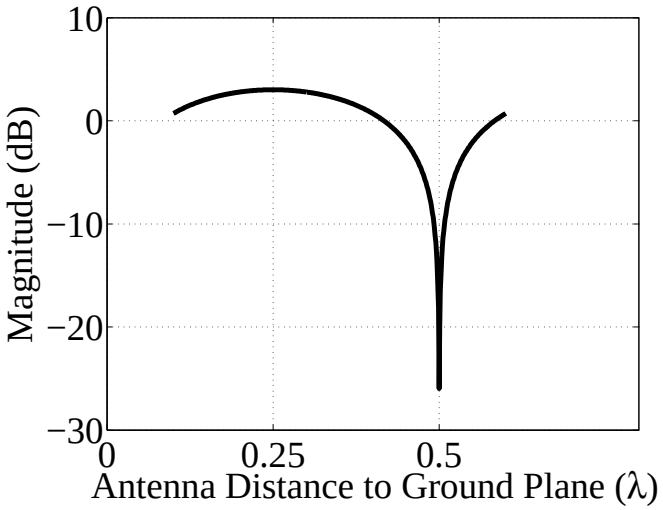

Figure 4.39: Antenna Factor for Varying Distance to Ground Plane

plane. Therefore the array factor equation can be written as Equation (4.5) for a single element above a ground plane at a distance d [72].

$$\text{Array} \quad \text{Factor} = 2j\sin(kd\cos(\theta)) \tag{4.5}$$

The antenna factor is a function of both the distance from the ground plane and the angle. A plot showing the array factor change as a function of distance with a constant angle, which is directly away from the center antenna or nadir, is shown in Figure 4.39. This plot shows a maximum occurring when the ground plane distance was $\lambda/4$ and a deep null occurring at $\lambda/2$. Therefore, it is ideal to keep the distance to the ground plane as close as possible to $\lambda/4$. Since the distances from the ground plane are about 0.25λ and 0.40λ, these values were used to compare the theoretical loss in the antenna gain. The value calculated using array theory is 3.1 dB.

The mutual coupling as mentioned in Section 2.2.1 may affect the sidelobes. Simulations were completed to compare the effects of mutual coupling on the array pattern. Removing the mutual coupling from the simulations requires some simplifications, so two cases are used to show the pattern without any present. The first case is the array factor that does not consider the element pattern, but reduces the elements to isotropic point sources [72]. The array factor does not take into account the angles of the bow-ties along the array. As can be shown from Figure 4.38b, the inboard array has three elements on both sides of the center antenna directed at angles. This is better represented in Figure 4.41. Therefore, the array factor removes the mutual coupling, but does not consider the effect on the radiation pattern from the elements.

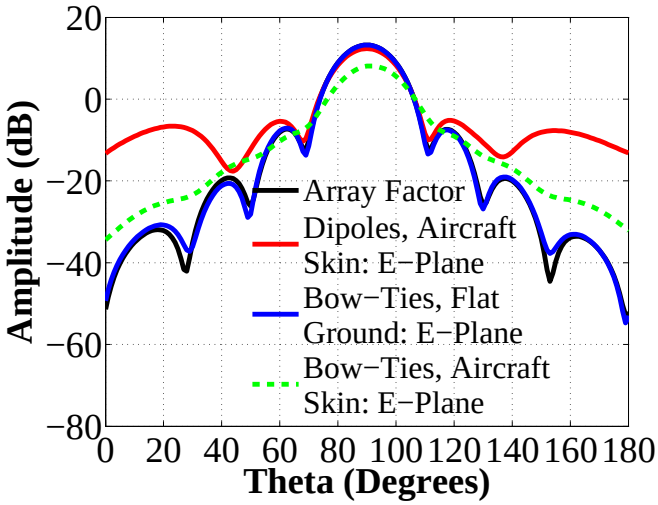

Figure 4.40: Radiation Pattern Comparing Mutual Coupling Affect on Sidelobes

The next simulation was drive to eliminate the effects of the mutual coupling was completed with thin dipoles, which have less mutual coupling than the bow-ties. The thin dipoles do not remove the effects of mutual coupling completely from the simulation, but reduce the simulation time and limit the mutual coupling. The peak mutual coupling level is -10 dB. This simulation was completed using the aircraft skin to consider the effects due to the irregular ground plane.

Next, the bow-ties were simulated using a finite but flat ground plane. While this does not reduce the mutual coupling, this removes the effects due to the skin. The final completed simulation included the revision two dipoles and the the skin of the aircraft. All of these results are compared in Figure 4.40.

The inboard array is not perfectly collinear, because the antennas have a separation along both the z- and x-axes as noted in Figure 4.39. These are shown in more detail in Figure 4.41, and the distances are from center-to-center. The dz1 is 77.2 cm (0.5λ at 195 MHz). The dz2 is 74.0 cm (0.48λ at 195 MHz) The dx1 is 2.6 cm (0.02λ at 195 MHz), and the dx2 is 4.6 cm (0.03λ at 195 MHz). This provided motivation to add phase matching cables to the inboard array to line up with the center element. These cables are described in more detail in Appendix B. The cable affected the radiation pattern by adding a phase shift. Simulation results showing the improvement for the array factor is shown in Figure 4.42. This showed the side lobes decrease in amplitude and separate from the main beam. Another configuration is shown for contrast where the dx between the antennas is 0.1 meter or (0.065λ) between the elements. This case showed an improvement, but the side lobes increased beyond the first side lobe. Therefore,

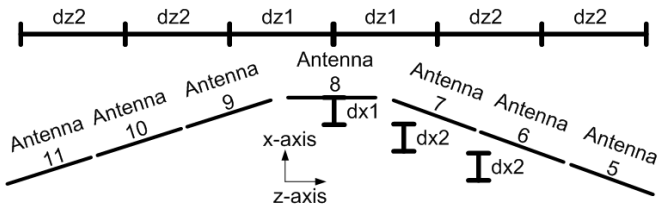

Figure 4.41: Geometry of Inboard Antenna Separations

the array cannot be made in any configuration without consequences. However, a small separation in the antenna distances can be compensated with a phase shift implemented using cables.

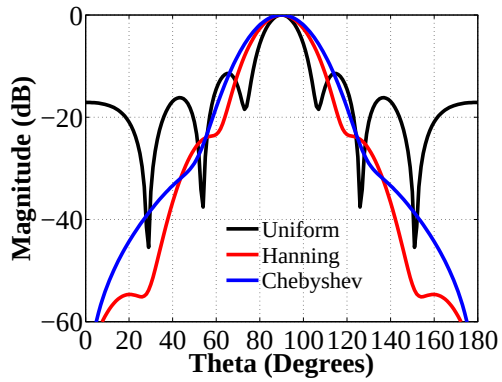

(a) Without Phase Adjustment Cables

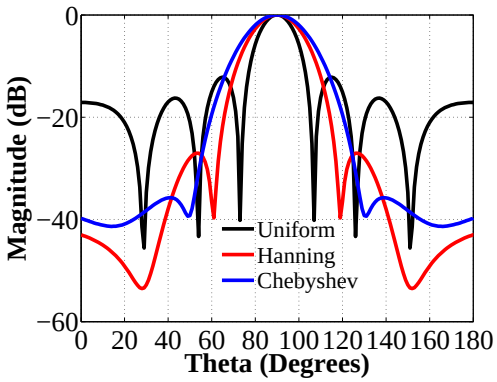

(b) With Phase Adjustment Cables

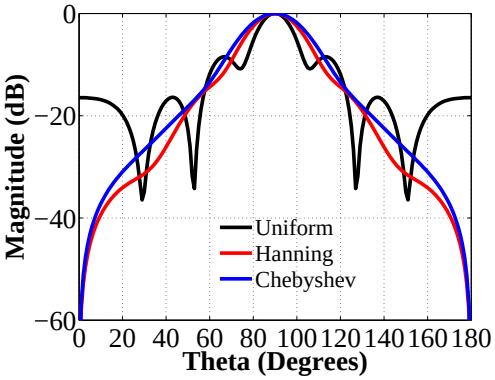

(c) Exaggerated dx

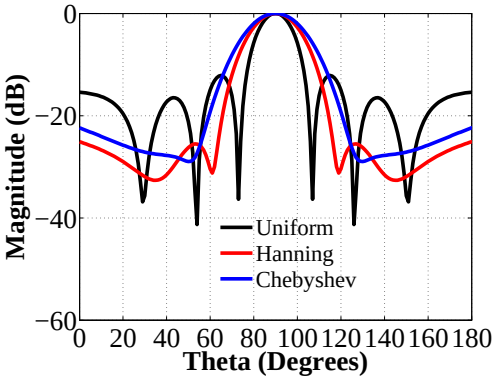

(d) Exaggerated dx with Phase Adjustment Cables

Figure 4.42: Inboard Array Factor

Chapter 5

Conclusions

A bow-tie antenna array was deployed on the NASA P-3 aircraft with a 41% bandwidth for 15 antenna elements. Furthermore, simulations and measurements agree well for the antennas mounted to the skins, and the antennas at this stage of integration were improved from the first revision. Conductors in close proximity to the antennas altered the current distributions, limited bandwidth and reduced the antenna return loss. Antenna design and adaptations to the structure improved the antenna performance. Several simulations agreed well for the full installation, but there were a few elements that the simulations did not predict the measured performance due to the complexity of the structure. In general, the bandwidth and the magnitude of the return loss improved from the first to the second revision.

The success in widening the bandwidth was accompanied with novel design techniques. The three fairings represent a large structure mounted on a NASA aircraft, which required investigation and analysis with the proper design changes to successfully integrate antennas into a complex structure. The increase in the antenna return loss throughout the bandwidth improves the radar performance from revision one to revision two and from the original design. The expansion of the antenna bandwidth will allow the depth sounding and imaging radar to improve its resolution, and present the possibility for expanding its capability to perform sea ice and permafrost measurements.

Several components of this analysis and design are unique to this project. The metallic objects surrounding the antennas imposed unique constraints on the design. Parallel conductors had parasitic effects on the antennas, which could detune the antennas or, through proper design, enhance the input match and widen the bandwidth as with the sleeve dipole [36]. The design manufactured for the second revision minimized the negative effects of these conductors, maintaining the return loss at the higher frequencies. In addition, the magnitude of the return loss at resonance did not

dramatically decrease. The individual antenna measurements were not performed in revision one as extensively as the second revision, so a direct comparison is difficult at this stage of the integration with the fairing. However, there was a minimal decrease in the return loss after integration with the antennas due to both the effects of the doublers and the dielectric loading of the S2-Glass.

A novel contribution was the reduction of the mutual coupling through the spiked back edge of the bow-tie antennas. This was done through a few different iterations of limiting currents along the back edge of the bow-tie, which was implemented with spikes rather than a straight edge. The final design had five spikes to reduce the mutual coupling but maintain antenna bandwidth.

Next, the balun designed for this radar system operates for high power applications while similar commercially available baluns operate only for low current. This balun does require more optimization to improve the upper frequencies through further study of the parasitic effects between windings.

Recommended Future Work

A few elements had a shifted resonance that would ideally occur at 195 MHz, so some modifications remain possible to improve upon the second revision. Furthermore, a few simulations do not completely agree with the measurements, so understanding the difference or the details lacking in the simulations will enable better analysis and insight to the issues. Below is a list of some of the possible improvements and focus areas for improvement upon this system.

1. The gain for antenna 8 is shown in Appendix D, but this gain is the same as other antenna elements. Initial field measurements in the field showed that the gain was 3 dB less than other antenna elements, which was explained using image theory in Section 4.5.1. Simulations should show this same change in gain. The presence of the cross beams inside the inboard port may act as a ground plane. However, these may be modeled incorrectly due to approximations in the geometry. Furthermore, improvement of simulations may done by adjusting the size of the ground planes within the simulations. Simulations have a finite sized ground plane in order to emulate the skin of the aircraft. This ground plane should not touch the PML layer as this may cause errors in producing correct radiation patterns.
2. Antennas 7 and 8 had the worst performance across the installed bandwidth, and there is potential for future optimization. Replacing the balun could potentially improve the response in the structure.

3. Better agreement from the measurements and the simulations are necessary to make additional improvements and fully validate the simulations. Measurements were not properly done on all the baluns with the test jig, and applying the appropriate S-parameters would be more accurate, even though the baluns performed similarly.

4. Another area for improvement and better understanding is the performance within the fairing. Testing of the antennas while inside the fairing and changing the layout of the cables may offer more insight into the variations from the simulations and the measurements.

5. Antenna 9 performed well when integrated with the fairing. This is a desirable result, but complete understanding for this reason would enable improvements to other antennas. Cables may be coupling currents from the antennas and impacting the performance even with the ferrites reducing the common-mode current on the outer conductor. Investigation the feed cable next to the antenna within the fairing may offer insight as to its performance. Testing the antenna with and without ferrites on the feed cable may indicate the reason for the improved input match and minimization of coupling. These two differences are the largest differences from antenna 7 and antenna 9, due to the symmetry of the array.

6. Qu and Ruan have shown that bow-tie antennas with rounded corners can have improved return loss performance [57]. Further investigation into rounding the corners on the bow-tie antenna may improve the return loss characteristics while not affecting the mutual coupling.

7. Securing ferrite balun wires may reduce the impact of long term damage due to vibration on the coating around the conductors. One solution is an encapsulate material that serves to fix the wires in place. An encapsulate may be a foam material. If failure occurs, an electrical short may disrupt the performance. In order to secure the balun wires, attention to the dielectric properties, rigidity of the encapsulate, and coefficient of thermal expansion may need to be considered. The dielectric properties may cause the signals on the magnet wire to travel at different speeds resulting in an unbalance on the output of the balun. The rigidity of the encapsulate may cause stresses on the balun wires at the joints. The baluns will be outside and can experience extreme temperature changes from the flights to the summer storage. A rigid encapsulate with a large coefficient of thermal expansion mismatch between the wires and ferrite may cause cracking and failure in the long term. The application of this material must be capable of being inserted into the binocular core and curing within a reasonable time and temperature. The

curing temperature cannot exceed the Curie temperature of the ferrite.

8. The current carrying capacity for 20 AWG wire is 11 Amps, but this value is for continuous current [55]. The power capability of the balun is determined by both the binocular core and the twisted-pair, so testing is the best method to evaluate the maximum current and power capabilities of the balun. This will be required for using the balun for higher transmit power.
9. A few different compounds were investigated for securing the balun wires inside the ferrite core. However, each of these impacted the balun performance, even when considering the relative permittivity of the material. Another possibility could be to try a coated wire such that vibrations and continued stress does not eventually cause a short to occur.
10. Although the balun may be glassed to the skin, care must be taken to securing the balun to the antenna prior to the the glassing process. This was done with a Silicone RTV for this project to discourage sliding of the balun from vibration. Better application of this process should be applied before the balun is attached to the antenna. This will allow the bond to be inserted underneath the balun as best as possible. Selection of this bond should be done for possible future removal but with added securing. Double-sided tape may be used, which will also add a cushion. Tapes may lose adhesive with use in the long-term.
11. During the manufacturing stage, the antennas are placed under vacuum for a thin layer of glass to harden and secure the antennas to the skins. The antennas may slide during this process, so a better mechanism for placement may be possible. One suggestion is to have matching pegs and holes in the antennas and skin to latch into place. This was a suggestion from John Hunter.

Bibliography

[1] "Center for Remote Sensing of Ice Sheets (CReSIS)," 2011. [Online]. Available: https://cms.cresis.ku.edu/

[2] A. Adams and D. Waren, "Dipole Plus Parasitic," *IEEE Transactions on Antennas and Propagation*, pp. 536–537, July 1971.

[3] "High Strength Glass Fibers," AGY, 2558 Wagener Road, Aiken, South Carolina, USA 29801, 2006.

[4] J. Allen and B. Diamond, "Mutual Coupling in Array Antennas," *Technical Report EDS-66-443, Lincoln Lab., MIT*, Oct. 1966.

[5] "Technical Document," Amphenol RF, 2011. [Online]. Available: www.amphenolrf.com/simple/cable_specs.pdf

[6] "Product Specifications FSJ1-50A," Andrew, Westchester, IL, 60154, 2007.

[7] "IEEE Standard Definitions of Terms for Antennas," Antenna Standards Committee of the IEEE Antennas and Propagation Society, 345 East 47th St, New York, NY 10017-2394, 1993.

[8] C. A. Balanis, *Antenna Theory: Analysis and Design.* Hoboken, NJ: Wiley-Interscience, 2005.

[9] V. Bilik and J. Bezek, "Improved Cable Correction Method in Antenna Installation Measurements," *Electronics Letters*, vol. 34, no. 17, pp. 1627–1628, August 1998.

[10] M. Biswas and A. Mandal, "The Effect of Radome on Resonance Characteristics of Triangular Patch Antenna," *International Journal of Engineering Science and Technology (IJEST)*, vol. 3, no. 1, pp. 536–543, January 2011.

[11] J. Brown, "New Understandings of the Use of Ferrites in the Prevention and Suppression of RF Interference to Audio Systems," *Audio Engingeering Society Convention 119th*, October 2005.

[12] R. Chatterjee, *Dielectric and Dielectric-Loaded Antennas.* Great Britain: Research Studies Press and John Wiley and Sons, 1985.

[13] C. Chen and D. K. Cheng, "Optimum Element Lengths for Yagi-Uda Arrays," *IEEE Transactions on Antennas and Propagation*, vol. 23, no. 1, pp. 8–15, January 1975.

[14] D. K. Cheng and C. Chen, "Optimum Element Spacings for Yagi-Uda Arrays," *IEEE Transactions on Antennas and Propagation*, vol. 21, no. 5, pp. 615–623, September 1973.

[15] K. R. Demarest, *Engineering Electromagnetics*. Upper Saddle River, NJ: Prentice Hall, 1998.

[16] J. DeMarinis, "The antenna cable as a source of error in EMI measurements," *IEEE Internationl Electromagnetic Compatiblity Symp. Dig.*, pp. 9–14, August 1988.

[17] S. Edelberg and A. A. Oliner, "Mutual Coupling Effects in Large Antenna Arrays: Part 1 – Slot Arrays," *IEE Proceedings*, vol. 136, no. 4, pp. 311–320, Aug. 1989.

[18] R. S. Elliot, *Antenna Theory and Design*. Englewood Cliffs, NJ: Prentice Hall, 1981.

[19] "Rohacell Dielectric Properties," Evonik Industries, 64293 Darmstadt, Germany.

[20] L. Francavilla, J. McLean, H. Foltz, and G. E. Crook, "Mode-Matching Analysis of Top-Hat Monopole Antennas Loaded with Radially Layered Dielectric," *IEEE Transactions on Antennas and Propagation*, vol. 47, no. 1, pp. 179–185, Jan. 1999.

[21] A. Gangi, S. Sensiper, and G. Dunn, "The Characteristics of Electrically Short, Umbrella Top-Loaded Antennas," *IEEE Transactions on Antennas and Propagation*, vol. 13, no. 6, pp. 864–871, Nov. 1965.

[22] S. Gogineni, D. Braaten, C. Allen, T. Akins, P. Kanagaratnam, K. Jezek, G. Prescott, G. Jayaraman, V. Ramasami, C. Lewis, and D. Dunson, "Polar Radar for Ice Sheet Measurements," *Remote Sensing of Environment*, vol. 111, no. 2-3, pp. 204–211, Nov. 2007.

[23] I. Gupta and A. Ksienski, "Effect of Mutual Coupling on the Performance of Adaptive Arrays," *IEEE Transactions on Antennas and Propagation*, vol. 31, no. 5, pp. 785–791, Sept. 1983.

[24] F. Gustrau and D. Manteuffel, *EM Modeling of Antennas and RF Components for Wireless Communication Systems*. Germany: Springer, 2006.

[25] R. Hale, E. Arnold, and M. Ewing, "Method for Design and Analysis of Externally Mounted Antenna Fairings in Support of Cryospheric Surveying," *American Institute of Aeronautics and Astronautics (AIAA) Structures, Structural Dynamics and Materials Conference*, April 2011.

[26] T. Hertel, "Cable-current effects of miniature UWB antennas," *IEEE Antennas and Propagation Society International Symposium*, Dec. 2005.

[27] M. Hossain, M. Sarkar, and M. Islam, "Performance Comparison of Bow-Tie and Slot Antenna Based on RWG Edge Elements," *IEEE Computer Research and Development, 2010 Second International Conference*, pp. 839–843, May 2010.

[28] C. Icheln, J. Ollikainen, and P. Vainikainen, "Reducing the influence of feed cables on small antenna measurements," *Electronics Letters*, vol. 35, no. 15, pp. 1212–1214, Aug. 1999.

[29] J. James, A. Schuler, and R. Binham, "Reduction of Antenna Dimensions by Dielectric Loading," *Electronic Letters*, vol. 10, no. 13, June 1974.

[30] V. Jara-Olivares and F. Rodriguez-Morales, "Testing Results for Antenna Array," Center for Remote Sensing of Ice Sheets, University of Kansas, 2007.

[31] L. Jian-Ying and G. Yeow-Beng, "Study on Open Sleeve Dipole Antenna," *IEEE international Workshop on Antenna Technology: Small Antennas and Novel Metamaterials*, pp. 291–294, March 2005.

[32] R. Joshi and A. Harish, "A Modified Bow-Tie Antenna for Dual Band Applications," *IEEE Antennas and Wireless Propagation Letters*, vol. 6, pp. 468–471, Oct. 2007.

[33] W. K. Kahn, "Currents on Generalized Yagi Structures," *IEEE Transactions on Antennas and Propagation*, vol. 27, no. 6, pp. 788–797, November 1979.

[34] H. King and J. Wong, "An Experimental Study of a Balun-Fed Open-Sleeve Dipole in Front of a Metallic Reflector," *IEEE Transactions on Antennas and Propagation*, vol. 20, no. 2, pp. 201–204, March 1972.

[35] R. King, "Asymmetrically Driven Antennas and the Sleeve Dipole," *Proceedings of the I.R.E.*, vol. 38, no. 10, pp. 1154–1164, October 1950.

[36] R. King, *The Theory of Linear Antennas with Charts and Tables for Practical Applications*. Cambridge, MA: Harvard University Press, 1956.

[37] R. King, H. Mimno, and A. Wing, *Transmission Lines Antennas and Wave Guides*. The Maple Press Company, York, PA: McGraw-Hill, Inc., 1945.

[38] J. E. Kingman, "Time-Gate Filtering in Geophysical Response Estimation," Terrigena, Ltd., 2005.

[39] S. Kingsley and S. Quegan, *Understanding Radar Systems*. Raleigh, NC: Scitech Publishing, Inc., 1999.

[40] D. Lamensdorf, "An Experimental Investigation of Dielectric-Coated Antennas," *IEEE Transactions on Antennas and Propagation*, vol. 15, no. 6, pp. 767–771, Nov. 1967.

[41] B. Lampe and K. Holliger, "Resistively loaded antennas for ground-penetrating radar: A modeling approach," *Society of Exploration Geophysicists*, vol. 70, no. 3, June 2005.

[42] C. Leat, N. Shuley, and G. Stickley, "Triangular-patch model of bowtie antennas: validation against Brown and Woodward," *IEE Proc.-Microw. Antennas and Propagation*, vol. 145, no. 6, Dec. 1998.

[43] K. F. Lee, *Principles of Antenna Theory.* Printed by Page Bros Ltd, Norwich: John Wiley & Sons, 1984.

[44] P. Lefferson, "Twisted Magnet Wire Transmission Line," *IEEE Transactions on Parts, Hybrids, and Packaging*, vol. PHP-7, no. 4, Dec. 1971.

[45] R. Mailloux, "Antenna and Wave Theories of Infinite Yagi-Uda Arrays," *IEEE Transactions on Antennas and Propagation*, vol. 13, no. 4, pp. 499–506, July 1965.

[46] R. Mailloux, "The Long Yagi-Uda Array," *IEEE Transactions on Antennas and Propagation*, vol. 14, no. 2, pp. 128–137, January 1966.

[47] T. A. Milligan, *Modern Antenna Design.* Hoboken, NJ: Wiley-Intersciene, 2005.

[48] M. Morgan and F. Schwering, "Eigenmode Analysis of Dielectric Loaded Top-Hat Monopole Antennas," *IEEE Transactions on Antennas and Propagation*, vol. 42, no. 1, pp. 54–61, January 1994.

[49] "Broadband Transformers and Power Combining Techniques for RF," Motorola Semiconductor Prodcuts Inc., Box 20913, Phoenix, Arizona, 85036, 1993.

[50] "IceBridge: An Airborne Mission for Earth's Polar Ice," NASA, 2011. [Online]. Available: http://www.nasa.gov/mission_pages/icebridge/science/index.html

[51] J. Paden, T. Akins, D. Dunson, C. Allen, and P. Gogineni, "Ice-sheet bed 3-D tomography," *Journal of Glaciology*, vol. 56, no. 195, pp. 3–11, 2010.

[52] J. Paden, C. Allen, and P. Gogineni, "3D imaging of ice sheets," *IEEE Intl. Geoscience and Remote Sensing Symp. (IGARSS)*, pp. 2611–2613, 2010.

[53] J. Paden, C. Allen, S. Gogineni, K. Jezek, D. Dahl-Jensen, and L. Larsen, "Wideband Measurements of Ice Sheet Attenuation and Basal Scattering," *IEEE Transactions on Geoscience and Remote Sensing Letters*, vol. 2, no. 2, April 2005.

[54] C. R. Paul, *Introduction to Electromagnetic Compatibility, 2nd Ed.* Hoboken, NJ: Wiley-Intersciene, 2006.

[55] "Handbook of Electronic Tables and Formulas," PowerStream, 2011. [Online]. Available: http://www.powerstream.com/Wire_Size.htm

[56] J. Proakis and D. Manolakis, *Digital Signal Processing, 4th Ed.* Upper Saddle River, NJ: Pearson Prentice Hall, 2007.

[57] S. Qu and C. Ruan, "Effect of Round Corners on Bowtie Antennas," *Progress in Electromagnetics Research*, vol. 57, pp. 179–195, 2006.

[58] S. Ramo, J. R. Whinnery, and T. V. Duzer, *Fields and Waves in Communication Electronics, 3rd Ed.* Canada: John Wiley and Sons, Inc., 1994.

[59] J. H. Richmond and E. H. Newman, "Dielectric coated wire antennas," *Radio Science*, vol. 11, no. 1, pp. 13–20, January 1976.

[60] A. Riddle, "Ferrite and Wire Baluns with Under 1 dB Loss to 2.5 GHz," *IEEE Intl. Microwave Symp. Digest*, June 1998.

[61] F. Rodriguez-Morales, P. Gogineni, C. Allen, C. Leuschen, K. Marathe, V. Jara-Olivares, A. Hoch, J. Li, J. Ledford, and K. Jezek, "Dual-Frequency and Multi-Receiver Radars for Sounding and Imaging Polar Ice Sheets," *EUSAR 2008 - 7th European Conference on Synthetic Aperture Radar*, 2008.

[62] F. Rodriguez-Morales, P. Gogineni, C. Leuschen, C. Allen, C. Lewis, A. Patel, K. Byers, L. Smith, L. Shi, B. Panzer, W. Blake, R. Crowe, and C. Gifford, "Development of a Multi-Frequency Airborne Radar Instrumentation Package for Ice Sheet Mapping and Imaging," *IEEE Microwave Symp. Dig.*, pp. 157–160, May 2010.

[63] S. Saario, D. Thiel, J. Lu, and S. O'Keefe, "An assessment of cable radiation effects on mobile communications antenna measurements," *Antennas and Propagation Society International Symposium, 1997. IEEE., 1997 Digest*, July 1997.

[64] R. O. Schmidt, "Multiple emitter location and signal parameter estimation," *IEEE Transactions on Antennas and Propagation*, vol. 34, no. 3, pp. 276–280, March 1986.

[65] J. Sevick, *Transmission Line Transformers, 4th Ed.* Raleigh, NC: Scitech Publishing, Inc., 2001.

[66] J. Sevick, *Understanding, Building, and Using Baluns and Ununs: Theory and Practical Designs for the Experimenter.* Hicksville, NY: CQ Communications, 2003.

[67] T. Simpson, "The Theory of Top-Loaded Antennas: Integral Equations for the Currents," *IEEE Transactions on Antennas and Propagation*, vol. 19, no. 2, pp. 186–190, March 1971.

[68] T. Simpson, "The Disk Loaded Monopole Antenna," *IEEE Transactions on Antennas and Propagation*, vol. 52, no. 2, pp. 542–550, Feb. 2004.

[69] M. Skolnik, *Introduction to Radar Systems, 3rd Ed.* New York, NY: McGraw-Hill, Inc., 2001.

[70] A. Soares, S. Fonseca, and A. Giarola, "The Effect of a Dielectric Cover on the Current Distribution and Input Impedance of Printed Dipoles," *IEEE Transactions on Antennas and Propagation*, vol. 32, no. 11, pp. 1149–1153, November 1984.

[71] T. Spence and D. Werner, "A Novel Miniature Broadband/Mutliband Antenna Based on an End-Loaded Planar Open-Sleeve," *IEEE Transactions on Antennas and Propagation*, vol. 54, no. 12, pp. 3614–3620, December 2006.

[72] W. L. Stutzman and G. A. Thiele, *Antenna Theory and Design, 2nd Ed.* Canada: John Wiley and Sons, Inc., 1998.

[73] G. A. Thiele, "Analysis of Yagi-Uda Type Antennas," *IEEE Transactions on Antennas and Propagation*, vol. 17, no. 1, pp. 24–31, January 1969.

[74] S. Uda, "Wireless Beam of Short Electric Waves," *J. IEEE (Japan)*, pp. 273–282, March 1926.

[75] "Personal Communication with Emily Arnold, Aerospace Engineer," The University of Kansas, 2011.

[76] W. Weeks, *Antenna Engineering.* United States of America: McGraw-Hill, Inc., 1968.

[77] Y. Xiang, "The electrostatic capacitance of an inclined plate capacitor," *Journal of Electrostatics*, vol. 64, pp. 29–34, 2006.

[78] H. Yagi, "Beam Transmission of Ultra Short Waves," *Institute of Radio Engineers*, vol. 16, no. 6, pp. 715–741, June 1928.

Appendix A

Mutual Impedance - General

A general equation for the mutual impedance between a source and a linear conductor is derived below. This relation is useful for describing the coupling physics between multiple antennas or between antennas and parasitic conductors. After the parasitic element has an induced current from the source, this element may become a source re-radiating this energy back to the original source, depending on the capability of this source to radiate energy. The configuration for the mutual impedance is shown in Figure A.1.

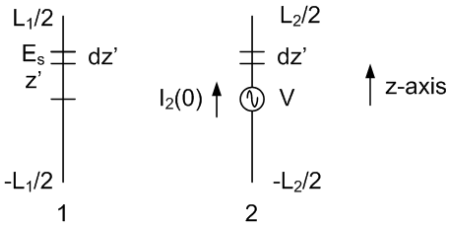

Figure A.1: Source Antenna Coupled to Linear Conductor

The current distribution ($I_2(z')$) on the source, element 2, produces an electric field. This electric field propagates and reaches element 1, which may be either another antenna or a parasitic conductor. At an infinitesimal distance above the conductor the transverse electric field may be called E_i for incident electric field. Due to the boundary

condition on the surface of a conductor, the electric field on the surface of the conductor (E_s) is the inverse and same magnitude as E_i, assuming the sides of are infinitesimal lengths. This relationship comes from energy conservation where the sum of the electric field along a closed loop path must be equal to zero [58]. The boundary condition is given by Equation A.1 [58].

$$\oint \mathbf{E} \cdot \mathbf{dl} = E_s \Delta l - E_i \Delta l = 0 \tag{A.1}$$

The relationship between the electric and magnetic fields can be related using the reciprocity theorem due to Lorentz as given in Equation A.2 [58].

$$\nabla \cdot (\mathbf{E_i} \cdot \mathbf{H_2} - \mathbf{E_2} \times \mathbf{H_1}) = \oint_S (\mathbf{E_i} \cdot \mathbf{H_2} - \mathbf{E_2} \times \mathbf{H_1}) \cdot \mathbf{dS} = 0 \tag{A.2}$$

The H_2 represents the magnetic field around a current element at the source, and H_1 represents the magnetic field around a current element in the receiving conductor. Similarly, E_2 represents the electric field at the port of the source, and since the electric field from one point to another is defined as the voltage, the E_2 may be replaced with a V as shown in Figure A.1. Using this definition for voltage, Equation A.2 can be simplified. The electric fields are defined on the z-axis and can be reduced as follows.

$$\int_{z'}^{z'+dz'} \mathbf{E_s} \oint_S \mathbf{H_2} - V \oint_S \mathbf{H_1} = -\mathbf{E_i} dz' \oint_S \mathbf{H_2} - V \oint_S \mathbf{H_1} = 0 \tag{A.3}$$

Also, the magnetic fields can be written as currents using Ampère's Circuital Law A.4 [58]

$$\oint \mathbf{H} \cdot \mathbf{dl} = \int_S \mathbf{J} \cdot \mathbf{dS} = I \tag{A.4}$$

For a line current, this relationship is expressed an H_ϕ term as shown in Equation A.5 [58]. A line current is used to represent the source for the problem of two antennas. Certainly, different antenna designs have multiple currents that would need to be

considered, which would make the problem more complex at every stage.

$$\oint \mathbf{H} \cdot \mathbf{dl} = 2\pi r H_\phi = I \tag{A.5}$$

Then after applying Ampère's Circuital Law to A.3, the magnetic fields can be written as currents along the z-axis.

$$-\mathbf{E_i} dz' I_2(z') - V I_1(z') = 0 \tag{A.6}$$

Equation A.6 can be re-written in the following form.

$$I_1(z') = \frac{-\mathbf{E_i} dz'}{V} I_2(z') \tag{A.7}$$

The derivation so far has considered only a differential current component at the source, but the total induced current on element 1 is a sum of all the current elements along element 2 and the corresponding incident electric fields at different values along the z-axis. Therefore, the total current along element one is expressed in Equation A.8 [43].

$$I_1 = \frac{-\mathbf{1} V}{\int_{-L_1/2}^{L_1/2}} E_i I_2(z') dz' \tag{A.8}$$

At this point, the induced current has been derived. Since impedance is defined as the voltage over the current, then an expression for the voltage is required. The open-circuit voltage at the source (V_{21}) can be expressed as the product of I_1 and the input impedance at the source (Z_{in2}) [43].

$$V_{21} = I_1 Z_{in2} = \frac{-\mathbf{Z_{in2}} V}{\int_{-L_1/2}^{L_1/2}} E_i I_2(z') dz' \tag{A.9}$$

A simple expression for the Z_{in2} is V divided by the current at z = 0 or $I_2(0)$.

Therefore, Equation A.9 reduces to Equation A.10 [43].

$$V_{21} = \frac{-\mathbf{1}}{I_2(0)} \int_{-L_1/2}^{L_1/2} E_i I_2(z')dz' \tag{A.10}$$

Finally, the mutual impedance can be calculated by using Equation 2.13 for V_{21} divided by the current at the element one at z = 0 ($I_1(0)$) [43].

$$Z_{21} = -\frac{1}{I_1(0)I_2(0)} \int E_{z21} I_2(z')dz' \tag{A.11}$$

Appendix B

Cables

The antenna cables deliver the signal generated from the radar chassis inside the aircraft cabin to the antennas either mounted beneath the cabin or on either wing. A diagram showing the position of the radar rack inside the P-3 cabin and fairing locations is shown in Figure B.1.

The array radiation pattern is dependent on the relative phase between each antenna, as discussed in Section 2.2. As the signals travel through the cables, the phase will also change. Therefore, the cable lengths should be kept the same length in order to ensure the excitation of the array with the proper phased signals. The inboard antennas should each be fed with the same length cable. Also the outboard antennas should each be fed with the same length cables. For the first and second revision, the outboard antennas were used to receive the signals and the phase adjustments can be done post-processing in software. However, the design was implemented to provide the proper lengths for future missions where transmitting on the outboard antennas would be possible.

The cable delays for each section are provided in Table B.1. The first cable listed is the RG-316 DS (DS for Double Shielded) cable that directly feeds the antennas. These were chosen for their flexibility and strain relief at the feed of the antenna. They were securely fastened to the glass and a ferrite (Fair-Rite Part Number: 0443164251) was attached at this location. The delays for the RG-316 cables were calculated based on

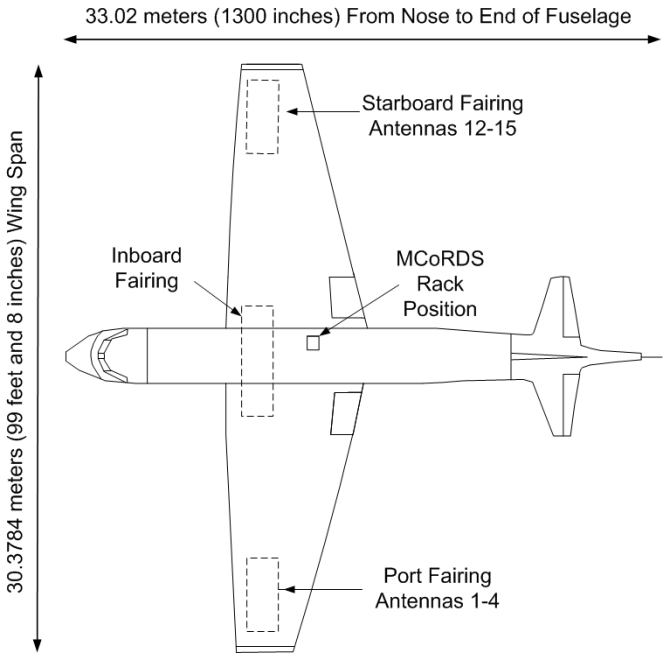

Figure B.1: P-3 Rack Positions Relative to Fairing Locations

their lengths and calculated using the cable delay 4.83 [ns/m] [5]. Each one was 6 inches except for the cable on antenna 8, which was 12 inches. The Heliax (FSJ1-50A) cables inside the fairings were measured using the Vector Network Analyzer (VNA) utility on the RF FieldFox (Agilent N9912A). The S11 was measured from 3 MHz to 3 GHz and 1001 points. Also the cable end not connected to the VNA was terminated in an open circuit. Matlab is used to compute the inverse Fourier transform and obtain the time-domain representation of the S11. There is a peak that represents the returned signal from the end of the cable, and the one way delay is half the time for the return signal. A similar procedure was done for the Heliax installed through the aircraft, except the antennas were already attached to the cables. The measurement then included the RG-316 DS and the fairing Heliax, but these delays are known and were subtracted from the one way delay for the aircraft Heliax. Last, RG-214 DS are used for phase matching cables for the inboard and outboard sections. These cables ensured that the phase delay through each cable is approximately the same for the inboard array and the outboard

arrays. Also the RG-214 DS for the inboard cables, except the center element, had additional lengths added to compensate for the free-space phase delay as discussed in Section 4.5.1. These cables had known lengths, so the delay was calculated using the cable delay for RG-214 DS of 5.05 [ns/m] [5].

Table B.1: Cable Delays for Each Section

Antenna	Delay RG-316 (ns)	Delay Fairing Heliax (ns)	Delay Aircraft Heliax (ns)	Delay RG-214 DS (ns)	Total Delay (ns)
1	0.77	10.83	94.89	0.00	106.49
2	0.77	14.17	88.00	3.56	106.50
3	0.77	17.50	81.39	6.83	106.49
4	0.77	21.00	74.61	10.11	106.48
5	0.77	20.17	41.68	8.05	70.67
6	0.77	16.17	42.81	11.10	70.85
7	0.77	16.00	43.66	10.56	70.99
8	1.54	24.00	44.27	2.02	71.83
9	0.77	20.67	43.64	5.90	70.98
10	0.77	21.50	43.49	5.07	70.83
11	0.77	26.17	43.75	0.00	70.68
12	0.77	9.00	94.94	1.76	106.48
13	0.77	13.17	87.36	5.20	106.49
14	0.77	15.83	82.10	7.80	106.50
15	0.77	19.33	74.63	11.74	106.48

The cable lengths for each section are provided in Table B.3. The RG-316 DS and the RG-214 DS were ordered to length. The calculated delay for the fairing Heliax was used with the Heliax delay of 3.97 [ns/m], calculated from the relative velocity of 0.84 [6]. The same was done for the Heliax installed throughout the aircraft.

The cable attenuation for each section are provided in Table B.3. The lengths for each type of cable is used to calculate the attenuation based on the attenuation per frequency given in Table B.4.

Table B.2: Cable Lengths for Each Section

Antenna	Length RG-316 (m)	Length Fairing Heliax (m)	Length Aircraft Heliax (m)	Length RG-214 DS (m)	Total Length (m)
1	0.15	2.24	23.91	0.00	26.31
2	0.15	2.93	22.18	0.70	25.97
3	0.15	3.62	20.51	1.35	25.64
4	0.15	4.35	18.80	2.00	25.30
5	0.15	4.18	10.50	1.59	16.43
6	0.15	3.35	10.79	2.20	16.49
7	0.15	3.31	11.00	2.09	16.56
8	0.30	4.97	11.16	0.40	16.83
9	0.15	4.28	11.00	1.17	16.60
10	0.15	4.45	10.96	1.00	16.57
11	0.15	5.42	11.02	0.00	16.59
12	0.15	1.86	23.93	0.35	26.29
13	0.15	2.73	22.01	1.03	25.92
14	0.15	3.28	20.69	1.54	25.66
15	0.15	4.00	18.81	2.32	25.29

Table B.3: Cable Attenuation for Each Section at 200 MHz

Antenna	RG-316 (dB)	Fairing Heliax (dB)	Aircraft Heliax (dB)	RG-214 DS (dB)	Total Attenuation (dB)
1	0.01	0.19	2.01	0.00	2.21
2	0.01	0.25	1.86	0.02	2.14
3	0.01	0.30	1.72	0.04	2.08
4	0.01	0.37	1.58	0.05	2.01
5	0.01	0.35	0.88	0.04	1.29
6	0.01	0.28	0.91	0.06	1.26
7	0.01	0.28	0.93	0.06	1.27
8	0.03	0.42	0.94	0.01	1.39
9	0.01	0.36	0.92	0.03	1.33
10	0.01	0.37	0.92	0.03	1.34
11	0.01	0.46	0.93	0.00	1.40
12	0.01	0.16	2.01	0.01	2.19
13	0.01	0.23	1.85	0.03	2.12
14	0.01	0.28	1.74	0.04	2.07
15	0.01	0.34	1.58	0.06	1.99

Table B.4: Cable Types: Attenuation Per Frequency

Attenuation (dB/100m)	100 MHz	200 MHz	300 MHz
RG-316 DS	26.7	37.9	46.6
Heliax	5.89	8.41	10.37
RG-214 DS	1.89	2.71	12

Appendix C

Test Flight Measurements (Time-Domain Gating)

The antennas operate fully installed on the P-3 to measure the ice thickness, internal layers and bed imaging. The antenna performance fully installed includes every structural component included in the aerospace fairing and the realistic ground plane effects. The best validation test for the antenna performance is implemented while installed on the P-3. However, the long cable lengths have an impact on the measurements causing reflections [9]. The cable lengths are discussed in Appendix B. Antenna measurements performed in the frequency domain with digital Vector Network Analyzers (VNAs) permit signal processing to smooth these reflections.

Time-domain gating can be used to filter the reflections in the time-domain and assess the antenna performance without their influences. This method employs the duality of the time and frequency domain to convert a frequency domain measurement into a time-domain signal. An aperiodic signal can be converted from the time domain into the frequency domain using the Fourier transform, and the same is true for converting a frequency domain representation of a signal into a time domain signal. These relations are given in Equations C.1 and C.2 for the inverse Fourier transform

and the Fourier transform, respectively [56].

$$x(t) = \int_{-\infty}^{+\infty} X(F) e^{j2\pi Ft} dF \tag{C.1}$$

$$X(F) = \int_{-\infty}^{+\infty} x(t) e^{-j2\pi Ft} dt \tag{C.2}$$

Once the signal is converting into the time domain, a filter can be applied to remove the unwanted reflections. A common technique to improve the ringing in the frequency domain and decrease the sidelobes [56]. An aperiodic time domain signal is represented as the sum of Fourier series, and limiting the time interval can be interpreted as truncating the series, which introduces ripple called the Gibbs phenomenon [56]. Different window functions are created having a trade-off with main beam width and sidelobe heights. A window is applied using the convolution in the time domain as shown in Equation C.3. The w is the time domain window function, and h is the windowed signal.

$$h(t) = \frac{1}{2\pi} \int_{-\pi}^{+\pi} x_{time}(v) w(t-v) dv \tag{C.3}$$

Three different window functions are shown in Figure C.1. The functions compared are common window functions that can also have the same weights applied to arrays with the same relative side lobe values as those shown in Figure C.1b. The Hanning window is used for the timegating for converting between the frequency domain to the time domain for its deep stop-band and low side lobe values, which is -31 dB below the main lobe [56, 38]. The taper associated with this window function removes about 10 MHz from both the low and high side of measured frequency range. This is notable in the time-gated frequency response. The Tukey window is a boxcar window with half-cosine tapers at the ends that can range from 0 to 1 corresponding to a boxcar or Hanning window for the extremes [38]. The Tukey provides a controllable sharp cutoff

window but lower side lobes than the boxcar window.

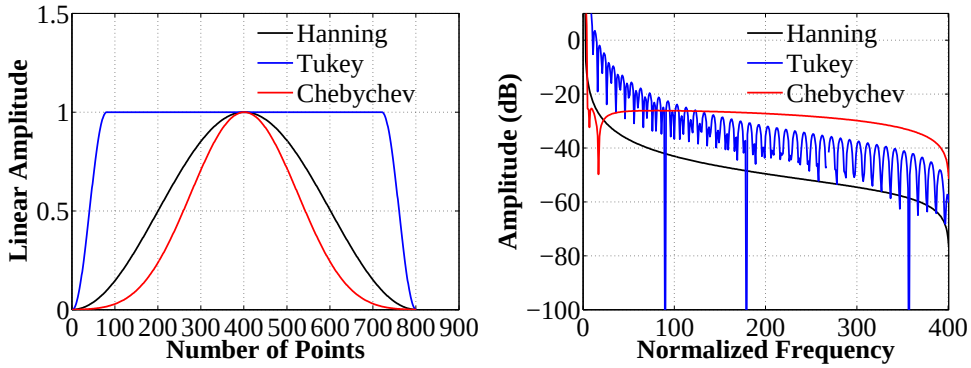

(a) Linear (b) Logarithmic

Figure C.1: Window Shapes

C.1 Test Flight Rev. 1

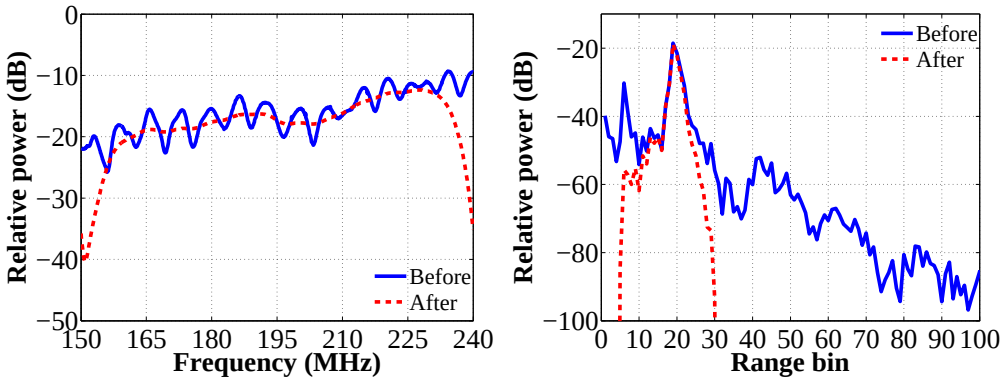

(a) Frequency (b) Time

Figure C.2: Time Gating: Rev. 1 Antenna 1

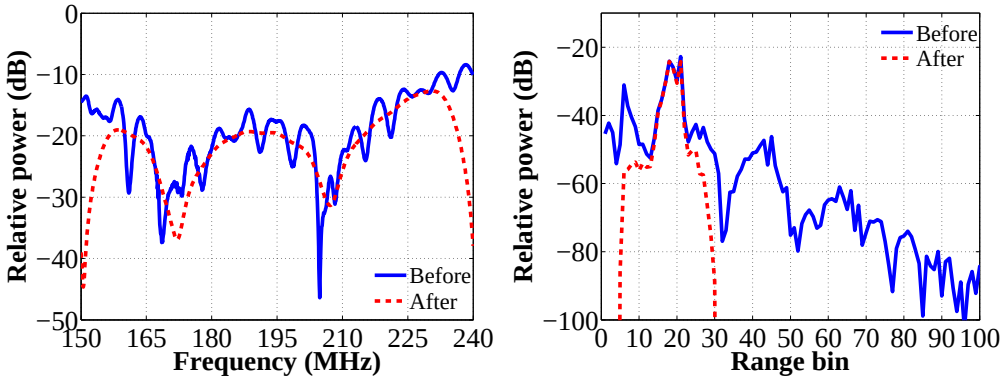

(a) Frequency (b) Time

Figure C.3: Time Gating: Rev. 1 Antenna 2

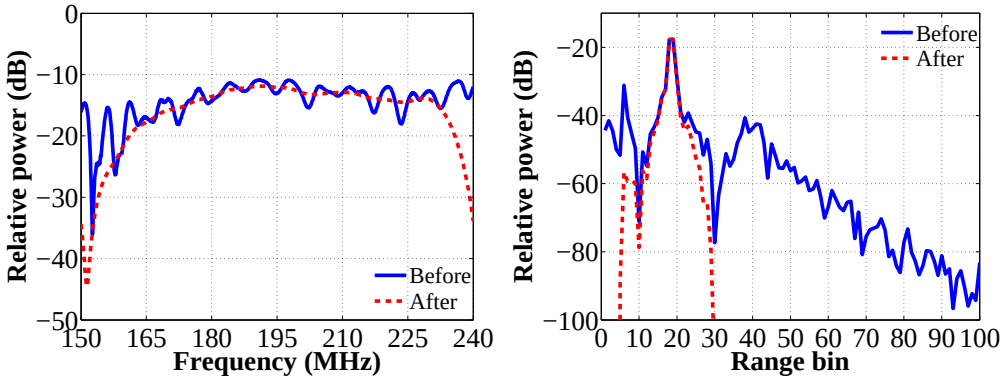

(a) Frequency (b) Time

Figure C.4: Time Gating: Rev. 1 Antenna 3

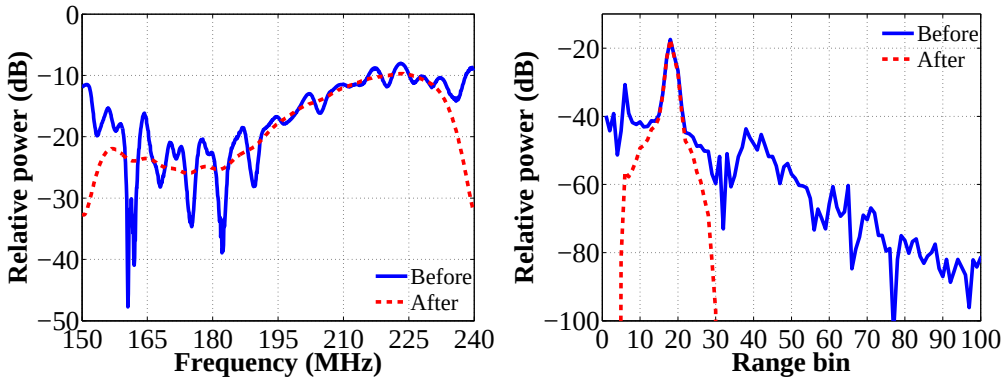

(a) Frequency (b) Time

Figure C.5: Time Gating: Rev. 1 Antenna 4

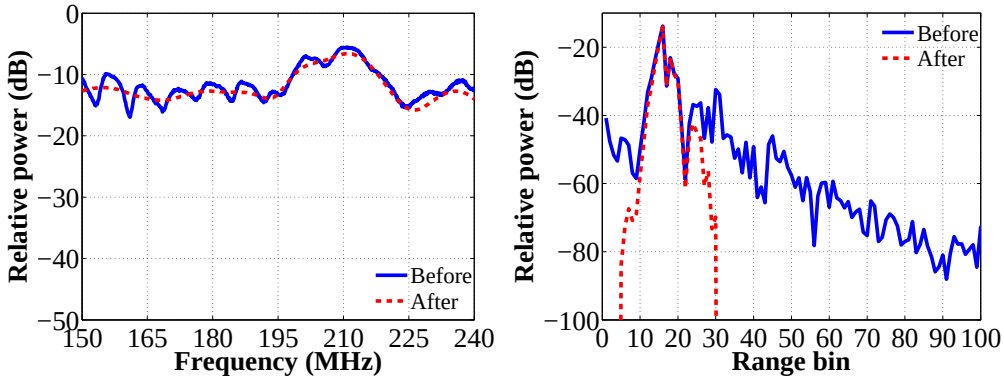

(a) Frequency (b) Time

Figure C.6: Time Gating: Rev. 1 Antenna 5

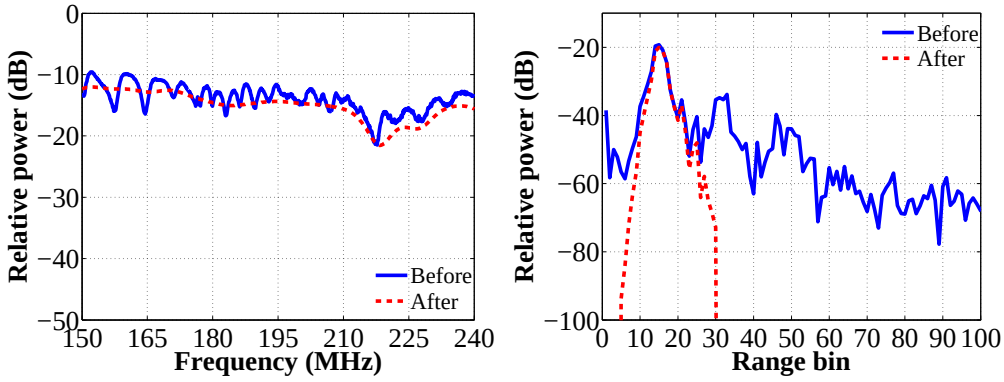

(a) Frequency (b) Time

Figure C.7: Time Gating: Rev. 1 Antenna 6

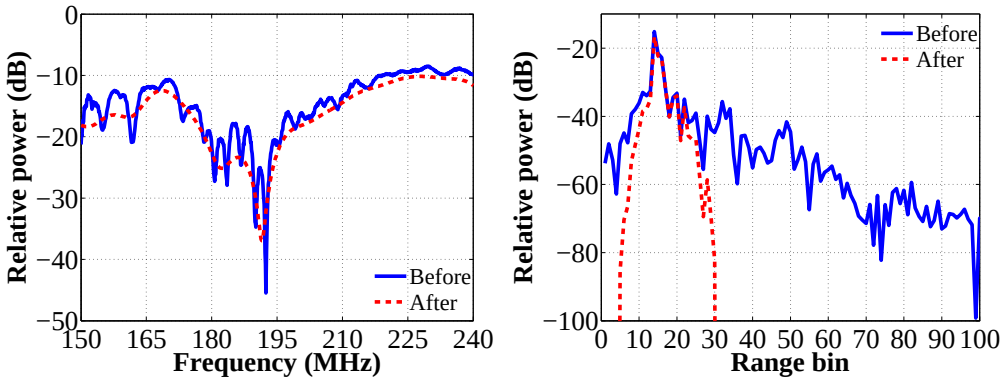

(a) Frequency (b) Time

Figure C.8: Time Gating: Rev. 1 Antenna 7

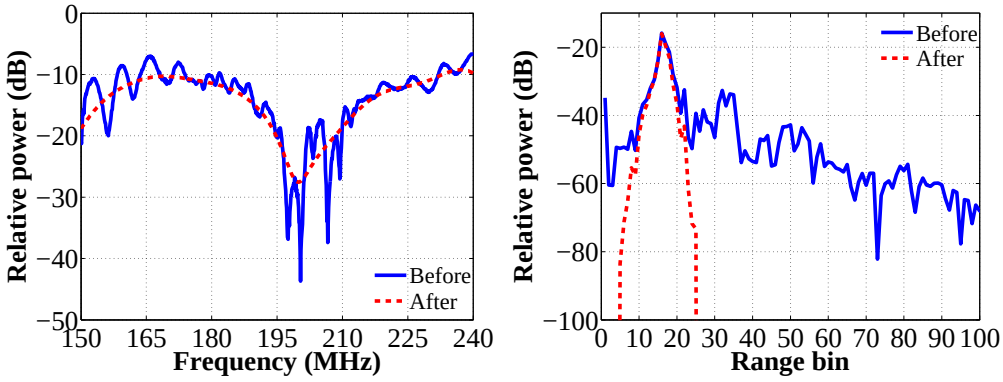

(a) Frequency (b) Time

Figure C.9: Time Gating: Rev. 1 Antenna 8

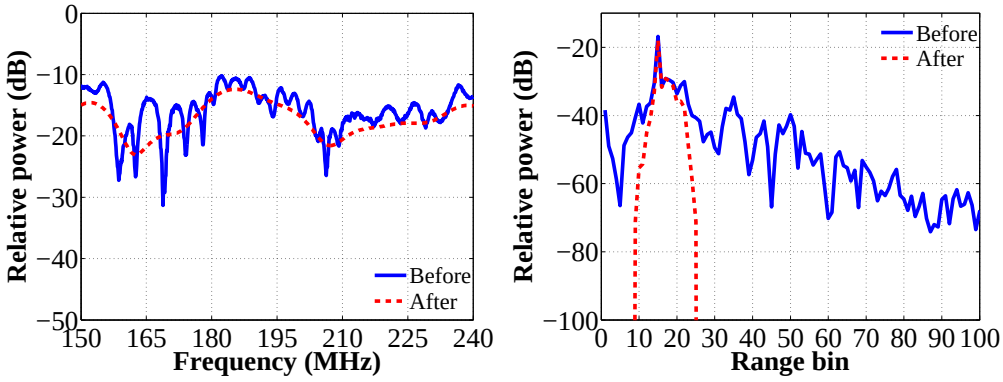

(a) Frequency (b) Time

Figure C.10: Time Gating: Rev. 1 Antenna 9

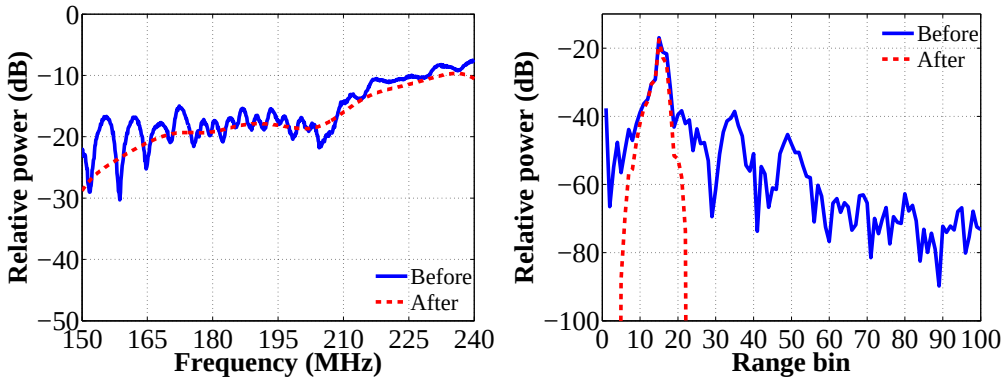

(a) Frequency (b) Time

Figure C.11: Time Gating: Rev. 1 Antenna 10

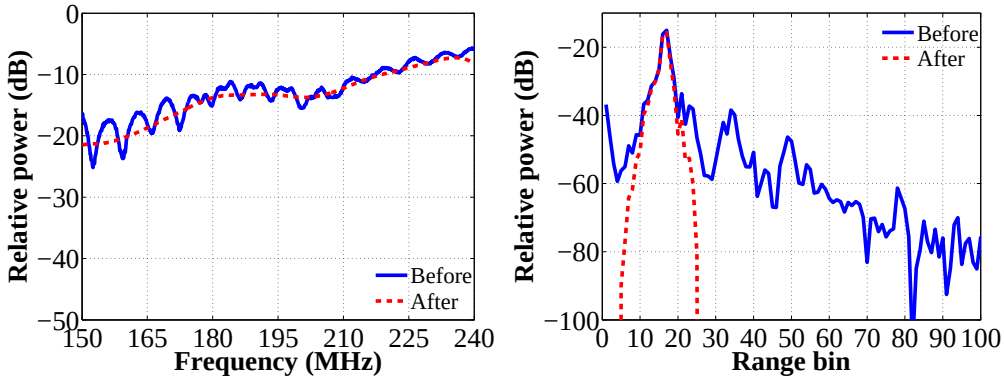

(a) Frequency (b) Time

Figure C.12: Time Gating: Rev. 1 Antenna 11

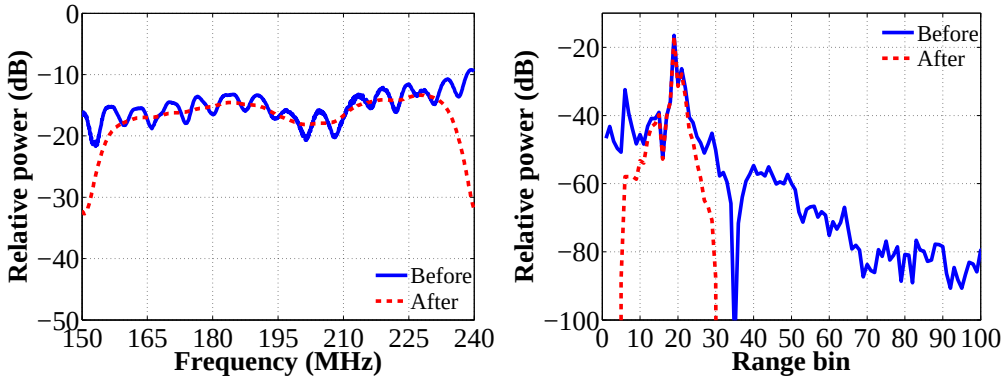

(a) Frequency (b) Time

Figure C.13: Time Gating: Rev. 1 Antenna 12

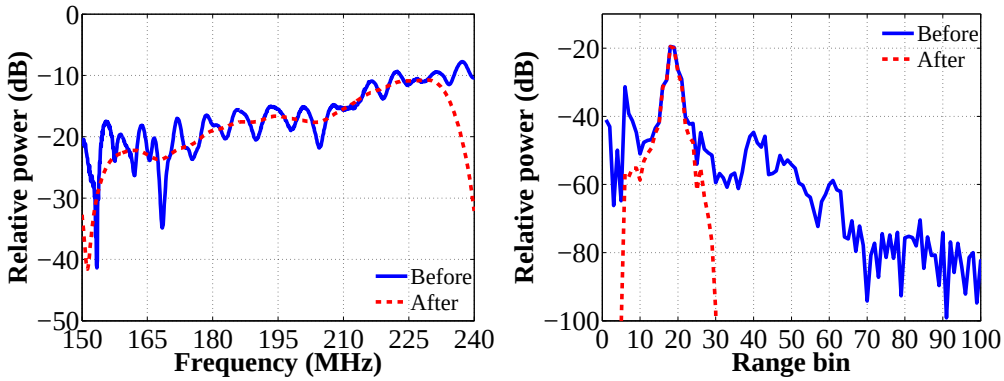

(a) Frequency (b) Time

Figure C.14: Time Gating: Rev. 1 Antenna 13

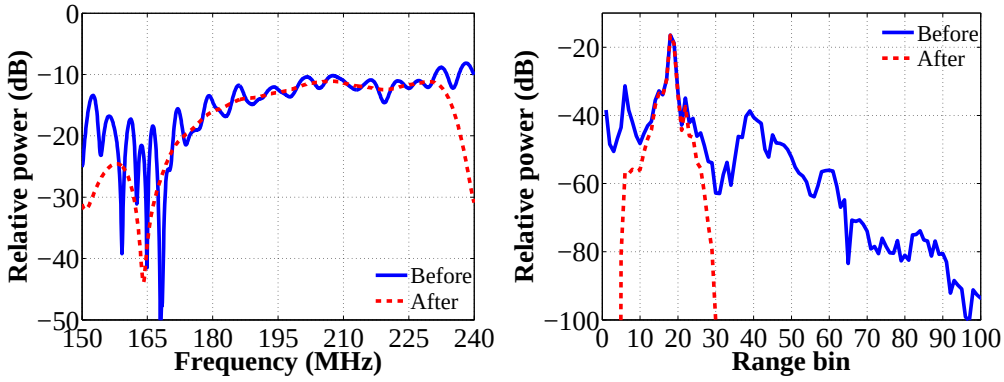

(a) Frequency (b) Time

Figure C.15: Time Gating: Rev. 1 Antenna 14

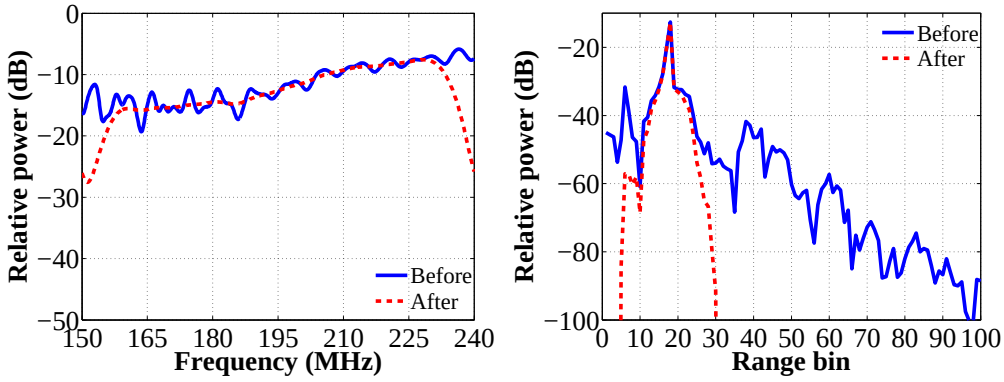

(a) Frequency (b) Time

Figure C.16: Time Gating: Rev. 1 Antenna 15

C.2 Test Flight Rev. 2

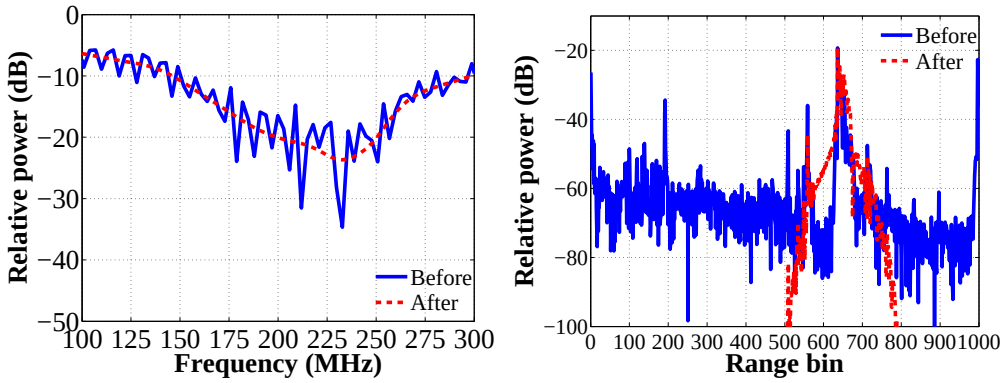

(a) Frequency (b) Time

Figure C.17: Time Gating: Rev. 2 Antenna 1

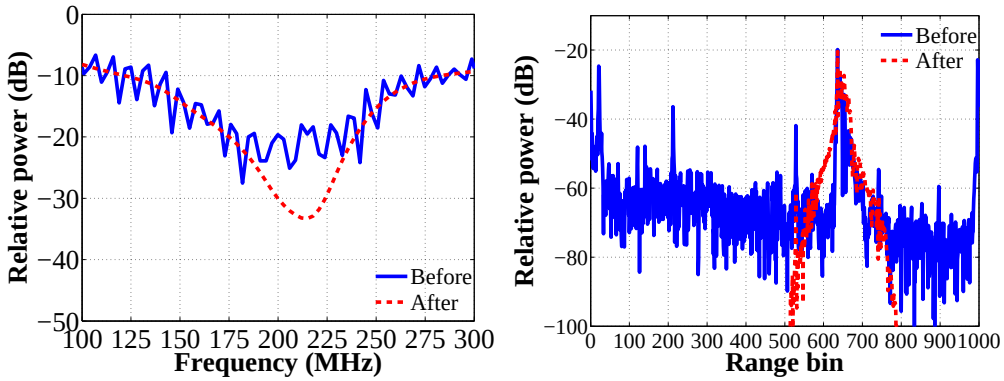

(a) Frequency (b) Time

Figure C.18: Time Gating: Rev. 2 Antenna 2

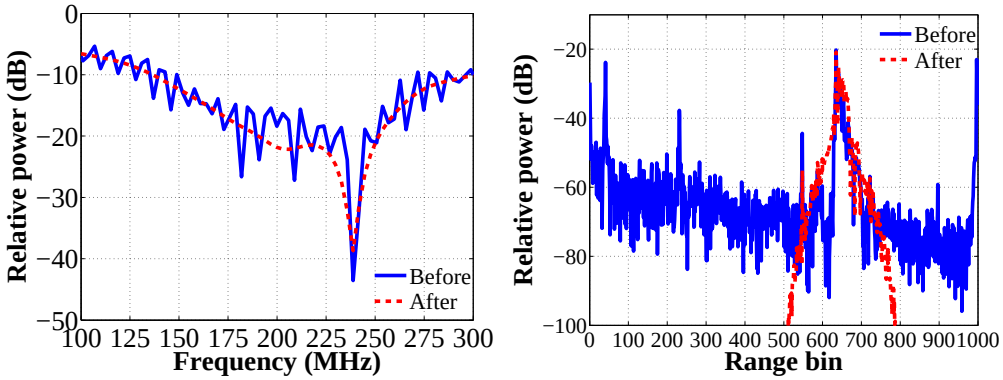

(a) Frequency (b) Time

Figure C.19: Time Gating: Rev. 2 Antenna 3

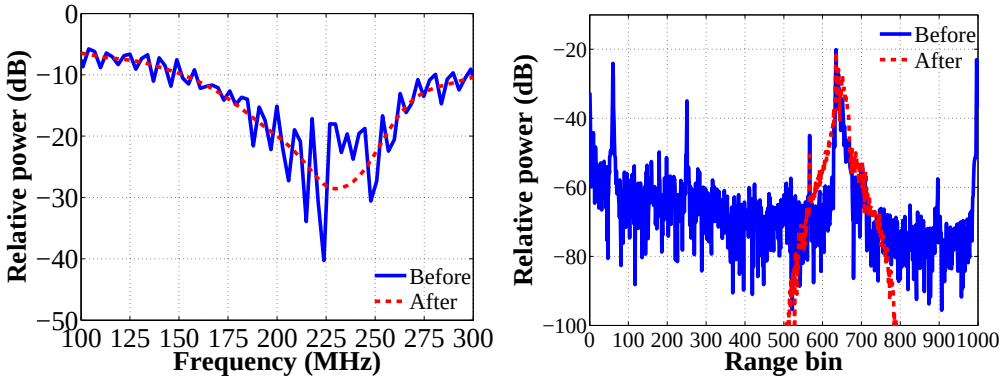

(a) Frequency (b) Time

Figure C.20: Time Gating: Rev. 2 Antenna 4

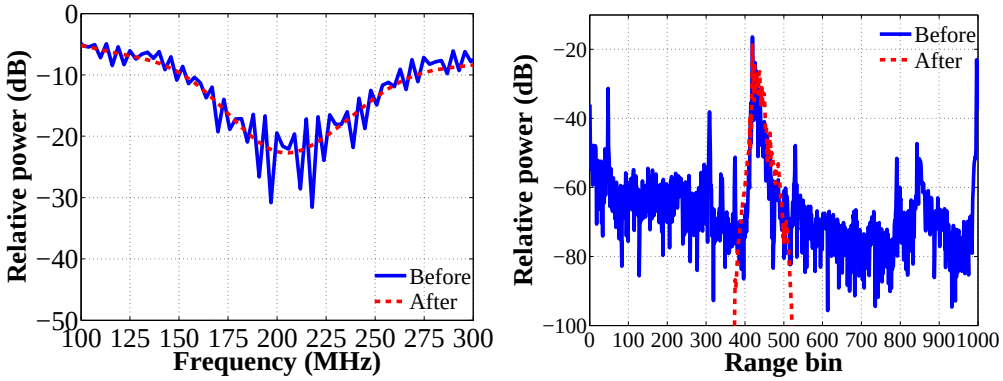

(a) Frequency (b) Time

Figure C.21: Time Gating: Rev. 2 Antenna 5

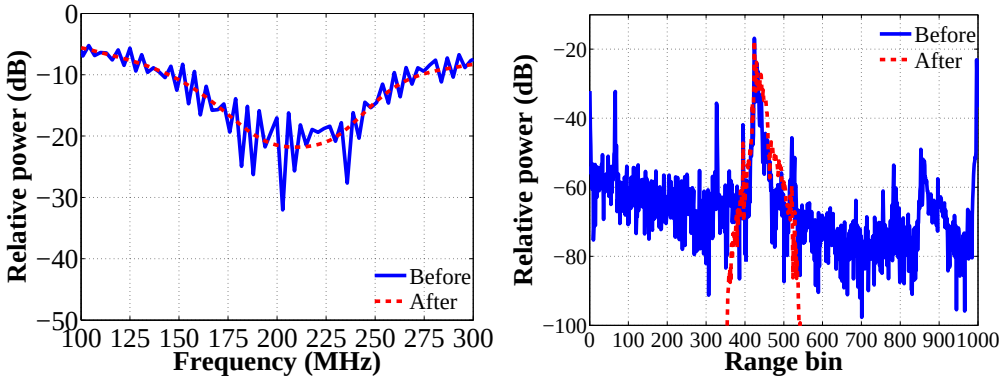

(a) Frequency (b) Time

Figure C.22: Time Gating: Rev. 2 Antenna 6

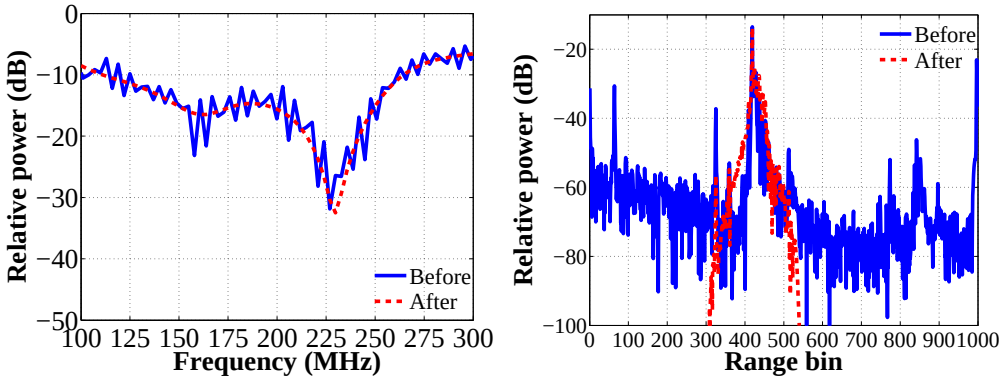

(a) Frequency (b) Time

Figure C.23: Time Gating: Rev. 2 Antenna 7

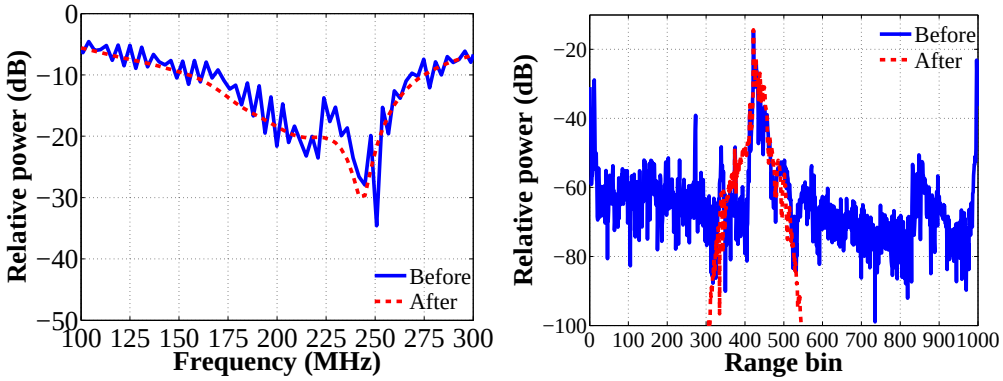

(a) Frequency (b) Time

Figure C.24: Time Gating: Rev. 2 Antenna 8

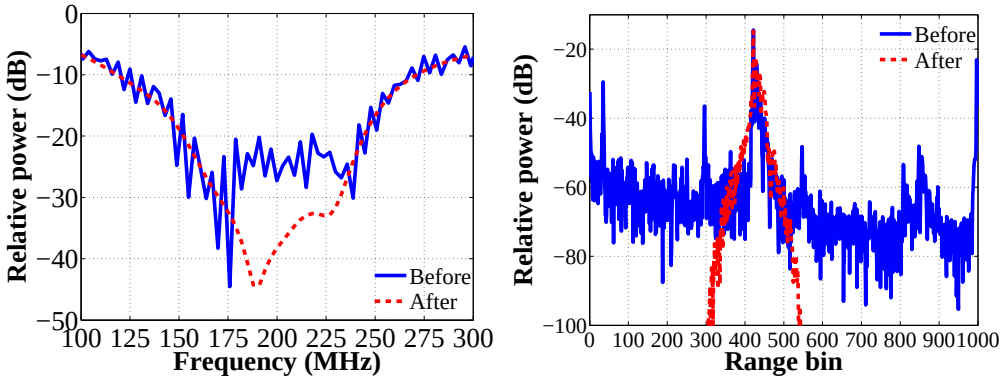

(a) Frequency (b) Time

Figure C.25: Time Gating: Rev. 2 Antenna 9

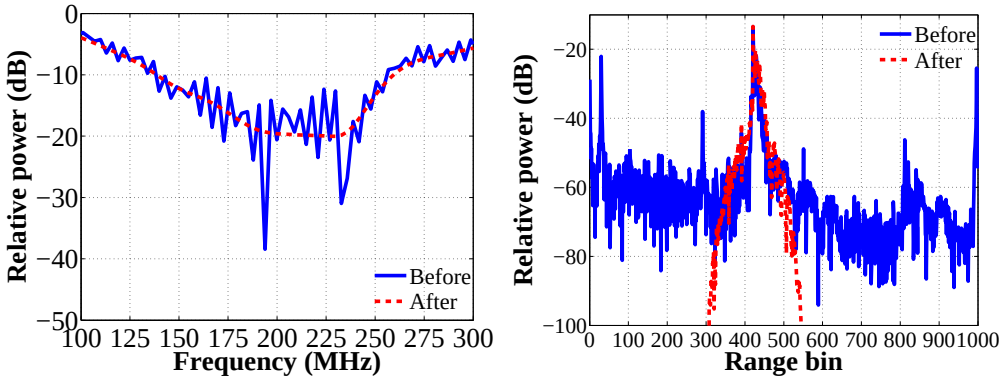

(a) Frequency (b) Time

Figure C.26: Time Gating: Rev. 2 Antenna 10

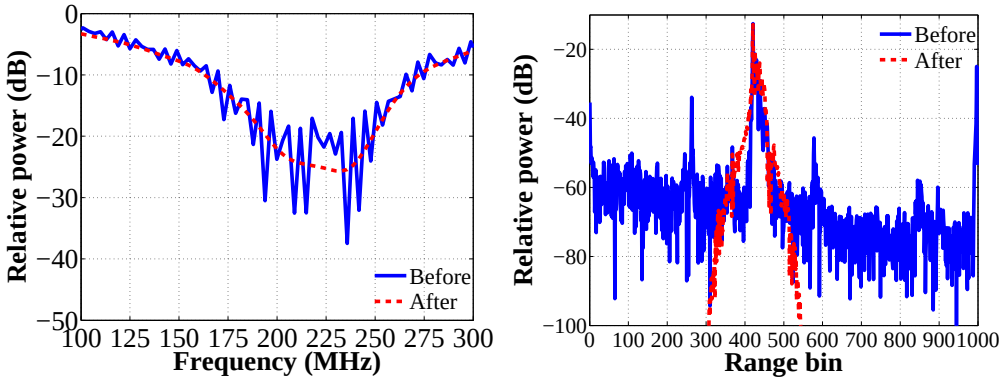

(a) Frequency (b) Time

Figure C.27: Time Gating: Rev. 2 Antenna 11

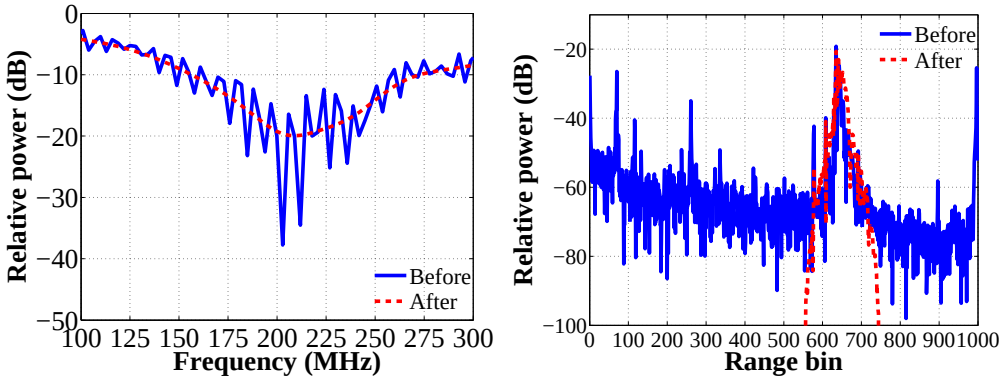

(a) Frequency (b) Time

Figure C.28: Time Gating: Rev. 2 Antenna 12

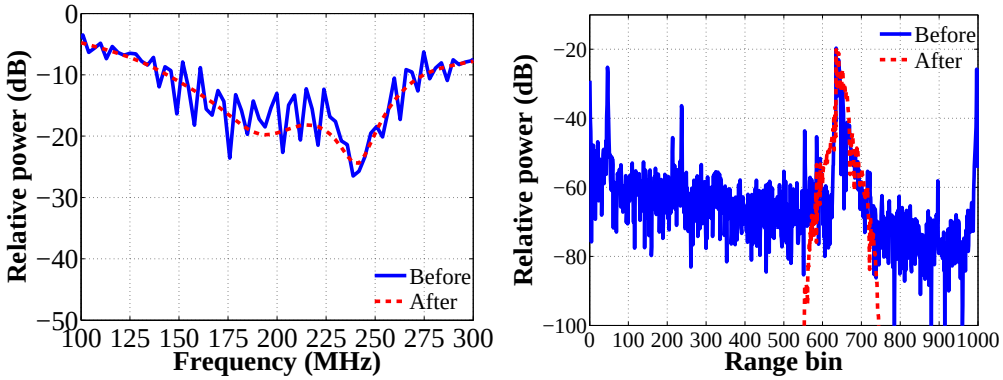

(a) Frequency (b) Time

Figure C.29: Time Gating: Rev. 2 Antenna 13

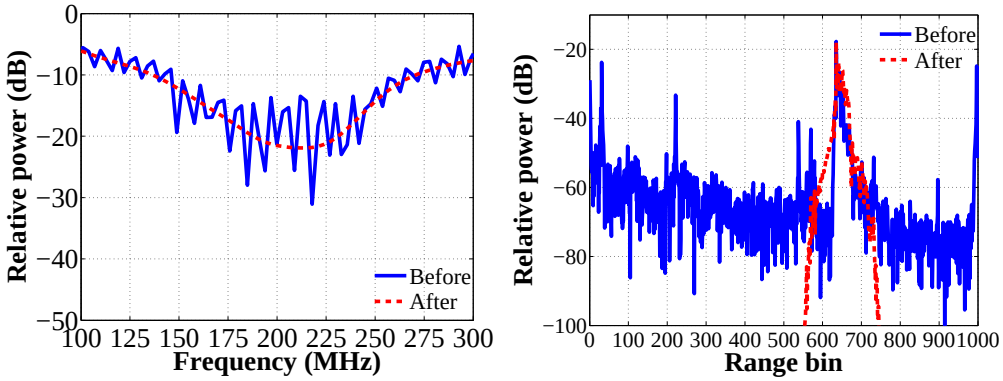

(a) Frequency (b) Time

Figure C.30: Time Gating: Rev. 2 Antenna 14

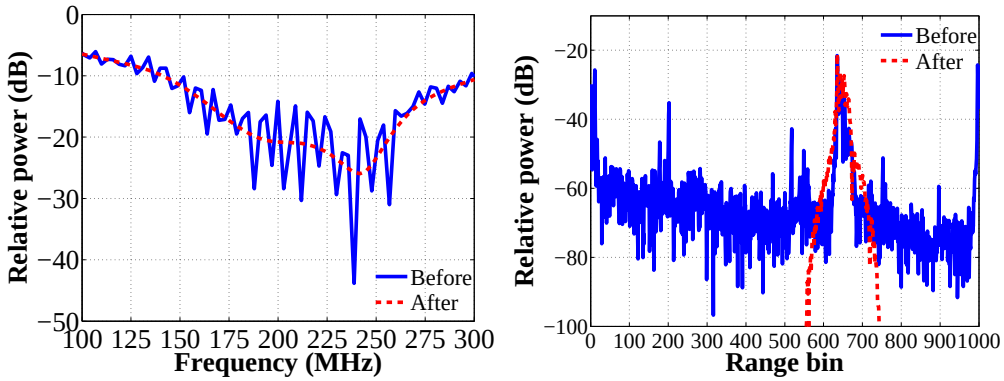

(a) Frequency (b) Time

Figure C.31: Time Gating: Rev. 2 Antenna 15

C.3 Time Gating Code

```
2  %Loads, time gates, and plots return loss data for P-3 antenna array
   taken during the test flight on May 19, 2011.
3  %
4  % Cable loss and balun loss are not considered.
5  % Reminder: time domain windowing in this manner lowers frequency
6  %   domain resolution
7  % Circular convolution due to windowing in time domain is not considered
8  %   so edge effects are apparent in the frequency domain after time gating
9  %
10 % Calibration: 1001 points, 1-port full calibration,
11 %   from 2 MHz-3 GHz
12 % Austin Arnette took measurements during flight over ocean.
13 %     patch cables of varying length were included
14 %   in the measurements and are on every antenna feed cable.  outer
15 %   antenna elements have a bulkhead connector in the wings which
16 %   causes another reflection.
```

```
17 %
18 % Authors: John Paden and Kyle Byers
19 out_dir = '/d0/Byers/P3/TimeGating/out_tf2_v2';
20
21 fmin                = 100;
22 fmax                = 300;
23 l_wid               = 4;
24 leg_pos             = 'SouthWest';
25 leg_pos_1           = 'NorthEast';
26 leg_pos_3           = 'SouthEast';
27 font_name           = 'Times';
28 font_size           = 30;
29 font_size1          = 25;
30 font_size2          = 14;
31 font_size_xlabel    = 12;
32 box_on_off          = 'Off';
33 box_on              = 'On';
34 frm                 = '-depsc2';
35
36 thesis_plots = '/d0/Byers/Thesis/Byers_Kyle_Thesis/plots/';
37
38     a1 = 'ANTENNA1.s1p';
39     a2 = 'ANTENNA2.s1p';
40     a3 = 'ANTENNA3.s1p';
41     a4 = 'ANTENNA4.s1p';
42     a5 = 'ANTENNA5.s1p';
43     a6 = 'ANTENNA6.s1p';
44     a7 = 'ANTENNA7.s1p';
```

```
45      a8 = 'ANTENNA8.s1p';
46      a9 = 'ANTENNA9.s1p';
47      a10 = 'ANTENNA10.s1p';
48      a11 = 'ANTENNA11.s1p';
49      a12 = 'ANTENNA12.s1p';
50      a13 = 'ANTENNA13.s1p';
51      a14 = 'ANTENNA14.s1p';
52      a15 = 'ANTENNA15.s1p';
53      Smap = [1 1 1 1];
54
55   %a1 time_gate = 500:800;
56   %a2 time_gate = 500:800;
57   %a3 time_gate = 500:800;
58   %a4 time_gate = 500:800;
59   %a5 time_gate = 370:525;
60   %a6 time_gate = 350:550;
61   %a7 time_gate = 300:550;
62   %a8 time_gate = 300:550;
63   %a9 time_gate = 300:550;
64   %a10 time_gate = 300:550;
65   %a11 time_gate = 300:550;
66   %a12 time_gate = 550:750;
67   %a13 time_gate = 550:750;
68   %a14 time_gate = 550:750;
69   %a15 time_gate = 550:750;
70
71  time_gate = 500:800;
72  in_fn = a1;
```

```
[in_fn_dir in_fn_name] = fileparts(in_fn);
[freq, all_data, freq_noise, data_noise, Zo] = SXPParse(in_fn);
Sparam = [1 1];   %Hard code for .s1p
data = squeeze(all_data(Sparam(1),Sparam(2),:));
data_td = ifft(data.*tukeywin(length(data),0.01));
data_td_wind = zeros(size(data_td));
data_td_wind(time_gate) = data_td(time_gate)...
                .* hanning(time_gate(end)-time_gate(1)+1);
data_td_wind = fft(data_td_wind);

figure(1); clf;
      plot(freq/1e6, lp(data),'b','LineWidth',l_wid );
      hold on;
      plot(freq/1e6, lp(data_td_wind),'--r','LineWidth',l_wid);
      hold off;
      xlabel('Frequency (MHz)','FontName','Times','FontSize',...
          font_size,'fontweight','b');
      ylabel('Relative power (dB)','FontName','Times',...
          'FontSize',font_size,'fontweight','b');
      set(gca,'XTick',100:25:300,'FontName','Times',...
          'FontSize',font_size);
      grid on;
    l = legend(...
        'Before',...
        'After',...
        'Location','Southeast');
    set(l,'FontName','Times','FontSize',font_size1, 'Box', box_on_off)
    axis([100 300 -50 0]);
```

```
101         out_fn_name = sprintf('rev2_%s_S%d%d_freq', in_fn_name,...
102             Smap(Sparam(2)), Smap(Sparam(1)));
103         out_fn = fullfile(out_dir,out_fn_name);
104 print(1,frm,[thesis_plots, 'Appendices/' out_fn_name],'-r300');
105 % close(1);
106
107 df = freq(2)-freq(1);
108 Nt = length(freq);
109 BW = df*Nt;
110 dt = 1/BW;
111 time = (0:dt:(Nt-1)*dt).';
112
113 figure(2); clf;
114       plot(lp(ifft(data.*tukeywin(length(data),0.2))),...
115             'b','LineWidth',l_wid );
116         hold on;
117       plot(lp(ifft(data_td_wind)),'--r','LineWidth',l_wid);
118         hold off;
119       xlabel('Range bin','FontName','Times','FontSize',...
120             font_size,'fontweight','b');
121       ylabel('Relative power (dB)','FontName','Times','FontSize',...
122           font_size,'fontweight','b');
123       ylim([-100 -10]);
124       xlim([0 1000]);
125       set(gca,'XTick',0:100:1000,'FontName','Times','FontSize',24)
126     l = legend(...
127         'Before',...
128         'After',...
```

```
129           'Location',leg_pos_1);
130       set(l,'FontName','Times','FontSize',font_size1, 'Box', box_on_off)
131         grid on;
132         out_fn_name = sprintf('rev2_%s_S%d%d_time', in_fn_name,...
133             Smap(Sparam(2)), Smap(Sparam(1)));
134         out_fn = fullfile(out_dir,out_fn_name);
135 print(2,frm,[thesis_plots, 'Appendices/' out_fn_name],'-r300');
136 % close(2);
137
138
139 %Create struct for the
140         v = genvarname('RL_Gate');
141         field = genvarname(['Antenna_' in_fn_name]);
142         eval([v '.' field '= lp(data_td_wind);']);
143
144         save([out_dir 'TimeGate_' in_fn_name '.mat'],'-struct', 'RL_Gate');
145
146
147
148
```

Appendix D

Radiation Patterns

The following appendix shows the simulated radiation patterns for different configurations. First, there is a comparison between the free-space rev. 1 antenna and the rev.2 antenna. The addition of the spikes had little impact on the radiation pattern in comparison to a tapered feed dipole without any spikes. Next there are radiation patterns for all the installed configurations for the second revision. These plots show the gain for the E-Plane and H-Plane for both co-polarization and cross-polarization. The co-polarization is shown with solid lines, and the cross-polarization is shown with dashed lines. All the co-polarization plots show consistent results from one antenna to the next. Antenna 2 shows low-cross polarization levels, but antenna 7 has higher cross-polarization levels. Finally, Figure D.4 shows the gain at 90° as a function of the frequency. The gain is fairly constant around 7 dB for antenna 2, but antenna 7 has more variations across frequencies. This is a result of the inconsistent ground plane (i.e. the aircraft skin) next to antenna 7, which has a greater impact on the lower frequencies.

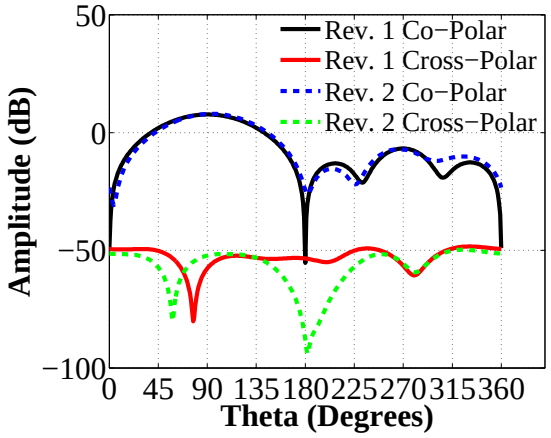

(a) E-Plane

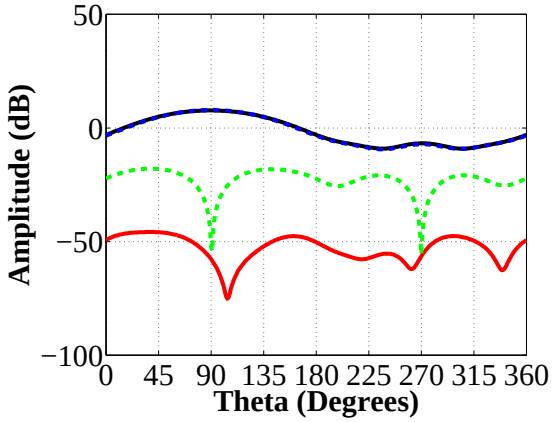

(b) H-Plane

Figure D.1: Radiation Pattern Comparison Between Rev. 1 and Rev. 2

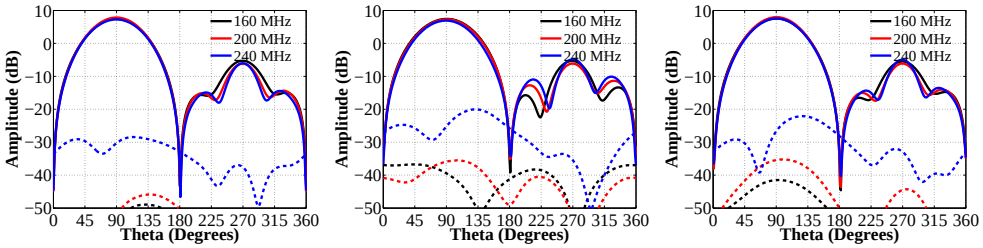

(a) Antenna 1 and 15 (b) Antenna 2 and 14 (c) Antenna 3 and 13

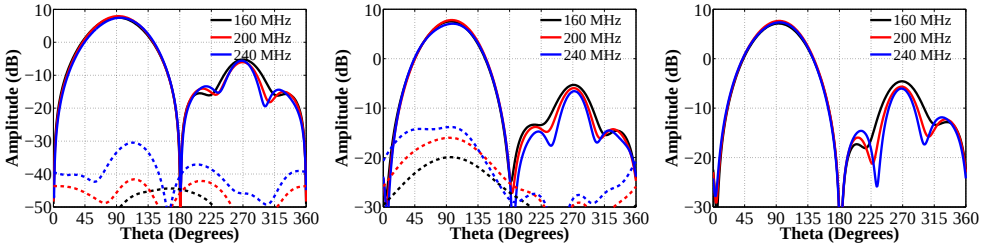

(d) Antenna 4 and 12 (e) Antenna 5 and 11 (f) Antenna 6 and 10

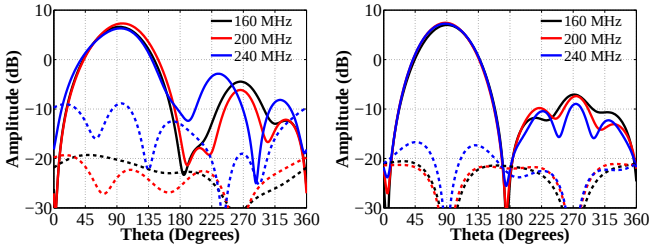

(g) Antenna 7 and 9 (h) Antenna 8

Figure D.2: Installed E-Plane Patterns (Solid Lines: Co-Polar and Dashed Lines: Cross-Polar)

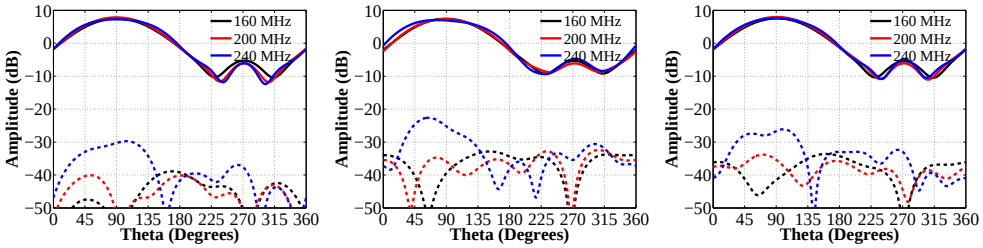

(a) Antenna 1 and 15 (b) Antenna 2 and 14 (c) Antenna 3 and 13

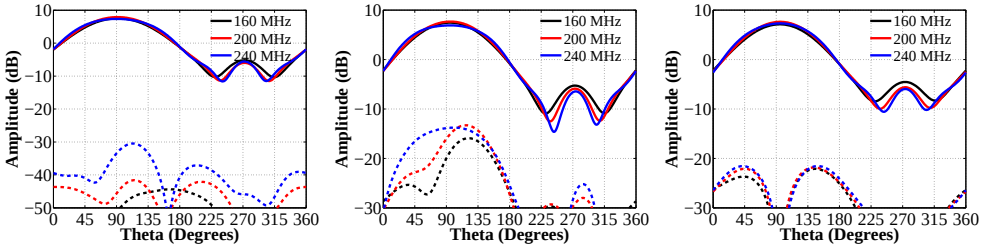

(d) Antenna 4 and 12 (e) Antenna 5 and 11 (f) Antenna 6 and 10

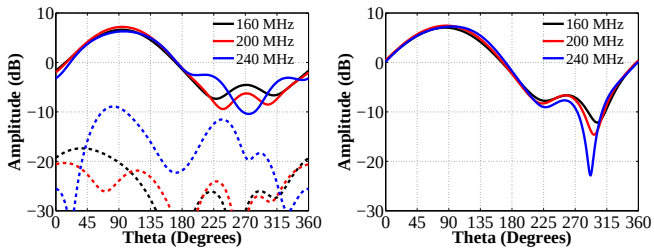

(g) Antenna 7 and 9 (h) Antenna 8

Figure D.3: Installed E-Plane Patterns (Solid Lines: Co-Polar and Dashed Lines: Cross-Polar)

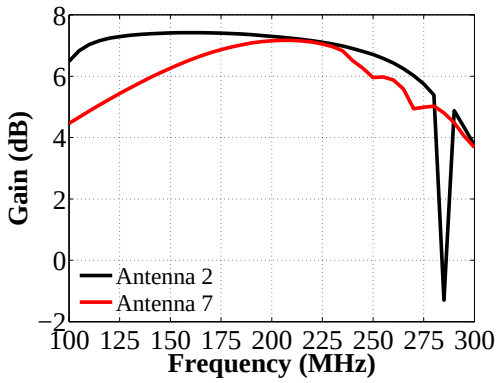

Figure D.4: Gain vs Frequency (Antennas 2/14 and 7/9)